

RICE UNIVERSITY

**A Non-Linear Finite Element Model for the Determination of Elastic
and Thermal Properties of Nanocomposites**

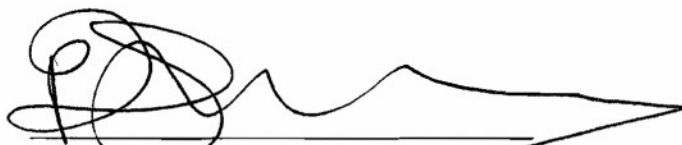
by

Paul Elsbernd, 2nd Lt USAF

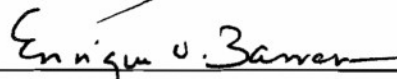
A THESIS SUBMITTED
IN PARTIAL FULFILLMENT OF THE
REQUIREMENTS FOR THE DEGREE

Master of Science

APPROVED, THESIS COMMITTEE:



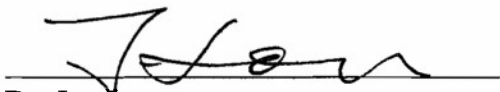
Dr. Pol D. Spanos, Chair
Lewis B. Ryon Professor in Engineering



Dr. Enrique V. Barrera
Professor of Mechanical Engineering &
Materials Science



Dr. John E. Akin
Professor of Mechanical Engineering &
Materials Science



Dr. Jun Lou
Assistant Professor of Mechanical
Engineering & Materials Science

HOUSTON, TEXAS

April 2009

Report Documentation Page				Form Approved OMB No. 0704-0188	
Public reporting burden for the collection of information is estimated to average 1 hour per response, including the time for reviewing instructions, searching existing data sources, gathering and maintaining the data needed, and completing and reviewing the collection of information. Send comments regarding this burden estimate or any other aspect of this collection of information, including suggestions for reducing this burden, to Washington Headquarters Services, Directorate for Information Operations and Reports, 1215 Jefferson Davis Highway, Suite 1204, Arlington VA 22202-4302. Respondents should be aware that notwithstanding any other provision of law, no person shall be subject to a penalty for failing to comply with a collection of information if it does not display a currently valid OMB control number.					
1. REPORT DATE APR 2009		2. REPORT TYPE N/A		3. DATES COVERED -	
4. TITLE AND SUBTITLE A Non-Linear Finite Element Model for the Determination of Elastic and Thermal Properties of Nanocomposites				5a. CONTRACT NUMBER	
				5b. GRANT NUMBER	
				5c. PROGRAM ELEMENT NUMBER	
6. AUTHOR(S)				5d. PROJECT NUMBER	
				5e. TASK NUMBER	
				5f. WORK UNIT NUMBER	
7. PERFORMING ORGANIZATION NAME(S) AND ADDRESS(ES) Rice University				8. PERFORMING ORGANIZATION REPORT NUMBER	
9. SPONSORING/MONITORING AGENCY NAME(S) AND ADDRESS(ES) The Department of the Air Force AFIT/ENEL WPAFB, OH 45433				10. SPONSOR/MONITOR'S ACRONYM(S)	
				11. SPONSOR/MONITOR'S REPORT NUMBER(S) CI09-0048	
12. DISTRIBUTION/AVAILABILITY STATEMENT Approved for public release, distribution unlimited					
13. SUPPLEMENTARY NOTES The original document contains color images.					
14. ABSTRACT					
15. SUBJECT TERMS					
16. SECURITY CLASSIFICATION OF:			17. LIMITATION OF ABSTRACT UU	18. NUMBER OF PAGES 106	19a. NAME OF RESPONSIBLE PERSON
a. REPORT unclassified	b. ABSTRACT unclassified	c. THIS PAGE unclassified			

The views expressed in this article are those of the author and do not reflect the official policy or position of the United States Air Force, Department of Defense, or the U.S. Government.

Abstract

A Non-Linear Finite Element Model for the Determination of Elastic and Thermal Properties of Nanocomposites

by

Paul Elsbernd

This thesis presents a non-linear model for the thermal and elastic properties of single-walled carbon nanotube reinforced polymer composites. Finite Element Analysis (FEA), in conjunction with the Embedded Fiber Method (EFM), is used to calculate the effective stress-strain curve and thermal conductivity of the composite material. First, the geometry of a user-defined volume fraction of nanotubes is randomly generated and their properties are incorporated into the polymer matrix using the EFM. Non-linear FEA is next performed to account for the non-linear properties of the polymer matrix and the carbon nanotubes. Finally, Monte Carlo Analysis of five hundred random microstructures is performed to capture the stochastic nature of the random fiber generation and to derive statistically sound results. The model is validated by comparison with several different experiments reported in the open literature.

Acknowledgements

I would like to sincerely thank several individuals who helped me in many ways throughout my research and thesis writing process. First and foremost, my sincere thanks go to my advisor, Dr. Pol Spanos. He chose to offer me a scholarship to Rice University and has been a constant help and advisor to me in my research. His mentorship and knowledge have been invaluable resources throughout my studies.

I would also like to thank Dr. Milton Esteva for the completely unselfish volunteering of his time, energy, and guidance throughout my entire graduate experience. His help in selecting a thesis topic, his guidance in an area that had previously been so foreign to me, and his technical expertise made this work possible and truly enjoyable. Thank you Milton.

Additional thanks go to Professor John Akin who helped me in the technical areas of Finite Element programming. Thank you for your time and efforts beyond the classroom. Thank you to Dr. Enrique Barrera and Dr. Jun Lou for serving on my thesis committee. Many thanks go to Dr. Jan Hewitt as well for volunteering her time and knowledge in the proofreading and critiquing of my thesis writing.

Finally, I would like to thank my beautiful wife Sarah for continuously supporting me and encouraging me through the several slumps I had in my research and motivation. Her love and encouragement helped me every day and I truly appreciate her unwavering support.

This work was funded by Rice University and the U.S. Air Force through the Clarkson Project for Materials Science research.

Contents

Abstract	iii
Acknowledgements	iv
List of Figures	vi
Introduction	1
1.1 Motivation	1
1.2 Obstacles to Accurate Experimentation	3
1.3 Current CNT Composite Models	6
The Representative Volume Element	11
2.1 Geometry Generation	12
2.2 Fiber Partitioning	19
2.3 The Embedded Fiber Method	22
The Non-Linear Finite Element Model	29
3.1 Non-Linearity of Carbon Nanotubes and Epoxies	30
3.2 Non-Linear FEA Solution Techniques	33
3.3 Details of the Model	40
Numerical Results	48
4.1 Deformation Behavior	48
4.2 Stress-Strain Results	58
4.3 Thermal Results	69
Concluding Remarks	84
References	87
Appendix A	97

List of Figures

Figure 1. A histogram of 1,000 Weibull randomly generated nanotube lengths.....	13
Figure 2. Lognormal distribution fit to the diameter data reported by Ziegler et al. [29].	15
Figure 3. The effective diameter of SWCNT as reinforcement is increased due to the carbon-carbon bonding between the nanotube and the matrix. The actual nanotube diameter is depicted as R_n and the effective diameter including the carbon-carbon spacing is shown	16
Figure 4. A histogram of the lognormal random effective diameters generated using the parameters from Ziegler's paper [29] are presented, including carbon-carbon spacing...	17
Figure 5. (a) A single, full RVE with 0.0889% v.f. nanotubes is depicted. (b) A close-up view of one section of the RVE is shown. The waviness of the nanotubes is easily observed. Longer nanotubes are wavier than shorter nanotubes to simulate the physical phenomenon.....	18
Figure 6. The nanotube geometry of a small section of an RVE before fiber partitioning is presented. The nanotubes are divided into ten segments each, with an "x" marking the end of each segment.....	20
Figure 7. (a) A visualization of the same microstructure as Fig. 5 with "x's" marking the division of individual nanotubes into segments. (b) A magnified view of one region of the RVE. The circles represent segments that were partitioned because they crossed element boundaries.....	21
Figure 8. The finite element mesh of the carbon nanotube/fiber cross-ply composite used by Li and Chou [19]. The intense mesh refinement along the nanotube matrix boundaries is to be noted.....	27
Figure 9. The non-linear thermal properties of SWCNTs are shown in the analysis of Grujicic et al. [15].	31
Figure 10. A block diagram of the non-linear incremental scheme for the elastic case is presented. Notice the two major loops which are the driving force behind the computational time required by the model.	38
Figure 11. Tensile stress versus strain curves for the various composites reported by Sun et al. are presented [45]. The bottom, black line is used in the current model to update the elastic modulus of the epoxy matrix.	42
Figure 12. Tensile stress versus strain curves for the composites reported by Zhu et al. are presented [22]. The middle, neat epoxy line is used in the current model to update the elastic modulus of the epoxy matrix.	43
Figure 13. A close view of the stress-concentrations at nanotube tips due tensile strain is presented. Li and Chou developed this picture from their damage sensing model [19].	45
Figure 14. A diagram of a single SWCNT structure illustrates the hollow, tubular nature of CNTs [55].	46
Figure 15. A diagram of the boundary conditions for the first test condition is presented. The bottom left corner is pinned and the bottom boundary is on rollers.....	49
Figure 16. A visualization of the mesh refinement for one, two, three, and five divisions, respectively is shown.	50

Figure 17. The mesh deformation visualization for a single RVE, with 10 divisions and 1 wt% SWCNTs, stretched to 3.5% strain is presented. The change in shape of the RVE can be easily seen and by examining the shape change of each element, the reinforcing effect of fibers can be observed. The displacements of the final mesh are multiplied by a factor of three to make visualizing easier.	51
Figure 18. A contour plot of the y displacements of the element nodes is presented with the nanotube locations superimposed. The reinforcing properties of the nanotubes can be observed by noting the regions where colors stay the same. Some samples of these regions are highlighted with white boxes.	52
Figure 19. The mesh deformation and contour plot of y displacements for the same RVE are presented at 2.5% strain. By visualizing the displacements of a single incremental step the reinforcing capabilities of the nanotubes are very clear. The displacements of the final mesh on the left are multiplied by 300 to make visualizing easier.....	53
Figure 20. The contour plots of the y displacements after the first and 75th incremental steps are presented. By examining the deformation before and after the onset of plastic deformation, the role of the nanotubes in combating plastic deformation is evident.	54
Figure 21. A diagram of the boundary conditions for the second test condition illustrates the traditional tensile test. The bottom edge is completely fixed and the top edge is fixed in the x-direction.	54
Figure 22. The mesh deformation for the second testing condition is presented. (a) Mesh deformation for an RVE without nanotubes. Symmetric deformation is observed (b) Mesh deformation for an RVE with 1 wt. % SWCNTs is shown. The final mesh displacements are multiplied by a factor of 3 to make visualizing easier.	55
Figure 23. The displacement contours for the second test condition are presented. (a) The displacement contour of RVE without reinforcement is shown. (b) The displacement contour of an RVE with 1 wt % nanotubes is shown for comparison.	56
Figure 24. A displacement contour of the second test condition with special features indicated is presented. The areas boxed in white indicate sample regions of particularly strong reinforcement in the tensile direction as shown by the continuity of color. The white paths across the RVE indicate probable locations of fracture in the RVE due to lack of reinforcement.....	57
Figure 25. (a) The non-linear incremental convergence analysis for the model is shown for a single division of the RVE. (b) A closer view of the model results at high strains. A step refinement of 100 incremental steps is identified as sufficient for convergence.	60
Figure 26. (a) The mesh convergence analysis for the model with one hundred incremental steps is shown for 1, 10, 20, 40, 60, and 80 divisions of the RVE. The “diamond” line identifies the experimental results of Sun et al. [45]. (b) A closer view of the model results at high strains. A mesh refinement of 60 divisions is identified as sufficient for accurate stress-strain results.....	62
Figure 27. (a) The mesh convergence analysis for the model with one incremental step is shown for 1, 10, 20, 40, 60, and 80 divisions of the RVE. The “diamond” line identifies the experimental results of Sun et al. [45]. (b) The same analysis is shown for the model with 10 incremental steps.....	64
Figure 28. (a) The model results for 60 divisions, 100 steps are compared to the results of Sun et al. [45]. (b) A close view of the stress-strain curve high strain values is shown..	66

Figure 29. The maximum and minimum RVE's out of the 500 RVE's sampled in the MCMCA are compared to the experimental results of Sun et al. [45] to highlight the span of possible outcomes for random nanotube geometries.....	67
Figure 30. The model results for 60 divisions, 100 steps are compared to the results of Zhu et al. [22]. The center, blue F-SWCNT line represents the experimental data.....	68
Figure 31. A diagram of the boundary conditions for the thermal analysis is shown. The top edge is held at 100° C and the bottom is held at 0°C while the sides are insulated. ..	71
Figure 32. A contour plot of temperatures from the non-linear thermal model is presented.	73
Figure 33. (a) The MCMCA for the thermal conductivity of 500 RVEs is presented for the incremental approach. A mesh refinement of 130 divisions is needed for accurate results. (b) By zooming in, it is also evident that 10 incremental steps are sufficient to capture the non-linearity of the thermal conductivity of the nanotubes.	75
Figure 34. (a) The MCMCA for the thermal conductivity of 500 RVEs is presented for the iterative approach. A mesh refinement of 130 divisions is needed for accurate results. (b) By zooming in, it is also evident that only two iterative steps are needed to capture the non-linearity of the thermal conductivity of the nanotubes.	77
Figure 35. A comparison of the thermal conductivities calculated by the model to various experiments is shown.	80
Figure 36. A comparison of the modified model's thermal conductivity results to various experiments is presented. Much better agreement with experimental results is clearly evident.....	82

Chapter 1

Introduction

1.1 Motivation

As nanotechnology has blossomed over the last two decades, countless applications for a variety of nanoparticles have been demonstrated or proposed. The use of gold nanoparticles to destroy tumors [1], of carbon nanotubes to improve bullet proof vests [2], and of fullerene nanoparticles to detect biological markers of disease [3] are a few examples that encompass only a tiny fraction of the countless possible applications of nanoparticles. Arguably, the most commonly proposed application of nanoparticles is their use in composite materials. While the choice of particle strongly depends on the functionality sought for the composite, one of the most widely studied nanocomposites is the carbon nanotube reinforced composite.

Carbon nanotubes offer exceptional mechanical, thermal, and electrical properties at an almost insignificant weight on the macroscale. Theoretically, single-walled carbon nanotubes (SWCNTs) exhibit elastic moduli of the order of 1 TPa and fracture strains of 10-30% [4-8]. Initial experiments did not identify such a specific value for the elastic modulus due to undeveloped experimental techniques and carbon nanotubes that were not perfectly prepared or treated. Troiani et al. [9] reported an elastic modulus of 305 ± 156 GPa. On the other extreme, Treacy et al. [10] report 1.8 ± 0.9 TPa. Recent

improvements in nanotube fabrication and new experimental techniques have yielded elastic properties that are more consistent with theoretical predictions. Wong et al. [11] and Yu et al. [8] reported elastic moduli of 1.28 ± 0.59 TPa and 0.95 TPa, respectively. These findings indicate that SWCNT's have elastic moduli that are three times that of carbon fibers, and five times that of steel at one sixth the weight [12].

In addition to their outstanding mechanical properties, carbon nanotubes exhibit exceptional thermal and electrical properties. The theoretical thermal conductivity of SWCNTs is usually reported as $6,000 \frac{W}{m-K}$ at room temperature [13], which is approximately three times the thermal conductivity of diamond, and approximately 10^4 times that of most polymers [14]. This value is in fact highly temperature dependent as reported by Grujicic et al. [15], ranging from values as high as $12,000 \frac{W}{m-K}$ at 100K to about $2,000 \frac{W}{m-K}$ at 300K. Carbon nanotubes are also found to have exceptional electrical conductivity, of the order of $10^4 \sim 10^7 \frac{S}{m}$, approximately 20 decades higher than that of most polymers [14,16].

These outstanding properties make carbon nanotubes extremely interesting for a variety of applications. Individually, applications for CNTs include field emission sources, Lithium-ion batteries, capacitors, actuators, molecular sensors, gas and hydrogen sources, scanning probe tips, and countless electronics applications [17,18]. However, of more interest to this current study are the potential applications for nanotubes in composite materials; polymer composites in particular. Their mechanical properties make them ideal candidates to use as reinforcing agents, either alone or as filler with other reinforcements, such as carbon or glass fibers. Their thermal properties make them

desirable for thermal management applications, and their electrical properties make them ideal for numerous other composite applications such as electromagnetic shielding, preventing electrostatic charging, and damage sensing [19,20]. Collectively, these properties make nanotube composites very interesting to many different fields including the aerospace, automotive, medical, and defense industrial sectors.

Because of the significant promise in these new composites, a need to predict their physical properties has developed. It is in this context that the motivation for the current work is derived. The capacity to accurately predict properties of nanocomposites is particularly needed because the sheer number of different possible composites limits experimental characterization. Not only are there countless different polymers to be used as the matrix material of the composite, but the effect of various volume fractions of nanotubes also needs to be studied for each composite. These two factors are the primary motivations for an accurate and versatile model of carbon nanotube composites behavior.

1.2 Obstacles to Accurate Experimentation

Besides the overwhelming number of possible composites, there are four major issues influencing the experimental accumulation of accurate information about nanotube composites. They are: inadequate interfacial bonding, poor dispersion, waviness and alignment issues, and nanoscale measurement concerns. Interfacial bonding describes the ability of the carbon nanotube to chemically bond to the matrix material. This point relates to the inherent physical structure of carbon nanotubes. Pristine nanotubes are essentially defect-free and atomically smooth. This fact inhibits interfacial bonding with

the matrix structures in which CNTs are mixed and thus tremendously inhibits their reinforcing capabilities.

This problem has been approached by several researchers and the most effective solution has been functionalization. Surface functionalization is the process by which various chemical functional groups are attached to the nanotube sidewalls and/or endcaps using either covalent or non-covalent bonding. This process was first proposed for nanotubes by Tiano et al. [21]. By specifically choosing functional groups based upon the composite matrix material, a dramatic increase in the interfacial bonding in the composite can be achieved. Zhu et al. [22] report that by utilizing acid treatment and fluorination of the nanotubes, they were able to achieve a 30% increase in the elastic modulus of an epoxy composite with the addition of only 1% weight fraction (wt.) of SWCNTs. Functionalization is an excellent method because it allows one to modify nanotubes with functional groups that offer the best bonding for any specific matrix material, and it only has a small effect on the properties of the nanotube itself. Garg and Sinnot [23] report that even a high degree of sidewall functionalization will degrade the mechanical strength of SWCNTs by only 15%.

The second obstacle is that of dispersion. Due to the extraordinarily large aspect ratio of SWCNTs, up to 1,000, nanotubes tend to agglomerate to form ropes or bundles by means of intrinsic Van der Waals attraction [24]. One rope can contain hundreds of nanotubes, but the nanotubes can readily slide relative to each other due to the low shear modulus of the bundles [25-27]. This fact prevents good dispersion of nanotubes in the matrix and not only limits the reinforcing capabilities of the CNTs, but it can actually degrade the initial properties of the bulk matrix material alone. Many methods have been studied to

address this problem including ultrasonication, high shear mixing, surfactants, functionalization, and several others [22]. The most successful method seems to be a combination of the above methods with functionalization playing a primary role.

In addition to dispersion and bonding issues, waviness and alignment are other major challenges faced by experimentalists. A large number of studies have been published researching methods of better aligning nanotubes in a composite. The methods of electrospinning, magnetic field inducing, liquid crystal inducing, shear flow, extrusion or ejecting, melt spinning, and mechanical stretching are among many that have been explored [17,22]. Furthermore, lone carbon nanotubes, even in composites, are generally assumed to be straight and are often modeled as such. In actuality, only quite short nanotubes, less than about 100 μm , are found to be straight or “quasi-straight” in composites [20]. In fact, when normal nanotubes are incorporated into composites, the bonding with the matrix material in conjunction with curing of the composite, in the case of epoxies, causes waviness to be observed. This is due to the low bending rigidity of carbon nanotubes, of the order of $1 \times 10^{-25} \frac{\text{N}}{\text{m}^2}$ [28]. Additionally, it has been shown that current nanotube fabrication methods result in nanotubes with a large distribution of diameters and lengths [29,30]. This fact will in turn lead to a distribution of waviness exhibited in the nanotubes, increasing with nanotube length. Most current models assume that the nanotubes in the composite are straight due to the computational and theoretical difficulties that arise in accounting for this parameter in their approach. Only a few authors, including Shi et al. for mechanical properties [31], Li et al. for electrical properties [19], and Zhang et al. for thermal properties [32], have incorporated waviness into their models. Neither of these authors studied the mechanical properties of

composites. The model proposed in this paper includes both waviness and alignment in its calculation of thermal and mechanical properties of the composite. This is one of the primary advantages of the proposed model over other current models.

The final obstacle relating to the accumulation of knowledge about the effective properties for different composites is the scale on which experiments must be conducted. Though perhaps less challenging than observing nanotube properties directly, nanocomposite experimentation is difficult because it is both costly and time intensive due to the equipment and methods that must be used. While nanotubes are costly by themselves, the fabrication of the composites is quite difficult and time consuming as well. For polymer composites, which are of considerable interest, most researchers first functionalize the nanotubes, disperse them in an epoxy matrix material, and then cure the resin. Zhu et al. reported this process to take a minimum of 18 hours [22]. Any misstep in the process would require starting over. Then, to perform an analysis on the sample, ATR-FTIR, SEM/EDAX, optical microscopes, DMA systems, and other systems are used [22,33]. Finally, mechanical testing is performed in a variety of ways. The complexity, expense, and time required for this testing are some of the primary motivations for a general model of nanotube composites to be developed.

1.3 Current CNT Composite Models

In pursuing a versatile model, many different models have been developed with a variety of unique approaches. Tserpes et al. [34] developed a multi-scaled modeling approach to

test the tensile behavior of composites in which nanotubes are modeled independently, then approximated as a beam element, and integrated into a representative volume element (RVE) which can eventually be solved using finite element analysis (FEA). Li and Chou [35] presented another multi-scale approach to test compressive behavior. Xiao and Gillespie Jr. [36] reported a nanomechanics model for predicting elastic properties of SWCNTs as composite reinforcement, and then used a micro-mechanics model to calculate the elastic properties of the composite as a whole. Shi et al. [31] used a micromechanics model as well, and include waviness and agglomeration in their calculation of the elastic properties. Song and Youn [37] calculated the effective thermal conductivity of nanotube/polymer composites using the control volume finite element method. All of these models use a single carbon nanotube that traverses the entire RVE. They assume that the effective properties of the composite as a whole can be calculated based on a representative RVE with a single nanotube, primarily due to computational simplicity. This assumption is contended in this paper and is not made by the current model.

Beyond the models that calculate effective properties based upon a single nanotube RVE, there are several models that do not make this assumption. Xue [38] presented a numerical method based on Maxwell theory to calculate the thermal conductivity of nanotube/oil and nanotube/decene composites. Bagchi and Nomura [39] approximated nanotubes as spheroidal inclusions and used effective medium theory to calculate the thermal conductivity of aligned nanotube/polymer composites. One of the most versatile models is presented by Zhang and Tanaka [32]. Using the hybrid boundary node method in conjunction with the Fast Multipole Method, they calculated the thermal properties of

CNT composites while including waviness and alignment for a variety of nanotube configurations. Odegard et al. [40] modeled the nanotubes as an effective continuum fiber using the equivalent-continuum modeling method along with a micromechanics approach to calculate mechanical properties of CNT/polymer composites. Seidel and Lagoudas [41] modeled nanotubes using a composite cylinders approach and used the Mori-Tanaka methods to obtain the effective elastic properties for the composite as a whole. They considered both aligned and randomly oriented nanotubes and also consider nanotube bundling. Finally, Li and Chou presented a model for damage sensing by calculating electrical properties of CNT/glass-fiber composites using the finite element method.

Each of the methods detailed above provide important and unique contributions to the modeling of CNT-reinforced composites, but there is one major aspect that nearly every model excludes; non-linearity. Tserpes et al. [34] are the only known authors who reported a stress-strain curve for their composite calculations, but they considered only a single-nanotube that is perfectly aligned and traverses the entire RVE. Without the consideration of the non-linear elastic properties of the polymer matrix and/or those of the carbon nanotubes themselves, a stress-strain relationship cannot be obtained for the composite. The stress-strain curve is one of the most important properties needed to characterize a composite and is thus the primary motivation and result of the model detailed in this thesis.

The model proposed herein reliably simulates CNT-reinforced composite properties and provides qualitative deformation information regarding the composite structure as a whole. Esteva [42] reported a finite element model in which nanotube-composite

structures are modeled using finite elements and the Embedded Fiber Method, originally developed to model steel bar reinforcements in concrete [43-45]. This useful approach allows a simple square mesh of the entire RVE to be generated, circumventing a complicated meshing process while still producing accurate results. In ordinary FEM routines, human intervention must take place to locate fiber-mesh interfaces and to increase the mesh refinement in these areas. The simple square mesh used by the EFM allows for an RVE with a realistic volume fraction of nanotubes and the addition of non-linearity to be modeled with a reasonable amount of computational effort. This model includes the consideration of nanotube waviness and alignment as well. This concept, when applied to nanotube-composites, is novel and effective. Esteva was able to calculate the effective modulus of elasticity and thermal conductivity of a nanotube/polymer composite, but his model did not include a non-linear stress-strain relationship or a non-linear thermal conductivity. The proposed model builds upon the work of Esteva, but it also incorporates the non-linear elastic properties of polymer composites using an incremental approach, and studies the non-linear thermal properties of SWCNTs using both incremental and iterative approaches. The non-linear elastic approach allows the calculation of stress-strain relationships along with descriptive deformation behavior before and after the onset of plastic deformation of the composite. The non-linear thermal approach allows for the effect of non-linear thermal conductivity to be examined and its relevance in modeling to be discussed. In addition to the non-linear issues, the model herein proposes the introduction of several realistic parameters, including length and diameter distributions of SWCNTs as well as a more accurate model of nanotube waviness. Each of these aspects is considered to make the model versatile

with the ultimate goal of producing a model that closely agrees with experimental results. In the numerical results section of this thesis, a comparison to the experimental results of Sun et al. [46] and Zhu et al. [17,22] is presented for the stress-strain relationships calculated by the proposed model. The effective thermal conductivities calculated by the model are also compared to six different experiments [16,47-51].

Chapter 2

The Representative Volume Element

The herein proposed approach is based on a two-dimensional finite element model of the composite structure. The properties of the composite structure as a whole are represented by a representative volume element (RVE) of dimension $1\ \mu\text{m} \times 1\ \mu\text{m} \times 5\ \text{nm}$. The small thickness approximates a two dimensional structure which is adopted for simplicity. There are three distinct steps in the proposed model; geometry generation, fiber portioning, and finite element analysis. First, to generate the nanotube geometry of the RVE, the positions and orientations of nanotubes in the RVE, up to the desired volume fraction, are randomly generated. Second, the RVE is divided into a square mesh of elements and the fibers are partitioned, or divided, according to which element they fall in. The refinement of this square mesh necessary for accurate results is one of the objects of study in this report. Finally, the mechanical or thermal properties of the nanotubes in each element are integrated into the composite matrix properties, based upon which kind of study is being performed, and non-linear finite element analysis is utilized to find either the stress-strain relationship and deformation behavior, or the thermal conductivity of the embedded fiber composite.

2.1 Geometry Generation

The first step in accurately modeling any composite material is to realistically model the geometry of the reinforcing agents. Due to the many advances that have been made in dispersing nanotubes and breaking up ropes and agglomerates [52,53], as well as the effects that these factors have on effective composite properties [54], a geometry of lone nanotubes is assumed. To generate an accurate geometry within the RVE, the parameters of nanotube length, diameter, and waviness are integrated into the model.

In any individual batch of carbon nanotubes, varying according to method of fabrication, lengths of individual nanotubes vary anywhere from less than 100 nm to over 1 μm. Both Wang et al. [29] and Ziegler et al. [30] reported statistically accurate length measurements of a large number of nanotubes. Wang et al. reported a Weibull distribution of lengths with scale and shape parameters of $\alpha = 5 \times 10^{-6}$ and $b = 2.4$, respectively [29]. The probability and cumulative density functions (PDF and CDF) for a Weibull distribution are given by, respectively, by the equations

$$f(x) = \frac{\gamma}{x} \left(\frac{x}{\alpha} \right)^{\gamma} e^{-\left(\frac{x}{\alpha} \right)^{\gamma}} \text{ and } F(x) = 1 - e^{-\left(\frac{x}{\alpha} \right)^{\gamma}}. \quad (1)$$

Isolating x in the CDF gives the equation

$$x = -\alpha [\ln(1 - u)]^{\frac{1}{\gamma}}, \quad (2)$$

where x is a random number from a Weibull distribution and u is a random number from a uniform distribution. This method is known as the inverse transformation method and is simple and useful for generating random numbers from arbitrary distributions. In this notation, α and γ are related to the scale and shape parameters reported by Wang et al. in the following manner:

$$\alpha = e^{-\frac{\ln \gamma}{b}}, \gamma = b. \quad (3)$$

Using the above information, along with minimum and maximum nanotube lengths of 20 nm and 800 nm, respectively, the length of each nanotube in the proposed model is randomly generated from a Weibull distribution using the inverse transformation method. A histogram of 1,000 random lengths generated using these Weibull parameters is shown in Figure 1 to demonstrate the effectiveness of this technique.

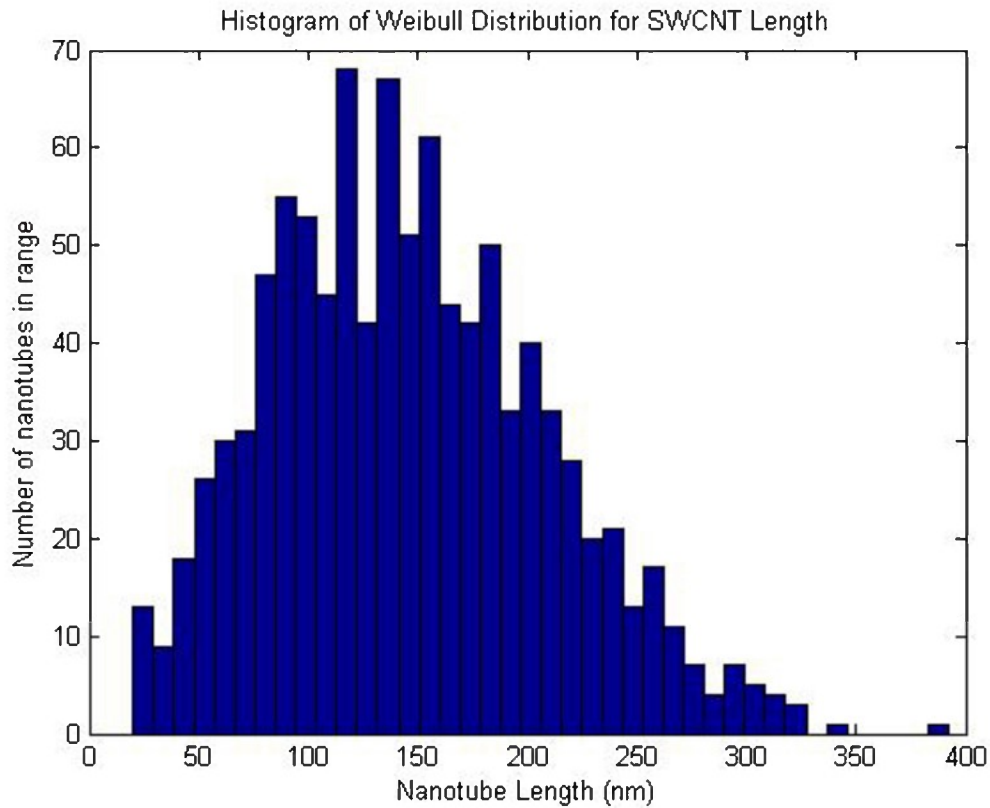


Figure 1. A histogram of 1,000 Weibull randomly generated nanotube lengths.

Other authors have reported a distribution of nanotube diameters in addition to nanotube lengths. Theoretical diameters of carbon nanotubes range from about 0.5 nm to 7.5 nm as reported by Pipes et al. [55]. Experimentally fabricated nanotube diameters of more than 5 nm have been reported, but an average diameter between one and two nanometers is reported by several authors in any given batch of nanotubes, for a variety of fabrication methods [56,57]. In addition to length distribution, Ziegler et al. [30] also reported a distribution of individual nanotube diameters which ranges from approximately 0.5 nm to 2 nm. The general PDF and CDF for a lognormal distribution are given, respectively, by the equations

$$f(x) = \frac{1}{\sigma x \sqrt{2\pi}} e^{-\frac{(\ln x - \mu)^2}{2\sigma^2}} \text{ and } F(x) = \frac{1}{2} + \frac{1}{2} \operatorname{erf}\left[\frac{\ln x - \mu}{\sigma \sqrt{2}}\right]. \quad (4)$$

Solving the CDF for x yields the equation

$$x = e^{(\sigma \sqrt{2} \operatorname{erfinv}[2u-1] + \mu)}, \quad (5)$$

where x is a random number from a lognormal distribution and u is a random number from a uniform distribution..

Ziegler et al. did not report the σ and μ parameters for their lognormal calculation, but they did report a histogram of their diameter distribution data. Using Matlab's "dfittool" capability, a distribution fit is performed on their histogram to calculate these parameters. This fit is shown in Figure 2.

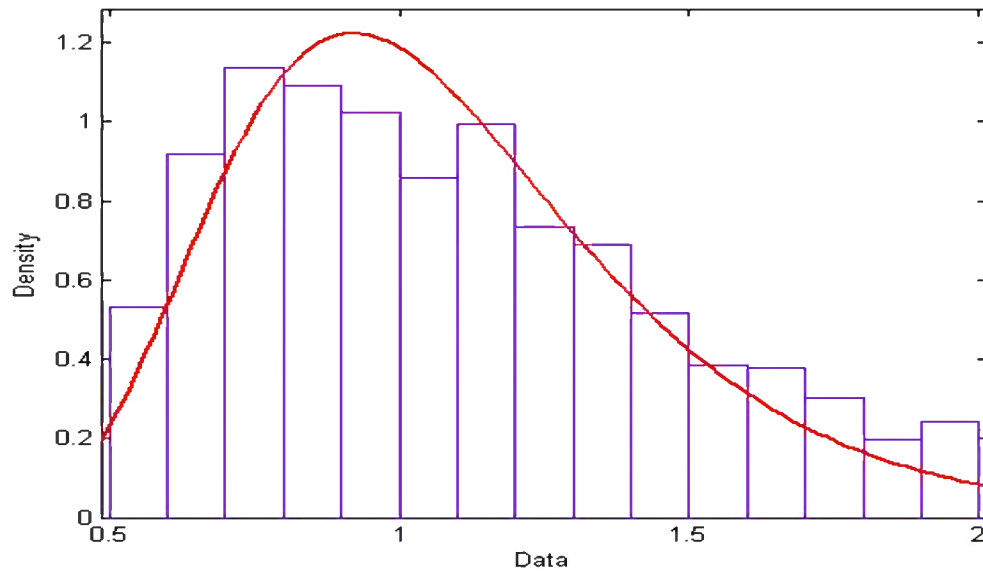


Figure 2. Lognormal distribution fit to the diameter data reported by Ziegler et al. [29].

The parameters of μ and σ are found to be, respectively, 0.02847 and 0.33637. Using these parameters, a random diameter for each nanotube was generated, with a lower limit of 0.5 μm , as supported by Ziegler et al. and by theoretical computations. It is important to note, however, that this diameter is not the effective diameter that is incorporated into the calculation of the volume that each nanotube occupies. When dealing with nanocomposites, the actual distance of atomic bonds must be considered because it is of significant size compared to the diameter of the particles. In this particular case, the carbon-carbon bond spacing between the nanotubes and the polymer matrix must be considered in the calculation of the effective volume occupied by the nanotubes. A carbon-carbon bond is approximately 0.34 μm in length, thereby increasing the effective diameter of each nanotube by 0.68 μm . A diagram of this effect is shown in Figure 3.

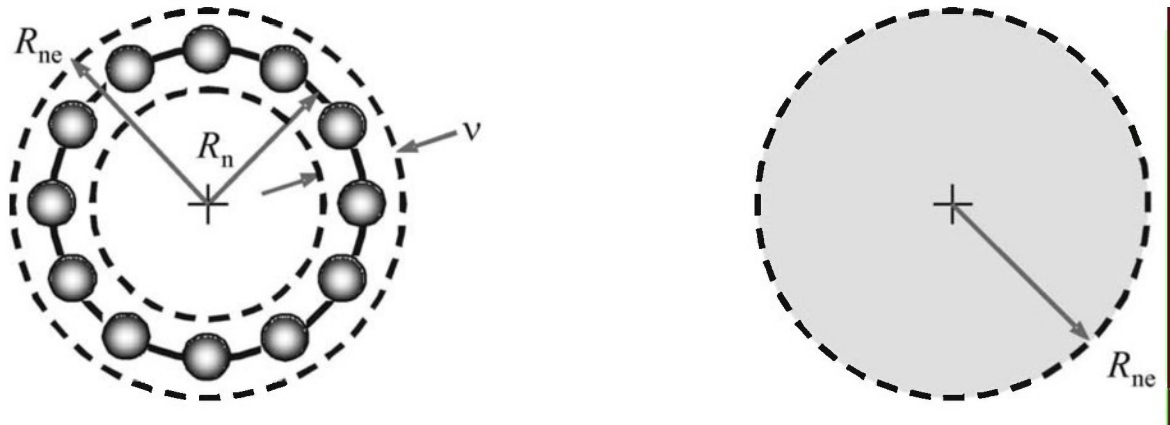


Figure 3. The effective diameter of SWCNT as reinforcement is increased due to the carbon-carbon bonding between the nanotube and the matrix. The actual nanotube diameter is depicted as R_n and the effective diameter including the carbon-carbon spacing is shown

This effect is incorporated into the random diameter generation but is ignored in the random length generation. This is done because the 0.68 μm length scale is significant when compared to the average diameter of approximately 1 μm but not significant when compared to the average length of approximately 200 μm . A histogram of 2,000 random effective diameters is shown in Figure 4 to demonstrate this distribution.

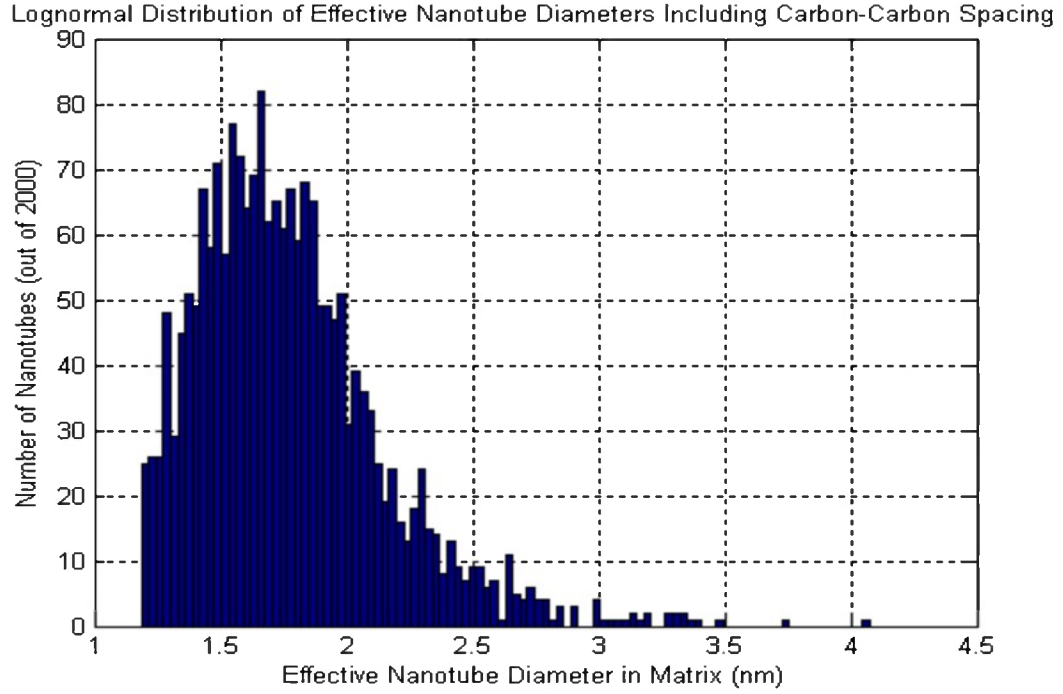


Figure 4. A histogram of the lognormal random effective diameters generated using the parameters from Ziegler's paper [29] are presented, including carbon-carbon spacing.

The final parameter that is incorporated into the geometry generation of the nanotubes is waviness. As mentioned in the introduction, waviness can be considered a function of length. To incorporate this into the model, each nanotube was divided into ten segments, which are computationally treated as individual fibers. Each segment is straight and there is an angle of deviation between each segment. This angle is random, varying uniformly between $-\frac{\Theta_{max}}{2}$ and $\frac{\Theta_{max}}{2}$, where Θ_{max} is some upper limit. The upper limit of the angle is determined by the nanotube length. Due to insufficient experimental data on the subject, a linear model of waviness is assumed and thus the function for the maximum angle of deviation between any two segments for a particular nanotube is given as

$$\Theta_{max} = \frac{180^\circ}{\text{upper length limit}} \times \text{actual nanotube length.} \quad (6)$$

With these concepts in place, the geometry generation routine is implemented with relative ease. The positions of each nanotube are generated randomly throughout the RVE and any time a nanotube segment ends outside of the RVE, that nanotube is ended and a new nanotube is begun. With the diameter and length of each nanotube stored, the volume of each nanotube is easily calculated. The generation process continues until the desired volume fraction is reached. Any individual complete geometry generation is referred to as a microstructure. A single RVE microstructure with 0.0089% volume fraction (1% wt.) of nanotubes in place is illustrated in Figure 5.

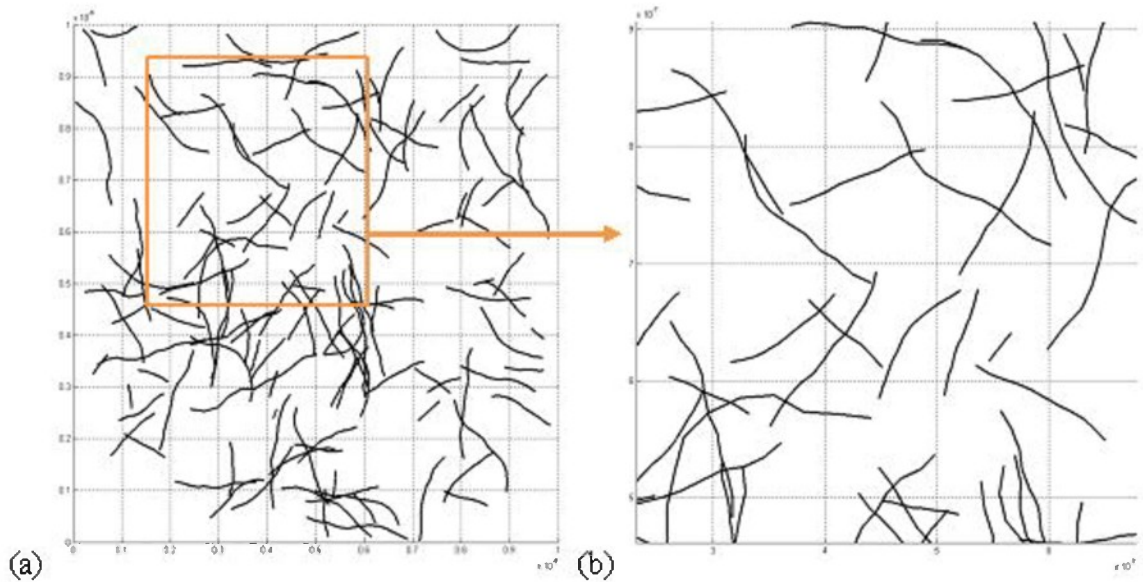


Figure 5. (a) A single, full RVE with 0.0889% v.f. nanotubes is depicted. (b) A close-up view of one section of the RVE is shown. The waviness of the nanotubes is easily observed. Longer nanotubes are wavier than shorter nanotubes to simulate the physical phenomenon.

It should also be noted that most authors report the weight fraction of nanotubes rather than the volume fraction. The conversion between the two quantities is not difficult as long as the densities of the nanotubes and matrix material are known. These are input parameters that are easily changed in the model depending on what type of nanotubes and

what composite matrix material are desired. The conversion from weight fraction to volume fraction is given by the equation [55]

$$v_{f_{nt}} = \frac{w_{f_{nt}} \rho_{matrix}}{w_{f_{nt}} \rho_{matrix} + (1 - w_{f_{nt}}) \rho_{nt}}, \quad (7)$$

where $w_{f_{nt}}$ is the weight fraction of nanotubes, ρ_{matrix} is the density of the polymer matrix, and ρ_{nt} is the density of the nanotubes.

2.2 Fiber Partitioning

After generating the nanotube geometry for any single microstructure, it becomes necessary to partition each nanotube because of the nature of the fiber embedment. Partitioning is a process in which reinforcing fibers that cross the boundaries of one element into another element are divided at that boundary. In finite element analysis, the RVE is divided into many elements. These elements allow for the calculation of mechanical displacements, temperature values, or any other number of quantities, depending on the fundamental equation you are seeking to solve, to be found at finite points throughout the RVE. The accuracy of FEA increases with the number of elements, but each element adds additional degrees of freedom to the system that must be solved, thereby increasing the computational time required to solve the problem. After the initial geometry generation, each nanotube is divided into ten segments to incorporate waviness, as described above. A visualization of this initial division is shown in Figure 6.

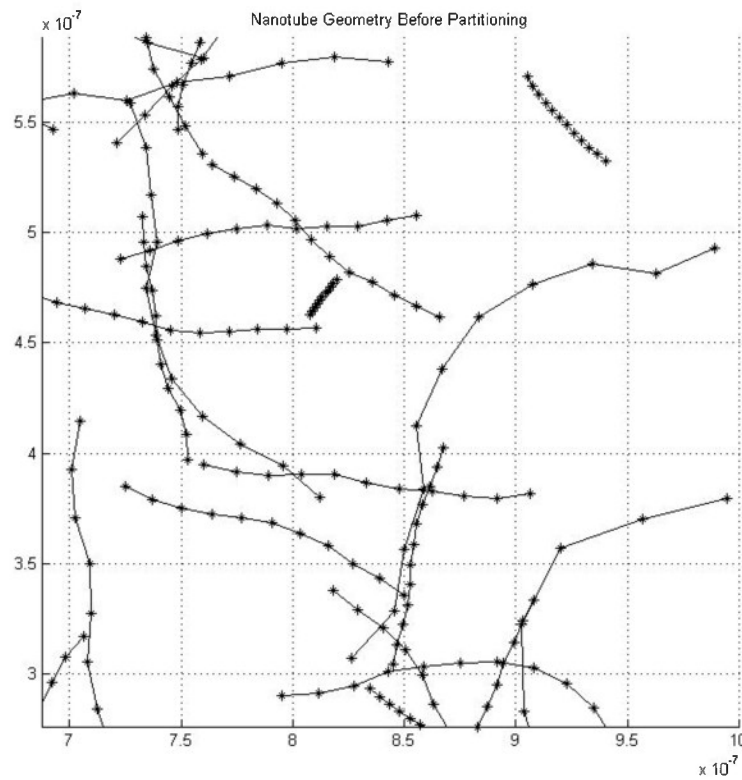


Figure 6. The nanotube geometry of a small section of an RVE before fiber partitioning is presented. The nanotubes are divided into ten segments each, with an “x” marking the end of each segment.

However, to perform FEA, only the properties of the matrix and the reinforcing fibers that lie in each particular element are of use. Thus a fiber that begins in one element and ends in a neighboring element would need to be partitioned at the point it crosses the element boundary into two, separate, shorter fibers. If the entire fiber is included in every element in which it passes, the reinforcing properties of that fiber would be grossly overestimated. It can be imagined then that one fiber can potentially cross several element boundaries, thus being divided several times, especially as the number of divisions within the RVE increases. Though this is not physically precise, this method has been shown to be computationally accurate and must be used for the Embedded Fiber Method (EFM), which will be discussed in the following section. The partitioning

algorithm used in the current model is taken from the work of Esteva [42] and based upon the work of Ranjbaran [44,45]. It is important to note that although the fibers are divided into essentially smaller fibers by partitioning, none of the waviness and length distribution information is lost because this is all taken to account in the geometry generation process. A sample microstructure is presented in Figure 7 to illustrate the concept of fiber partitioning.

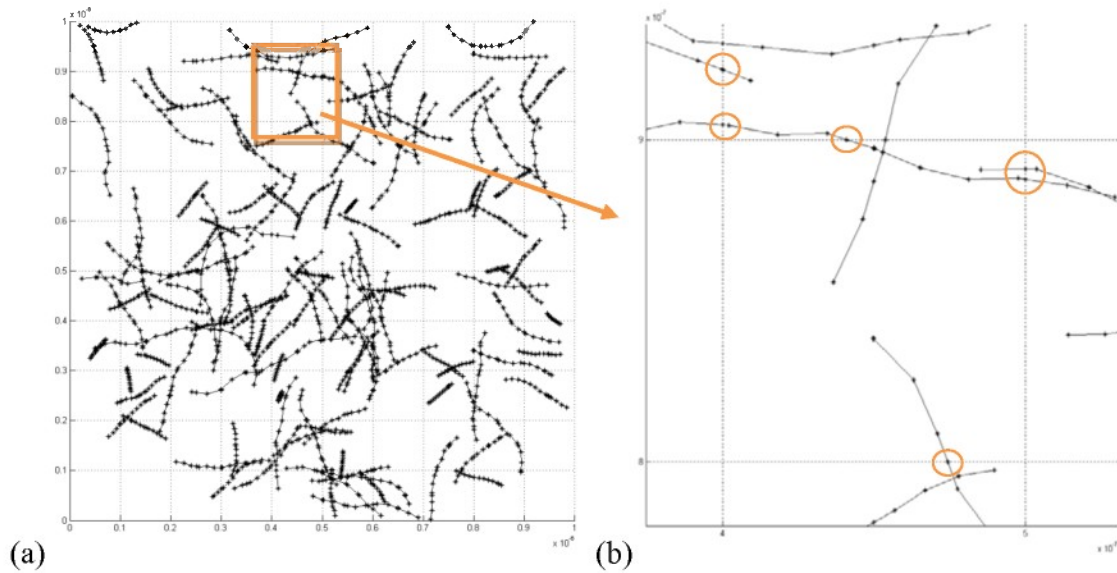


Figure 7. (a) A visualization of the same microstructure as Fig. 5 with “x’s” marking the division of individual nanotubes into segments. (b) A magnified view of one region of the RVE. The circles represent segments that were partitioned because they crossed element boundaries.

After generating the geometry and partitioning the nanotubes for an RVE, the final step before solving the system using the Finite Element Method is to incorporate the reinforcing properties of the nanotubes into those of the bulk matrix material. This is accomplished using the Embedded Fiber Method.

2.3 The Embedded Fiber Method

As mentioned in the introduction, the Embedded Fiber Method (EFM) was originally developed for the Finite Element Analysis of steel-rod reinforced concrete by Ranjbaran [44,45]. The fundamental principle behind this method is the assumption of perfect bonding between the bulk matrix material and the reinforcing structures, thus allowing the direct addition of the stiffness characteristics, or any other property, to those of the matrix material. With the recent advancements in nanotube functionalization and interfacial bonding mentioned in the introduction, this assumption is justified for the case of functionalized CNT composites. To illustrate the general process, a brief description of the process for the elastic case is presented.

The stiffness characteristics of the fibers and matrix alone are calculated using the traditional finite element formulation. The stiffness matrix for an isotropic material element is given by the equation

$$[K]_{mat}^e = h \int_A [B]^e [D] [B]^T d\alpha = \iint_{\Omega} [B]^e [D] [B]^T J ds dt, \quad (8)$$

where the strain matrix B , the material matrix D , and the Jacobian matrix J are given, respectively, by

$$B^e = \begin{bmatrix} du/dx \\ dv/dy \\ du/dy + dv/dx \end{bmatrix} = \quad (9)$$

$$\begin{bmatrix} \frac{dN_1}{dx} & 0 & \frac{dN_2}{dx} & 0 & \frac{dN_3}{dx} & 0 & \frac{dN_4}{dx} & 0 \\ 0 & \frac{dN_1}{dy} & 0 & \frac{dN_2}{dy} & 0 & \frac{dN_3}{dy} & 0 & \frac{dN_4}{dy} \\ \frac{dN_1}{dy} & \frac{dN_1}{dx} & \frac{dN_2}{dy} & \frac{dN_2}{dx} & \frac{dN_3}{dy} & \frac{dN_3}{dx} & \frac{dN_4}{dy} & \frac{dN_4}{dx} \end{bmatrix},$$

$$D = \frac{E}{1-\nu^2} \begin{bmatrix} 1 & \nu & 0 \\ \nu & 1 & 0 \\ 0 & 0 & \frac{1-2\nu}{2} \end{bmatrix}, \quad (10)$$

$$I = \begin{bmatrix} dx/dr & dy/dr \\ dx/ds & dy/ds \end{bmatrix}. \quad (11)$$

Equations (9), (10), and (11) represent the matrices for the two-dimensional plane stress FEA problem, which is what the current model is solving. In Equation (10), E is the modulus of elasticity of the matrix material and ν is Poisson's ratio. For a four-noded quadrilateral element with two degrees of freedom per node, there are four shape functions used to map between the local parametric coordinates r and s and the global coordinates x and y . These shape functions are seen in Equation (9) and are given by

$$[N] = [N_1 N_2 N_3 N_4]^T, \quad (12)$$

$$N_1 = \frac{1}{4}(1-r)(1-s), \quad (13)$$

$$N_2 = \frac{1}{4}(1+r)(1-s), \quad (14)$$

$$N_3 = \frac{1}{4}(1+r)(1+s), \quad (15)$$

$$N_4 = \frac{1}{4}(1-r)(1+s), \quad (16)$$

These shape functions allow the mapping of local coordinates to global coordinates using the equations

$$x(r,s) = [N][u] \text{ and } y(r,s) = [N][v], \quad (17)$$

where u and v are the x and y coordinates of the element nodes, respectively. In other words, by using the shape functions in Equations (13) through (16), the x and y positions corresponding to any parametric point (r,s) can be found easily using Equation (17).

Furthermore, the local derivatives are mapped to global derivatives using the Jacobian from Equation (11) and the derivatives of the shape functions. This mapping is given by the equation

$$\begin{bmatrix} dN/dx \\ dN/dy \end{bmatrix} = [J]^{-1} \begin{bmatrix} dN/dr \\ dN/ds \end{bmatrix}. \quad (18)$$

With these derivatives and coordinates in hand, the strain matrix and stiffness matrix for an element are easily calculated. Due to the discrete nature of FEA, the integral of Equation (8) is determined numerically using Gaussian quadrature. For any particular element, the shape functions and the Jacobian are evaluated at each of the Gaussian quadrature points within the element and summed. For a two-dimensional square element, as is the case in the present model, these points are given as

$$\xi = \eta = \pm 1/\sqrt{3}. \quad (19)$$

The stiffness matrix can now be written as

$$[K]_{mat} = h \sum_{i=1}^n \sum_{j=1}^n w_i w_j [B(s_j, r_j)] [D] [B(s_j, r_j)]^T [J(s_j, r_j)] \quad (20)$$

These finite element formulations can be found in any standard Finite Element Method book, such as those by Akin [58], Desai and Abel [59], and Zienkiewicz et al. [60].

With the ability to calculate the stiffness matrix for the bulk matrix material, it is now necessary to calculate the stiffness matrices for the reinforcing fibers. In the current model, the nanotubes are approximated as line elements. This approximation is accurate

and economical as shown by Konrad and Graovac [43]. With this approximation, the stiffness matrix of a one-dimensional fiber, expanded using zeros to two dimensions, is given as

$$K_{fib_L} = \frac{EA}{L} \begin{bmatrix} 1 & 0 & -1 & 0 \\ 0 & 0 & 0 & 0 \\ -1 & 0 & 1 & 0 \\ 0 & 0 & 0 & 0 \end{bmatrix}. \quad (21)$$

This general stiffness calculation is for a fiber that is oriented in the local, positive x -direction. In Equation (21), A is the cross-sectional area of the fiber and L is the fiber length. To transform this matrix from its local system to the global coordinate system, accounting for the true alignment of the nanotube, a matrix of direction cosines is easily employed using the equation

$$K_{fib_G} = [C][K_{fib_L}][C]^T \text{ with} \quad (22)$$

$$[C] = \begin{bmatrix} \cos t & \sin t & 0 & 0 \\ -\sin t & \cos t & 0 & 0 \\ 0 & 0 & \cos t & \sin t \\ 0 & 0 & -\sin t & \cos t \end{bmatrix}.$$

In Equation (22), t is the angle between the fiber and the positive x -axis of the global coordinate system.

The next step to prepare the fiber's stiffness matrix to be embedded with the bulk material's stiffness matrix for a single element is to map the physical coordinates of the fiber endpoints to the corresponding parametric coordinates. The parametric coordinates of the fiber endpoints are found using a Newton-Rhapson scheme which is shown in Appendix A.

Finally, the full, global stiffness matrix for a single fiber in a single element can be found by interpolating the fiber's properties that are given in Equation (22) to the nodes of the

element under consideration. This is accomplished by utilizing the transformation matrix T with the equation

$$K_{fib} = [T][K_{fib_c}][T]^T, \text{ where} \quad (23)$$

$$[T] = \begin{bmatrix} N_1(r_1, s_1) & 0 & N_2(r_1, s_1) & 0 & N_3(r_1, s_1) & 0 & N_4(r_1, s_1) & 0 \\ 0 & N_1(r_1, s_1) & 0 & N_2(r_1, s_1) & 0 & N_3(r_1, s_1) & 0 & N_4(r_1, s_1) \\ N_1(r_2, s_2) & 0 & N_2(r_2, s_2) & 0 & N_3(r_2, s_2) & 0 & N_4(r_2, s_2) & 0 \\ 0 & N_1(r_2, s_2) & 0 & N_2(r_2, s_2) & 0 & N_3(r_2, s_2) & 0 & N_4(r_2, s_2) \end{bmatrix}$$

In Equation (23), r and s represent the local parametric coordinates of the fiber endpoints. Having introduced this final transformation, the fiber's properties can now be incorporated into those of the bulk matrix material using simple addition:

$$[K]_{embedded} = [K]_{mat} + [K]_{fib}. \quad (24)$$

It is important to note here that while the above steps are described for the case an elastic problem, this method is truly versatile and may be used with minimal change for thermal, electrical, or various other problems.

The Embedded Fiber Method is a bit daunting at first glance. Not only are there numerous equations to take into consideration, but this process must be accomplished for every fiber in an element as well as for every element in the RVE. However, the benefits achieved by accomplishing this extra work are indeed significant. The primary advantage is that the EFM allows the use of constant quadrilateral elements. Most models that use FEA must utilize intense mesh refinement along the nanotube/matrix boundaries in order to accurately capture the load transfer properties of the interface. For example, a picture of the finite element mesh used by Li and Chou [19] in their model is shown in Figure 8.

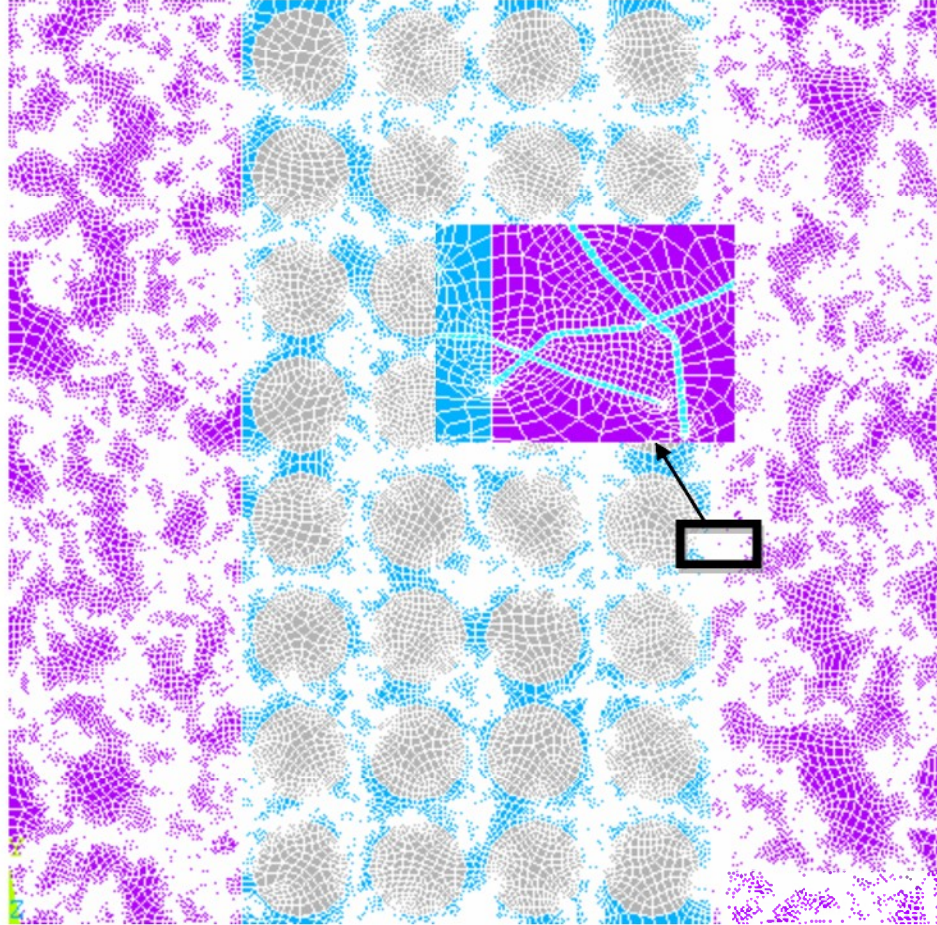


Figure 8. The finite element mesh of the carbon nanotube/fiber cross-ply composite used by Li and Chou [19]. The intense mesh refinement along the nanotube matrix boundaries is to be noted.

By utilizing a constant quadrilateral mesh, accurate results can be found without the costly human intervention of most other models. For example, the model of Li and Chou shown above uses approximately 357,000 elements and 360,000 nodes to achieve their results [19]. The fiber-matrix interfaces must be identified and the mesh must be refined in those areas. When compared to the 3,600 elements and 3,721 nodes needed for accurate results in the current model, the advantages of the Embedded Fiber Method become quite clear. For the thermal model with one degree of freedom per node, there are approximately 100x fewer equations to solve in the proposed model. There are about

200x fewer equations to solve for the elastic problem. No attempt to quantify the time saved by eliminating the human intervention process is made herein. However, the complete automation of the process by using the EFM is undoubtedly useful.

Without the Embedded Fiber Method, it is extremely difficult to accurately model any significant volume fraction of nanotubes because the computational time is simply too great. When considering non-linear properties, the number of equations to be solved is multiplied by the number of iterations or incremental steps employed. The Embedded Fiber Method is the only practical solution to evaluate the non-linear properties of a CNT-reinforced composite on a scale larger than only a few nanotubes and is thus utilized by the model proposed in this paper.

Chapter 3

The Non-Linear Finite Element Model

Having established the Embedded Fiber Method as the procedure for incorporating the physical properties of the nanotubes into the bulk composite material properties, the proposed method can now be detailed. Esteva [42] developed this model using the Embedded Fiber Method with the goal to determine the effective elastic and thermal properties of the composite. Using a linear model, the RVE was displaced to 5% strain and the reactions at the fixed bottom nodes were used to calculate the effective modulus of elasticity. Similarly, a temperature gradient was applied between the upper and lower boundaries and heat flux at the lower nodes was used to calculate the effective thermal conductivity. While this model made a significant advancement in the area of composite modeling, one of the primary tools used by researchers to describe a new or existing material is its stress-strain curve. By adopting a linear solution, it is not possible to accurately capture the non-linear properties of the polymer matrix or those of the nanotubes themselves. The proposed model explores both of these non-linearities and how they affect the thermal and elastic properties of the composite as a whole. First, the relevant non-linearities are identified. After identifying which non-linearities to consider, the various non-linear solution techniques are discussed and how they are applied to the

proposed model. Finally, the specific details of the model are discussed along with the parameters chosen for experimental comparison.

3.1 Non-Linearity of Carbon Nanotubes and Epoxies

The non-linear elastic and thermal properties of carbon nanotubes are well documented in the literature, both theoretically and experimentally. For the non-linear elastic properties, Tserpes et al. [34] presented a detailed finite element model of lone nanotubes using a structural mechanics approach. They identify the stress-strain relationship for armchair and zigzag SWCNTs. Additionally, Tserpes et al. [6] presented a progressive fracture model to calculate the stress-strain relationship for SWCNT's with perfect structures and for those with imperfections. Belytschko et al. [7] developed a molecular mechanics model to simulate nanotube fracture. They reported the stress-strain curve for perfect and imperfect zigzag nanotubes as well as a curve for various different perfect nanotube structures. Natsuki et al. [4] described a structural mechanics approach to modeling nanotube elastic properties. Finally, Meo and Rossi [5] presented a molecular-mechanics based FEM for the prediction of SWCNT elastic properties. Each of these models takes a slightly different approach, but they all identify $\approx 10\text{-}15\%$ strain as the region where significant non-linear behavior is first exhibited by SWCNTs.

The non-linear thermal properties of SWCNTs have also been modeled, though less frequently than the elastic properties. Grujicic et al. [15] presented a molecular dynamics based model of the thermal conductivity of SWCNTs in which they investigate the non-linear dependence of thermal conductivity on temperature. The strong dependence they

report is depicted in Figure 9 and is the motivation for the non-linear thermal analysis performed in this paper.

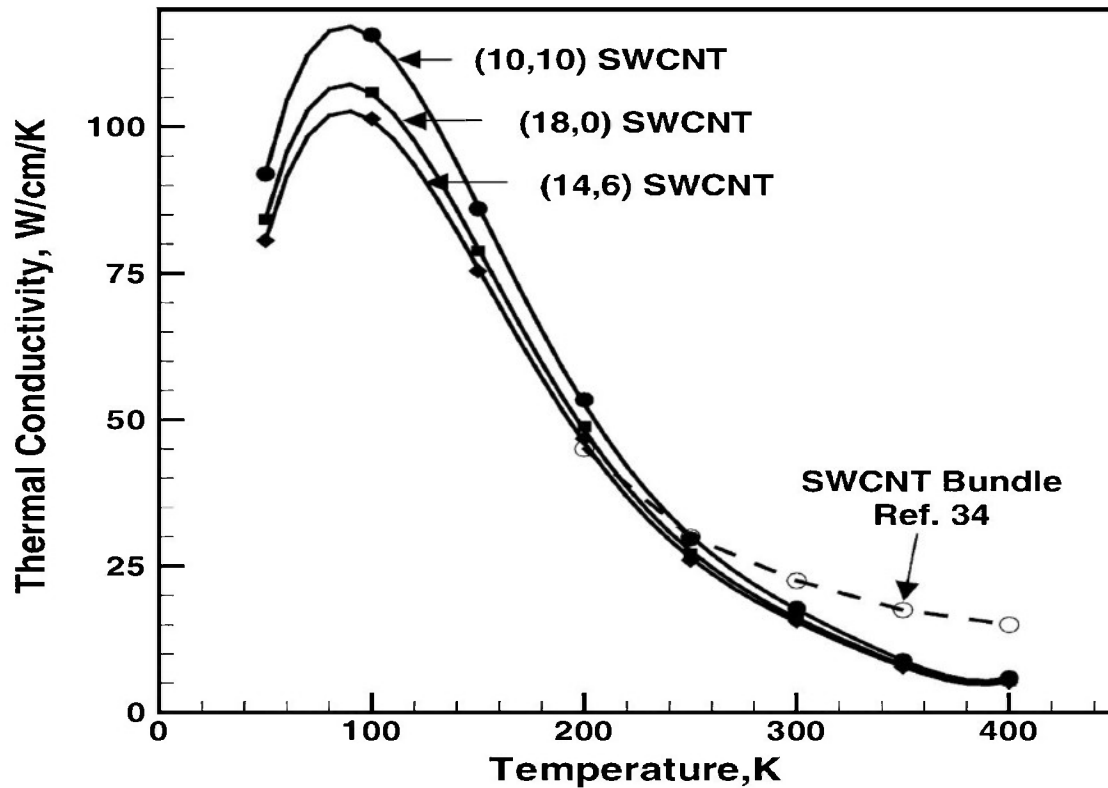


Figure 9. The non-linear thermal properties of SWCNTs are shown in the analysis of Grujicic et al. [15].

Kawamura et al. [61] also reported the temperature dependence of SWCNT thermal conductivity using a molecular dynamics simulation. Additionally, Xu et al. [47] reported this effect indirectly by reporting the temperature dependence of the thermal conductivity of composites reinforced with SWCNTs.

Along with the theoretical modeling evidence presented above, experimental evidence corroborates the non-linear thermal and elastic properties of SWCNTs. Yu et al. [8,27] performed tensile load testing using an AFM tip to document the non-linear stress-strain relationship of SWCNTs. Their results show the onset of non-linear behavior to occur at greater than 10% strain. Walters et al. [26] also reported the lower bound of the yield

strain of SWCNT ropes to be about 6%. For thermal properties, Shaikh et al. [62] reported a range of thermal conductivities for CNT ropes to range from 0.1-2,000 $\frac{W}{m-K}$.

Epoxy composites exhibit non-linear elastic properties at a much lower strain level. Zhu et al. [17,22] present stress-strain curves for neat epoxy in which non-linearity is shown at 3% strain. Li et al. [63] present similar effects with a load-displacement curve of neat epoxy. Sun et al. [46] and Gojny et al. [54] also indicate 3% strain as the onset of non-linearity in neat epoxy. Each author indicates epoxy failure at less than 6% without reinforcement. The significantly lower onset of non-linear behavior and failure in the epoxy than in the lone nanotubes led to the conclusion that the non-linear behavior of the nanotubes may be ignored and that of the epoxy must be taken into account for an accurate elastic model.

In general, polymers are reported to have constant values of thermal conductivity. Xu et al. [47] reported a constant thermal conductivity of $\approx 0.2 \frac{W}{m-K}$ for their PVDF polymer.

Wang et al. [48] reported a constant thermal conductivity of $\approx 0.18 \frac{W}{m-K}$ for the neat epoxy resin used in their experiments. Moisala et al. [16] reported a constant $\approx 0.255 \frac{W}{m-K}$ for epoxy consisting of a bisphenol-A resin and an aromatic amine hardener.

Du et al. [14] also reported a constant thermal conductivity of $\approx .18 \frac{W}{m-K}$ for their PMMA polymer. Finally, Cai and Song [49] used a semi-crystalline PU dispersion with a constant thermal conductivity of $\approx 0.15 \frac{W}{m-K}$. Because of the lack of any indication of a non-linear temperature dependence of the thermal conductivity of the neat epoxy, only the non-linear thermal conductivity of the nanotubes should be considered for a thermal model of CNT-reinforced polymer composites.

Based upon this review of the non-linear thermal and elastic properties of both carbon nanotubes and polymer matrix materials, it is concluded that the non-linear elastic properties of the epoxy matrix will be included in the elastic analysis of the model presented in this paper and the non-linear thermal properties of the CNTS will be included for the thermal analysis. With these choices made, the next step is to select the non-linear approach to take in each case.

3.2 Non-Linear FEA Solution Techniques

In general, there are two main sources of non-linearity in finite element analysis, as described in references such as Desai and Abel [59]. The first type is called material or physical non-linearity. This type of non-linearity stems from constitutive laws and is inherent in the physical properties of the material. The second kind of non-linearity relates to geometrical considerations. When materials undergo large deformations, the geometry of the material may change drastically and this can alter the equations used to govern the finite element analysis of that body [59]. In both the thermal and elastic cases considered in the present model, material non-linearity is the only aspect considered.

For material non-linearity, Desai and Abel [59] outline three kinds of non-linear solution techniques commonly used for finite element analysis: the incremental approach, the iterative approach, and a mixed approach. In the incremental, or step-wise, approach, the load applied to the system is subdivided into many small increments. In general, these increments do not need to be of the same size. With the application of each load

increment, all the constitutive laws pertaining to the system are assumed to be linear. The results obtained after each step are then used to update the values of the constants used in the previous linear increment based upon a known relationship. For a non-homogeneous material, the constants may vary throughout the body. When applying the iterative approach, the structure is fully loaded during each iteration. After solving the fully loaded system, the constants are then updated based upon the results. In general, equilibrium is not satisfied after each iteration. The non-balanced load is then used to correct the solution until equilibrium is achieved or is sufficiently close based upon predetermined criteria. Finally, a mixed approach is combination of the iterative and incremental approaches. Generally, incremental loads are applied and a number of iterations are applied to each load step [59].

After careful consideration of the above methods, the incremental technique was chosen for the elastic analysis to be performed and both techniques were studied for the thermal analysis. The incremental technique was chosen both for its versatility and because it most closely resembles the physical phenomenon of a tensile strain test. The iterative technique is not applicable in the elastic analysis of the current model because it does not provide any information about the stresses and strains at intermediate load increments. Thus, a stress-strain relationship cannot be obtained from an iterative approach in the elastic case. In addition, the availability of experimental data for comparison contributed to this choice.

For the thermal analysis, both an incremental approach and an iterative approach were taken for comparison. An iterative approach is more readily implemented than an incremental approach and converges more rapidly than the incremental approach. For

this reason, it was utilized to calculate an effective thermal conductivity for the composite. However, there is no guarantee that an iterative technique will converge and it provides no conductivity information at intermediate temperature increments, so an incremental approach was also used.

Upon deciding upon the approaches to select for the thermal and elasticity analyses, a non-linear finite element model was developed, using the Embedded Fiber Method as a foundation. After generating the nanotube geometry, partitioning the fibers, and embedding the fibers, the stiffness matrix of the entire RVE is assembled using the standard finite element procedures outlined in Chapter 2. The standard force balance equation for FEA is given by the equation

$$[K]\vec{u} = \vec{F}, \quad (25)$$

where $[K]$ is the system stiffness matrix assembled from the element stiffness matrices defined in Equation (24), \vec{u} is the displacement or temperature vector for all of the mesh nodes in the RVE, and \vec{F} is the reaction force or temperature gradient vector at the nodes. For the elasticity analysis case, the general finite element problem can be solved in one of two standard ways. The first approach is to prescribe a force to be applied to the structure and then to calculate the resulting displacements at all the nodes. The second approach is to prescribe displacements to specific nodes and then calculate the resulting displacements of all the other nodes. In each method, the final displacements can be used to recover the reaction forces at each of the fixed nodes. The current model uses the displacement-controlled approach because the uniform displacement of an entire edge is needed to generate a stress-strain curve for the RVE as a whole.

To implement the incremental solution technique, displacement increments were applied to the elasticity, problem and temperature increments were applied to the thermal problem. The number of increments necessary for an accurate solution is one of the results of the present report. After each increment is applied, the resulting displacements or temperatures of every node in the mesh are calculated.

For the elasticity case, there are two degrees of freedom per node; x and y displacements. With the displacements at each node in hand after an incremental displacement is applied, the strain at each node can be calculated and interpolated to the Gaussian quadrature points using the strain matrix B from Equation (9), and the equation

$$\vec{\epsilon} = [B]\vec{u}. \quad (26)$$

In two-dimensions, the strain vector $\vec{\epsilon}$ is a three component vector including the strain in the x and y directions, ϵ_x and ϵ_y , as well as the shear strain, γ_{xy} . With the strain, the stress vector at each Gauss point can be calculated using the relation

$$\vec{\sigma} = [D]\vec{\epsilon}. \quad (27)$$

Similar to the strain vector, the stress vector $\vec{\sigma}$ in two-dimensions is a three component vector including the strain in the x and y directions, σ_x and σ_y , as well as the shear stress, τ_{xy} . Recalling the earlier description of the basic finite element method, $[D]$ is the material matrix given in Equation (10). It is worth pausing here to describe the modulus of elasticity E that appears in the material matrix and how it is calculated in the current model. In any linear model, the modulus of elasticity of a solid material is assumed to be constant. For a perfectly elastic material, this modulus can be calculated as the slope of the stress-strain curve for that material. Though no material is perfectly elastic, this assumption is valid for most “nearly” elastic materials. For materials that exhibit non-

linearity, the slope of the stress-strain curve changes as stress levels change. For materials that exhibit plasticity, the curve decreases at the onset of plastic deformation. For work-hardening materials, the slope of the curve may even increase at higher stress or strain levels. The slope of the curve at any given strain level is known as the tangent modulus. In this report, the tangent modulus of a polymer material is a function of strain, not assumed to be constant, and will simply be referred to as the modulus or elastic modulus of the material.

In general plasticity theory, there are two competing ways to categorize whether a material has begun to undergo plastic deformation. The Tresca and von Mises criteria are two different methods which take into account the full stress state at one specific point of a material to come up with a single value which describes the effective stress at that point. The von Mises criterion is the more conservative of the two and is thus employed in the current model. The von Mises equivalent stress in two dimensions is given by the equation [59,64]

$$\sigma_{VMS} = \sqrt{1/2 \left[(\sigma_x - \sigma_y)^2 + \sigma_y^2 + \sigma_x^2 + 6\tau_{xy}^2 \right]}. \quad (28)$$

After finding the strain vector at a node using Equation (26) and using it to find its corresponding stress vector by Equation (27), the von Mises stress at each Gauss point in each element can be calculated using Equation (28). The von Mises stress is then used to refer to the stress-strain curve of the neat epoxy to calculate the tangent modulus at any particular Gauss point. In this manner, the modulus at each Gauss point throughout the RVE can be updated after each displacement increment. This procedure allows the non-linearity of the material to be effectively incorporated into the model. A synopsis of the incremental procedure is presented in Figure 10.

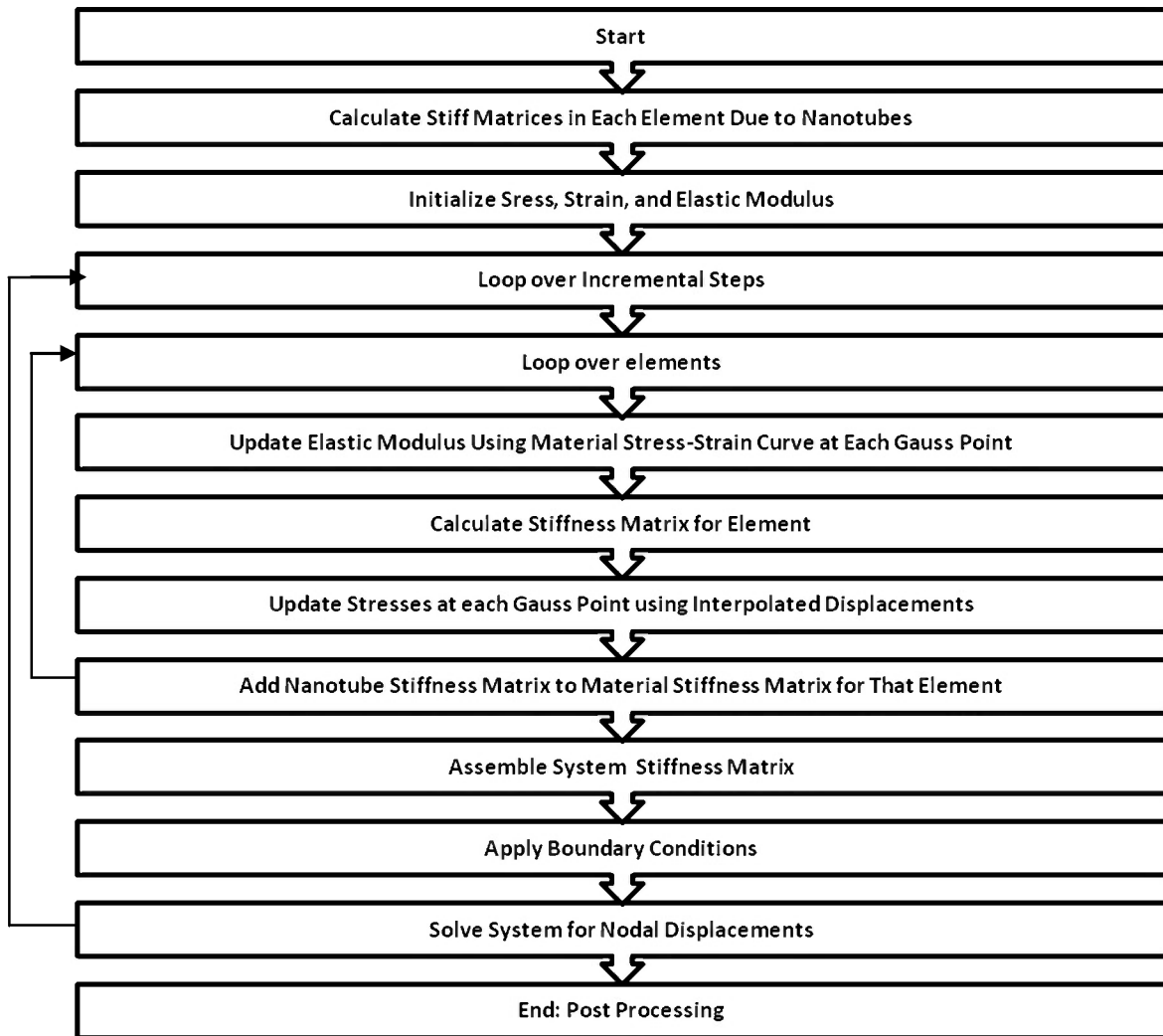


Figure 10. A block diagram of the non-linear incremental scheme for the elastic case is presented. Notice the two major loops which are the driving force behind the computational time required by the model.

For the thermal problem, the incremental approach follows essentially the same approach as the elastic problem, with only a few differences. The first difference between the thermal and elastic problem is that the thermal case requires only one degree of freedom per node, temperature. This in turn greatly reduces the computational cost to solve the problem because the number of equations to solve is halved. The second difference is that instead of updating the elastic modulus of the material, the thermal conductivity of

the nanotubes is updated after each incremental temperature increase. This process is simply performed with the knowledge of the temperature at each of the nodes throughout the RVE. Using the shape functions given in Equations (13) through (16), the temperature is interpolated from the nodal temperatures to define a temperature at each of the nanotube endpoints. Because the nanotube thermal conductivity is quite high, approximately four orders of magnitude greater than that of the polymer matrix, an average of the two nanotube endpoint temperature is assumed as the constant temperature along that nanotube. The thermal conductivity of that particular nanotube is then updated based upon the curve of Grujicic et al. [15] shown in Figure 9. The thermal conductivity is updated using the equation

$$K_{nt} = 3E^{-8}T^5 + 7E^{-9}T^4 - 0.0011T^3 + 0.1568T^2 - 26.503T + 2471.7, \quad (29)$$

where K_{nt} is the thermal conductivity of the nanotube and T is the temperature of the nanotube in degrees Celsius. This process is repeated for every nanotube in each element and is repeated after each incremental temperature step.

In addition to the incremental approach, the iterative technique is also applied to the thermal problem. In this process, the finite element solution is solved in one total temperature increase. Using the temperature data recovered from this solution, the thermal conductivities are updated using the same procedure as the incremental approach. The problem is then solved again using this data. This process is repeated until the solution converges to a solution. The number of iterations required for convergence is one of the results presented in the discussion section of the paper.

Overall, there are two aims to the non-linear analysis that is performed by the proposed model. The first aim is to create a stress-strain curve for any CNT-reinforced polymer

composite. The second aim is to discover whether or not the non-linear thermal properties of carbon nanotubes need to be included in thermal models of CNT/polymer composites. The results of incremental and iterative non-linear approaches are compared for this aim to see if one is superior to the other. However, whatever the results of the model may be, the success of these aims is ultimately determined by whether or not the model accurately represents available experimental results. Due to this fact, the present model is compared to several experiments by incorporating the parameters reported in those studies into the details of the model.

3.3 Details of the Model

With the general procedure detailed above, the two significant attributes of the proposed model should be evident. First and foremost, the model offers the option to to incorporate the non-linear properties of both the carbon nanotubes and the polymer matrix into both thermal and elasticity finite element analysis. Though only the polymer's elastic non-linearity and the nanotubes' thermal non-linearity are incorporated into the present elasticity and thermal analyses, respectively, it would take only minimal modification to incorporate both the non-linear elastic properties of the nanotubes and the thermal properties of the matrix should the specific physical situation require it. For instance, if a different polymer or other material were used in which non-linearity was initiated at a higher strain level, this would make the non-linear elastic properties of the nanotubes relevant, and the same procedure utilized for the present thermal analysis could quickly be used for the new elasticity problem. The same applies for a new thermal situation. The second significant attribute of the proposed model is its inherent

versatility. If it is desired to model a composite fabricated with short-straight nanotubes, such as the ones developed by Li et al. [65] or Jia et al. [66], all that is needed is a change in the parameters of the length distribution described in Chapter 2, Equation (1). This will in turn make the waviness insignificant and short, straight nanotubes will be generated. If it is desired to model a composite with aligned nanotubes, all that is needed is a minor change in the geometry generation section of the model in which the first nanotube segment is always generated in the same direction. Finally, the model is flexible to almost any physical difference in properties among the materials used. The stress-strain curve used to update the elastic modulus of the matrix material is a user-defined parameter and can be readily changed depending upon the material used. If a new or different curve for the thermal conductivity variation of SWCNTs with temperature is specified, the equation used to update the thermal conductivity of the nanotubes readily altered.

With these capabilities in mind, the elastic results of the model are compared to two different experimentally determined stress-strain curves. The first experiment is the tensile test performed by Sun et al. [46] on an epoxy composite reinforced in several different ways. The epoxy used was the EPIK-OTE™ 862 resin cured with the EPIKURE™ W curing agent. The stress-strain curves for the neat epoxy, epoxy with pristine nanotubes, and epoxy with functionalized nanotubes are reported and shown in Figure 11.

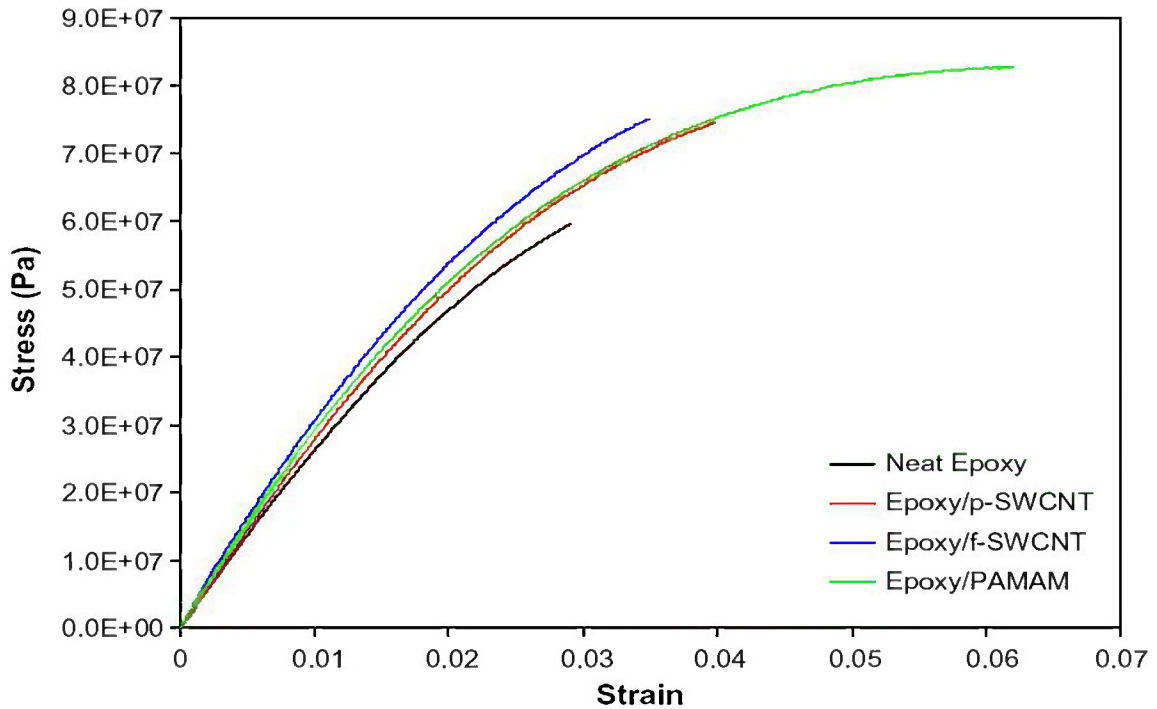


Figure 11. Tensile stress versus strain curves for the various composites reported by Sun et al. are presented [45]. The bottom, black line is used in the current model to update the elastic modulus of the epoxy matrix.

The bottom, black curve for the neat epoxy shown in Figure 11 is used as the reference curve by which the modulus of elasticity is updated in the incremental elastic analysis of the current model. One of the fundamental assumptions of the Embedded Fiber Method is that the reinforcing fibers are perfectly bonded to composite matrix, as explained in Chapter Two. Due to this assumption, the results of the model will be compared to the top, blue stress-strain curve for the epoxy reinforced with 1 wt% functionalized nanotubes.

Using a coordinate finding program developed at Rice University [42], the data points of the neat epoxy curve in Figure 11 were extracted from the reported figure. Using those data points and Matlab's built-in polynomial fitting routine, "polyfit", the cubic stress-strain polynomial is given by the equation

$$\sigma = -3.977E^{11}\varepsilon^3 - 1.573E^{10}\varepsilon^2 + 2.864E^9\varepsilon, \quad (30)$$

with an R^2 value of 0.999. Taking the derivative of this function, the instantaneous tangent modulus of the epoxy matrix is given by the equation

$$\frac{d\sigma}{d\varepsilon} = E_{tan} = -1.193E^{12}\varepsilon^2 - 3.148E^{10}\varepsilon + 2.864E^9. \quad (31)$$

The elasticity problem results of the proposed model are also compared to the work of Zhu et al. [22]. In their experiment, they used a similar epoxy and curing agent to Sun et al. [46] and they also used 1 wt% SWCNT loading. However, they report a different stress-strain relationship for the neat epoxy, allowing the simulation to be continued out to 5% strain. This curve is shown in Figure 12.

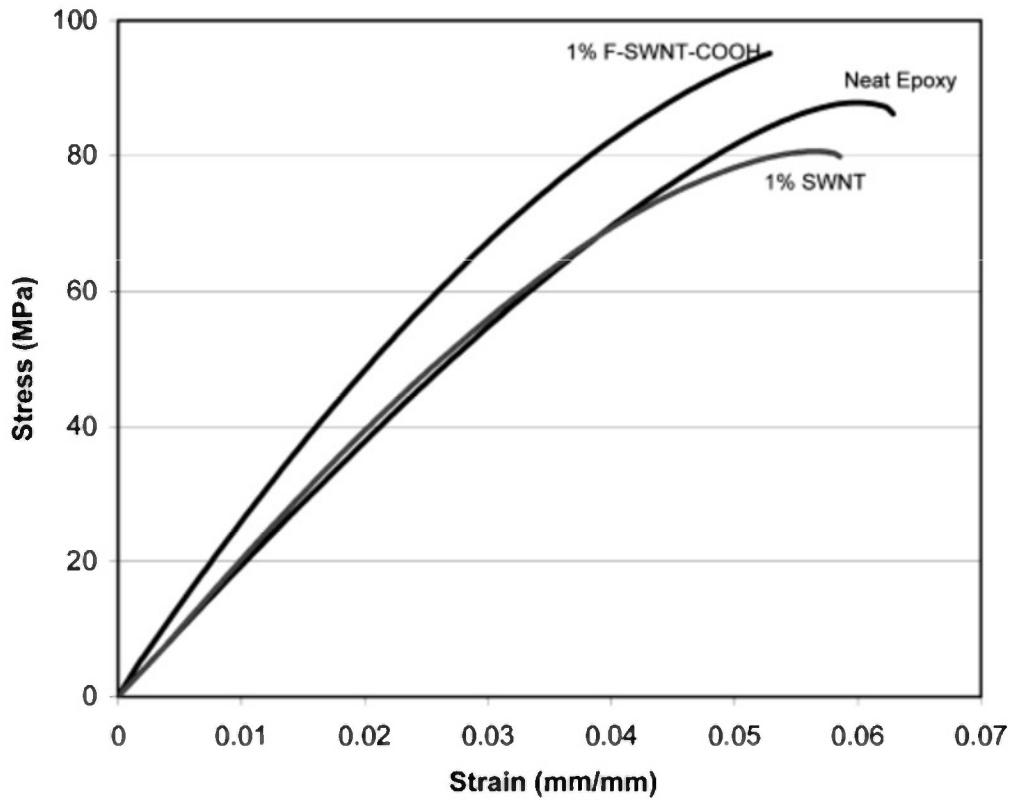


Figure 12. Tensile stress versus strain curves for the composites reported by Zhu et al. are presented [22]. The middle, neat epoxy line is used in the current model to update the elastic modulus of the epoxy matrix.

Using the epoxy curve that Zhu et al. report, the coordinate finding program of Esteva [42] was again employed and the data points for that curve were extracted. Again using Matlab's "polyfit" routine, the stress-strain polynomial fit to the data was found to be given by the equation

$$\sigma = -1.1084E^{11}\epsilon^3 - 4.0E^8\epsilon^2 + 1.93E^9\epsilon. \quad (32)$$

This stress-strain relationship yielded a tangent modulus equation given by

$$\frac{d\sigma}{d\epsilon} = E_{tan} = -3.325E^{11}\epsilon^2 - 8.0E^8\epsilon + 1.93E^9. \quad (33)$$

It should be noted here that in order to calculate the tangent moduli in Equations (31) and (33), a single value of strain is needed. The calculation of a single stress was explained in the above section utilizing the von Mises criterion, but no mention was made of calculating a single strain. There are a few references to a von Mises strain, but this quantity is almost never used and several different reported equations for the von Mises strain were found. Taking this into account, the most direct solution to the problem was to calculate the von Mises stress using Equation (28) and then to solve Equation (30) for the strain. In this manner, one could use the von Mises stress to calculate a single strain value. To solve Equation (30) for the strain, a simple Newton-Rhapson root-finding algorithm was developed to find the strain for any given von Mises stress. This value is then used in Equation (31) to find the tangent modulus.

It is also worth mentioning here that an additional limitation was placed upon this routine to ensure success. As noted in the composite materials literature, it is possible and probable that local stress and strain concentrations will occur throughout the RVE due to the local reinforcement provided by the nanotubes [19,67]. In reality, when the strain becomes too high, the reinforcing agent will tear from the reinforcing matrix and

reinforcement will drastically decrease. This effect can be seen visually in the experimental work of Sun et al. [46], Zhu et al. [22], and Gojny et al. [54], but is most readily observed in the work of Li and Chou [19] and shown in Figure 13.

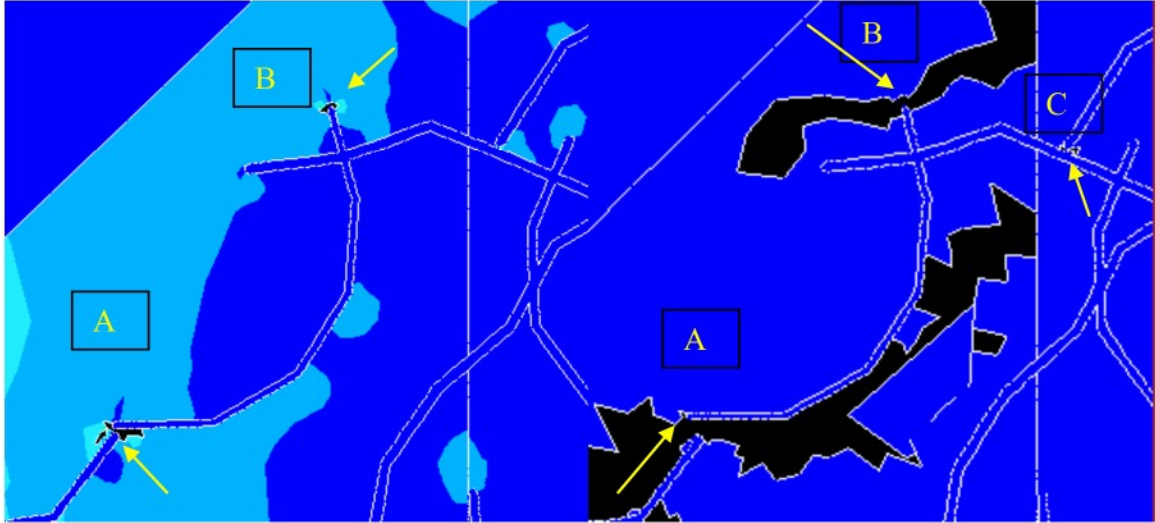


Figure 13. A close view of the stress-concentrations at nanotube tips due tensile strain is presented. Li and Chou developed this picture from their damage sensing model [19].

Since the proposed model relies upon the stress-strain curve reported by experimentalists to determine the modulus of elasticity, values of strain beyond the upper limit of the reported stress strain curve present a problem. The quadratic polynomial of Equation (31) used to calculate the tangent modulus drops drastically at high strain values, even below zero at especially high strains. Since a negative elastic modulus has no physical meaning in the context of the proposed model, this problem was avoided by setting a lower limit on the modulus of elasticity. A minimum modulus of 10 MPa, ≈ 100 times smaller than the epoxy under zero strain, was chosen to capture the “failure” of the reinforcement without allowing catastrophic failure of that element and the model as a whole.

Furthermore, the present model also accounts for the hollow structure of carbon nanotubes. As explained in the description of the Embedded Fiber Method, the

properties of the reinforcing fiber are directly combined with those of the matrix material. Implicit in this method is the assumption that the entire volume of the reinforcing fiber contributes to the reinforcement. In other words, the reinforcing fiber is assumed to have a solid structure. First discovered by Iijima in 1994, carbon nanotubes are a novel form of carbon and are in fact hollow tubes [68]. The hollow, tubular structure is clearly shown in the work of Pipes et al. [55] and is shown in Figure 14.

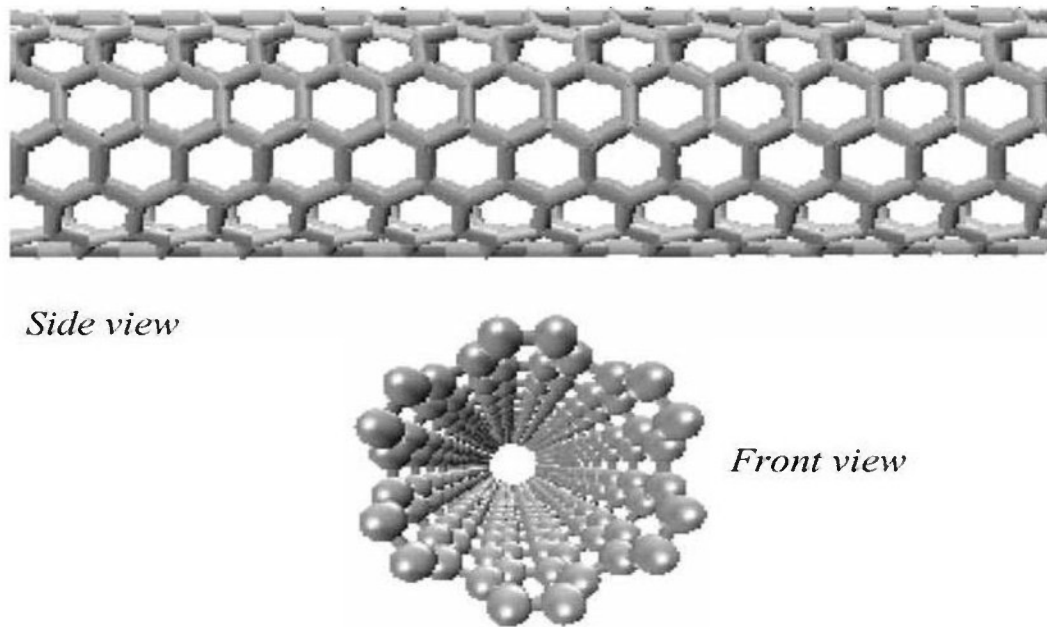


Figure 14. A diagram of a single SWCNT structure illustrates the hollow, tubular nature of CNTs [55].

The assumption, then, of solid reinforcing fibers made by the EFM is clearly not accurate on the nanoscale. This assumption would overestimate the reinforcing ability of the nanotubes, if left uncorrected, since the stiffness is calculated using the cross-sectional area of the fiber as shown in Equation (21). Several authors have reported various methods for making this correction. Seidel and Lagoudas [41] developed a micromechanics model of CNT-composites in which they used a composite cylinders approach to calculate effective properties of nanotubes when used as reinforcing fibers.

Using an initial elastic modulus of 1.1 TPa as supported by the literature cited in the introduction, they calculated an effective axial elastic modulus of 704 GPa by comparing the strain energies of solid and hollow cylinder models of the nanotubes. Odegard et al. [40] argue that a standard micromechanics approach is not accurate due to the fact that the lattice structures of the nanotube and polymer chains cannot be considered continuous at the nanoscale. They instead propose modeling the nanotube/polymer interface as an effective fiber by using an equivalent-continuum modeling method. They report an effective axial elastic modulus of 450.4 GPa. Considering this approach along with the small degradation of properties caused by functionalization [23], the fibers were assumed to have elastic moduli of 400 GPa in the current model.

In addition to the preceding data, a standard Poisson's ratio of $\nu = 0.3$ was assumed for the epoxy matrix. Nanotube upper and lower length limits of 20 μm and 800 μm , respectively, were chosen for the angle of deviation calculation in Equation (6). This assumption is based upon the reported length distributions of Wang et al. [29] and Ziegler et al. [30].

Chapter 4

Numerical Results

Having discussed the problem specific details and assumptions of the proposed approach, the elasticity and thermal results are next presented. First, the deformation behavior of the composite in tension is shown for two different boundary conditions. A comparison of the elastic results to the experiments detailed is then attempted. Finally, a discussion of the thermal results compared to other models and experiments is undertaken.

4.1 Deformation Behavior

The first result derived by the current model is a qualitative description of the deformation behavior of the composite structure as a whole for a given applied displacement in the positive y direction. By visualizing the displacements of the various elements throughout the RVE, it is possible to glean information about the distortion of the structure and the localized reinforcement effects of the carbon nanotubes. To accomplish this, the characteristics of the epoxy used by Sun et al. [46] and described in Chapter 3 were used. As also indicated above, this is a parameter that can be easily altered based on the particular composite matrix of interest. A reinforcing component of 1 wt% functionalized SWCNTs (F-SWCNTS) was randomly generated throughout the

RVE. To conduct the deformation analysis, the composite generated by the model was analyzed under two different loading conditions. In both tests, the upper boundary of the RVE was displaced $0.035\text{ }\mu\text{m}$, equivalent of a total effective strain of 3.5% on the RVE in the positive y -direction.

In the first test, the lower boundary of the RVE was held fixed in the y -direction only. This test condition was chosen because it eliminates any reactions at the fixed nodes in the x -direction. By doing so, the reactions at the fixed nodes can then be used to recover the effective stresses that will be used for the stress-strain curve. A diagram of the boundary conditions for the first test condition is shown in Figure 15.

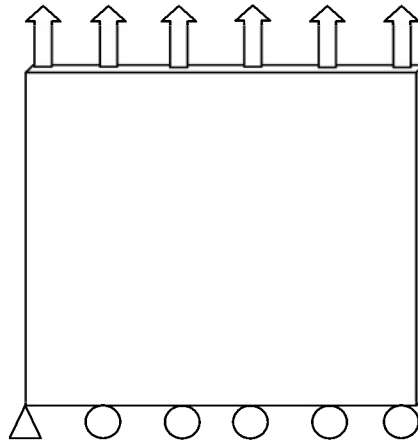


Figure 15. A diagram of the boundary conditions for the first test condition is presented. The bottom left corner is pinned and the bottom boundary is on rollers.

Using these boundary conditions, the final displacements of all the elements in the finite element mesh were examined. The number of elements in the mesh is referred to as the “mesh refinement.” The mesh refinement necessary for experimentally accurate results is discussed in the next section. A non-linear analysis was performed for one, ten, and one hundred incremental displacement steps. The different increment sizes were examined for a variety of different mesh refinements. As already mentioned in the description of

the Embedded Fiber Method, one of its primary advantages is the capacity to derive accurate results with a simple square mesh. Because the mesh is square, its refinement, as reported in this thesis, will be described using the term “divisions”. A division refers to the square root of the number of elements in the mesh. For example a mesh with one division has one element, two divisions yield four elements, four divisions yield sixteen elements, etc. This concept is illustrated in Figure 16.

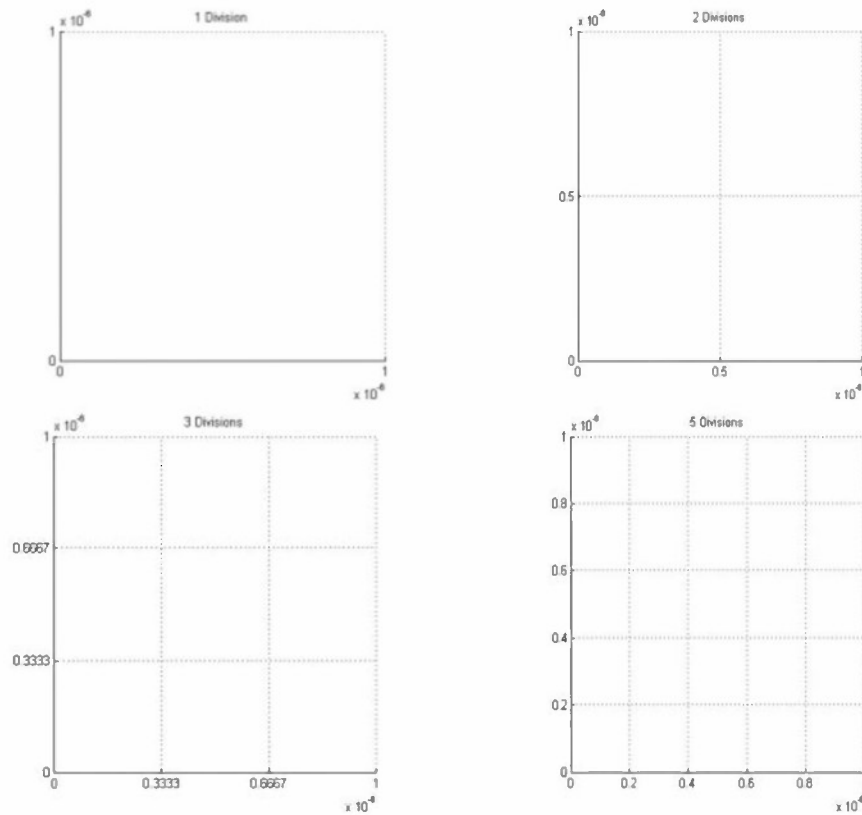


Figure 16. A visualization of the mesh refinement for one, two, three, and five divisions, respectively is shown.

The final displacements of the mesh can be visualized in two different ways. The first is to simply redraw the final mesh superimposed upon the initial mesh. This kind of visualization allows a qualitative view of the shape change of the RVE. To readily

observe this behavior, the incremental solution technique was applied with 100 equal steps to an RVE with 10 divisions and 1 wt% volume fraction of SWCNTs. The effective strain of the composite was taken to 3.5% strain. The final and initial meshes are both shown in Figure 17.

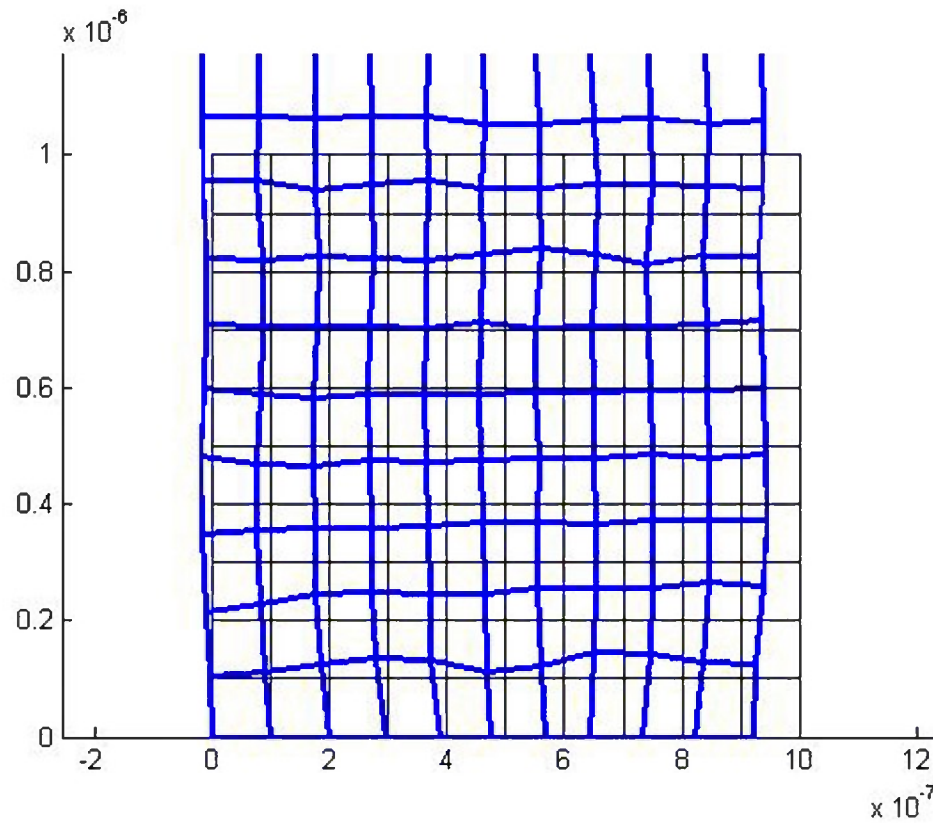


Figure 17. The mesh deformation visualization for a single RVE, with 10 divisions and 1 wt% SWCNTs, stretched to 3.5% strain is presented. The change in shape of the RVE can be easily seen and by examining the shape change of each element, the reinforcing effect of fibers can be observed. The displacements of the final mesh are multiplied by a factor of three to make visualizing easier.

The second option of visualizing the displacements of the mesh involves viewing a contour plot of displacements in the positive y direction. This technique may be more visually suggestive about nanotube reinforcement as the locations of the nanotubes can be conveniently shown along with the contour plot. A contour plot of the same RVE as depicted in Figure 17 is now shown in Figure 18.

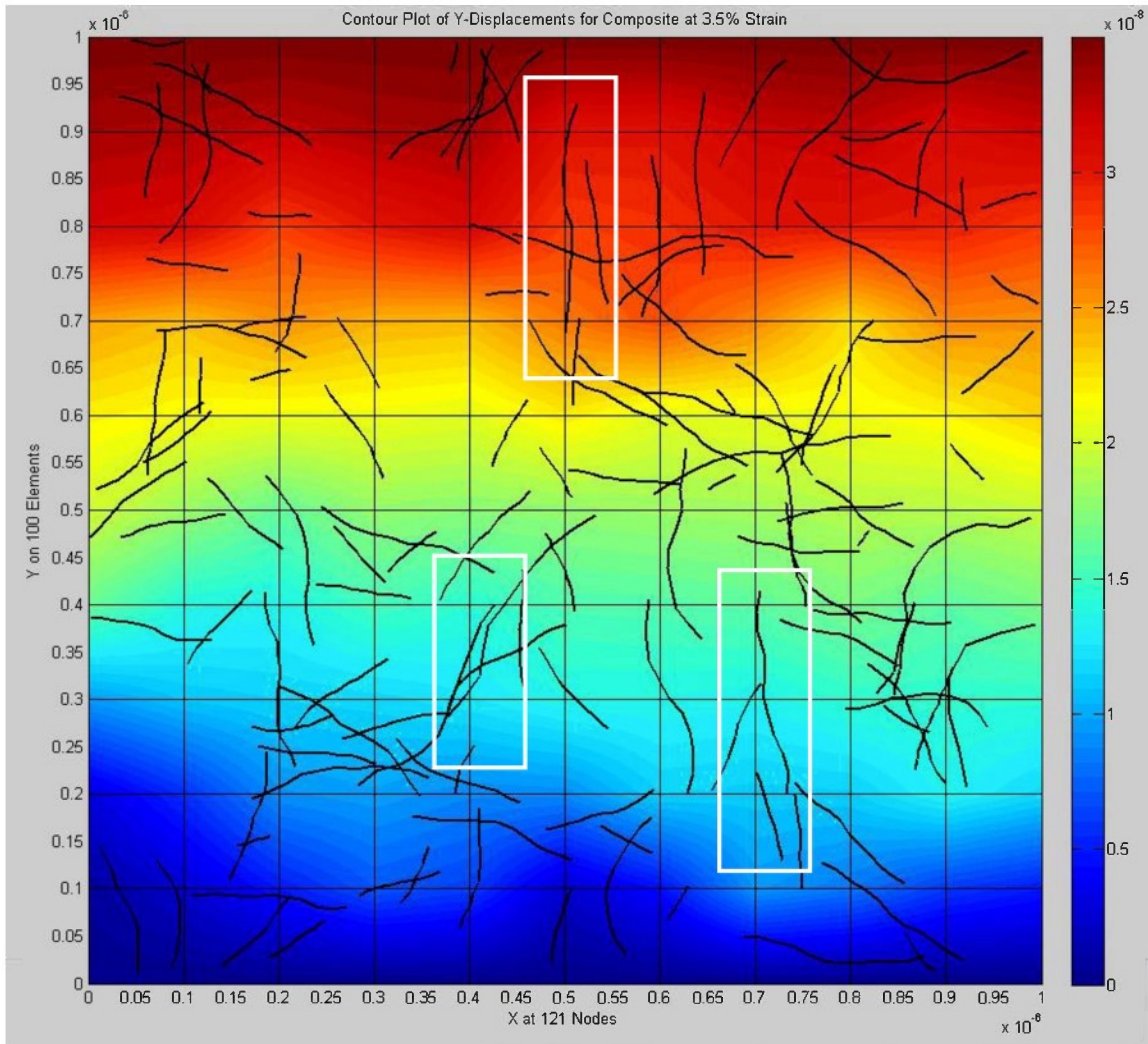


Figure 18. A contour plot of the y displacements of the element nodes is presented with the nanotube locations superimposed. The reinforcing properties of the nanotubes can be observed by noting the regions where colors stay the same. Some samples of these regions are highlighted with white boxes.

Figure 18 clearly reveals the reinforcing capabilities of the nanotubes. The most notable features to observe in the contour plot are the areas in which color remains the same or nearly the same in the y directions. These regions indicate quite small displacements and are clearly located where nanotubes are aligned in the tensile stretch direction. A few of these regions are outlined in white for easy identification.

Each of these techniques to visualize displacement is useful alone, but when they are viewed together, a comparison can be readily made, enhancing the descriptive ability of

both plots. By viewing the two plots side by side, the reinforcing effects of the nanotubes can be seen not only in the tensile direction, but also in the x direction. To this effect, the mesh deformation and displacement contours of the same RVE are shown in Figure 19. However, in this figure the plots are shown for a single step at a high strain value, approximately 2.5% strain. By examining the deformation behavior at high strains, the reinforcing capabilities are more readily observable since the surrounding matrix material is losing its capacity to elastically resist the tensile stretching.

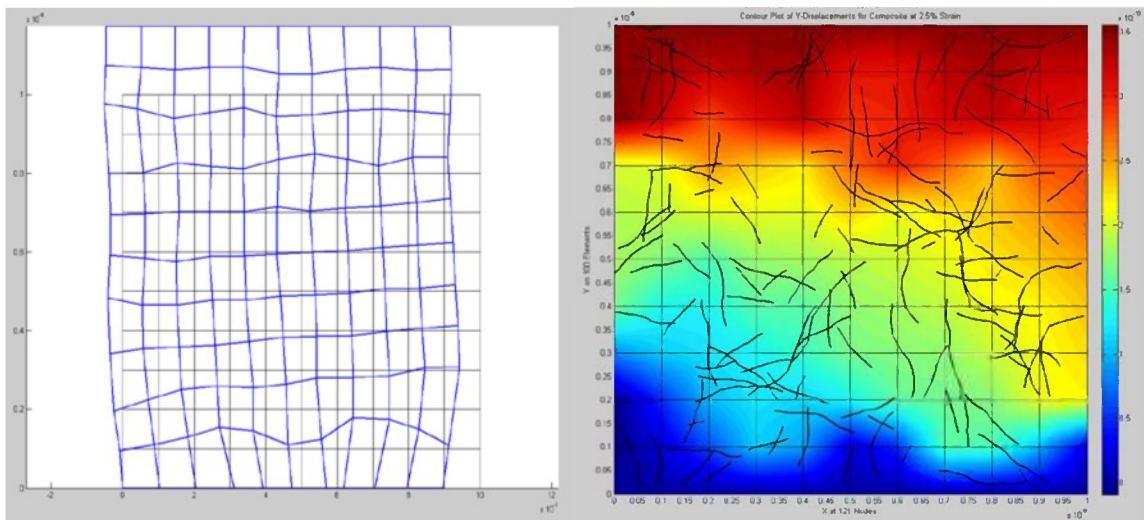


Figure 19. The mesh deformation and contour plot of y displacements for the same RVE are presented at 2.5% strain. By visualizing the displacements of a single incremental step the reinforcing capabilities of the nanotubes are very clear. The displacements of the final mesh on the left are multiplied by 300 to make visualizing easier.

Furthermore, it is insightful to compare the contour plots of the RVE before and after the onset of plastic deformation. By making this comparison, it becomes evident that at low strains, the nanotubes have a limited reinforcing role, but at high strains their role becomes very important and pronounced. The contour plots of the displacements after the first step and after the 75th step are shown in Figure 20.

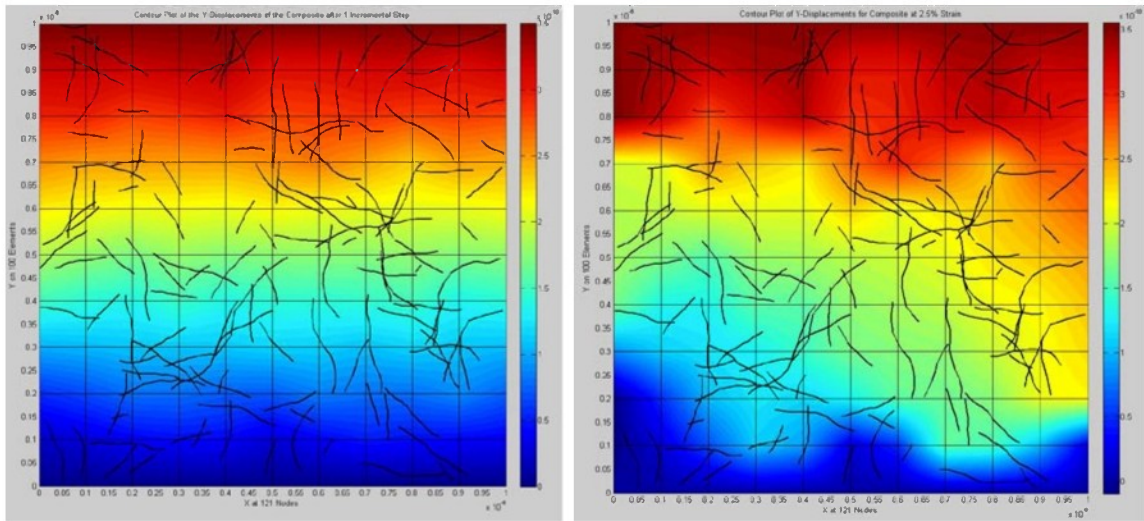


Figure 20. The contour plots of the y displacements after the first and 75th incremental steps are presented. By examining the deformation before and after the onset of plastic deformation, the role of the nanotubes in combating plastic deformation is evident.

Having presented the deformation results from the first loading condition as depicted in Figure 15, the results of the second test condition are now shown. The second condition is the traditional tensile test in which the bottom edge of the sample is fixed in both the x and the y directions and the top edge is fixed in the x direction while displaced in the y direction. These boundary conditions are shown in Figure 21.

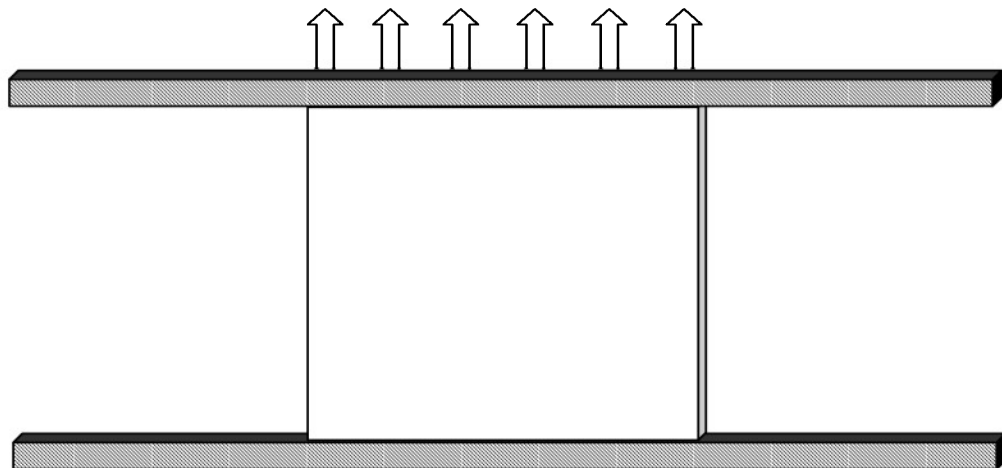


Figure 21. A diagram of the boundary conditions for the second test condition illustrates the traditional tensile test. The bottom edge is completely fixed and the top edge is fixed in the x -direction.

In the same manner as the first test condition, the change in the RVE shape can be visualized by the change in the mesh shape. The final and initial shapes are shown for an RVE with no nanotubes and an RVE with 1 wt% SWCNTs for comparison in Figure 22. In these results, 100 incremental steps were again used but 20 divisions were used this time as compared to the 10 divisions used in the results above. This difference is made only to show what 20 divisions look like when visualized.

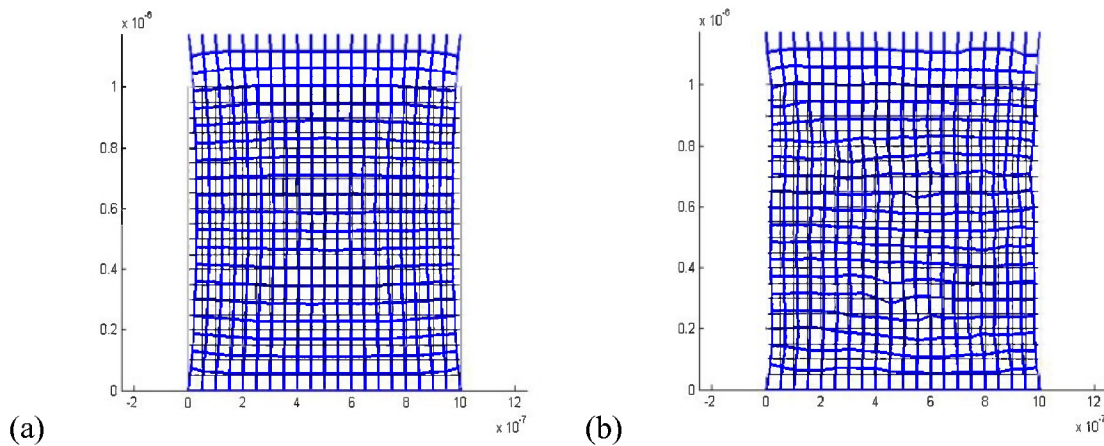


Figure 22. The mesh deformation for the second testing condition is presented. (a) Mesh deformation for an RVE without nanotubes. Symmetric deformation is observed (b) Mesh deformation for an RVE with 1 wt. % SWCNTs is shown. The final mesh displacements are multiplied by a factor of 3 to make visualizing easier.

Similarly, the contour plots with and without nanotubes are shown in Figure 23.

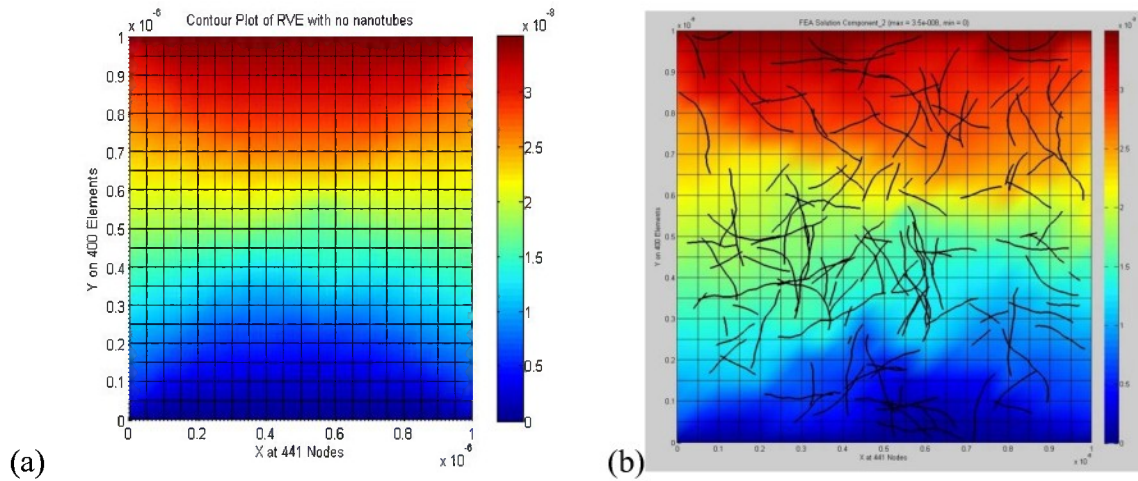


Figure 23. The displacement contours for the second test condition are presented. (a) The displacement contour of RVE without reinforcement is shown. (b) The displacement contour of an RVE with 1 wt % nanotubes is shown for comparison.

An enlargement of the contour plot in Figure 23 (b) is shown in Figure 24. Here, the areas outlined in white highlight the reinforcing capability of the nanotubes. It is also worth recognizing the path in which major changes in color occur. These paths, indicated by white lines, clearly follow regions that are void of nanotubes indicating a lack of mechanical reinforcement.

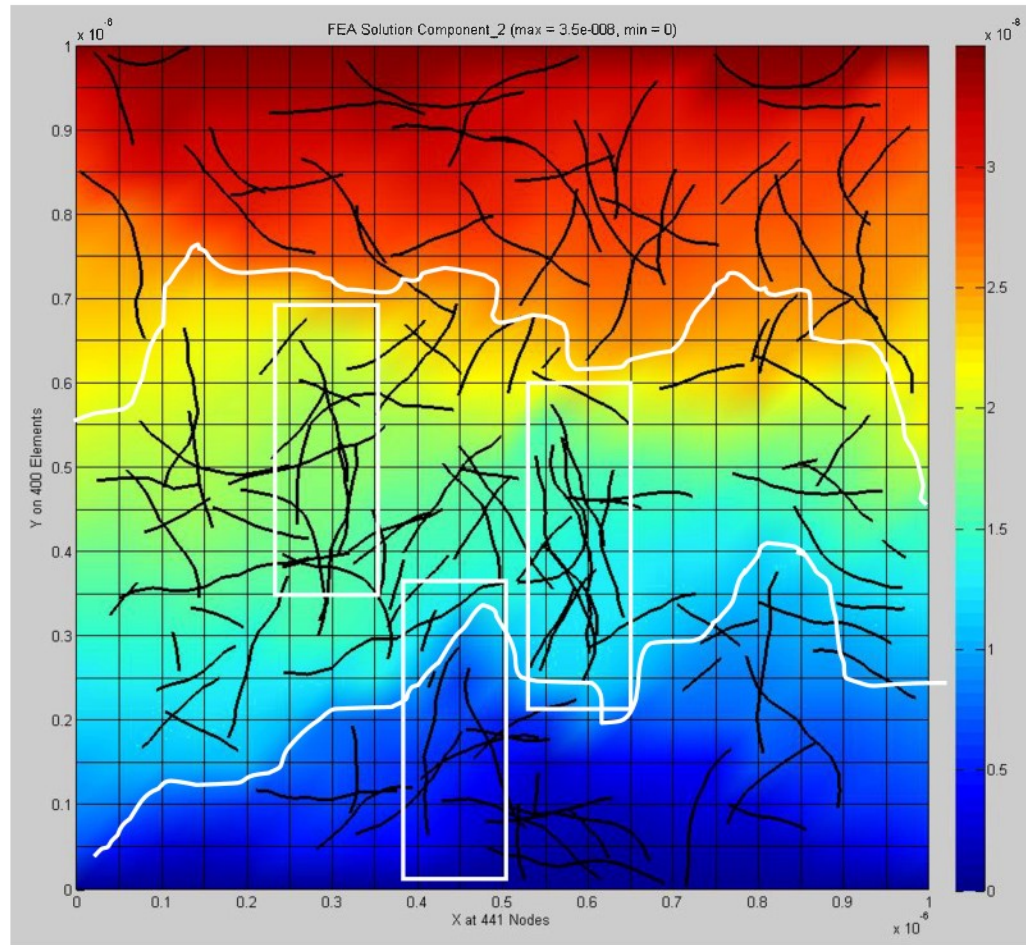


Figure 24. A displacement contour of the second test condition with special features indicated is presented. The areas boxed in white indicate sample regions of particularly strong reinforcement in the tensile direction as shown by the continuity of color. The white paths across the RVE indicate probable locations of fracture in the RVE due to lack of reinforcement.

After using both testing conditions to examine deformation behavior, the first condition was chosen to calculate the stress-strain curve for the composite. As detailed above, by allowing all the nodes to move freely in the x direction as the first condition does, there are no reaction forces in the x direction. Hence, all of the force caused by displacing the upper boundary nodes will be present in the y component of the reaction forces at the bottom nodes. This fact allows a true stress-strain relationship for the lone composite material to be developed.

4.2 Stress-Strain Results

With a qualitative view of the deformation behavior in hand, the next step was to determine the mesh refinement and number of incremental steps needed for an accurate model. To accomplish this, a mesh refinement analysis was performed and the results were compared to experimental data. The stress-strain curve used for comparison in the mesh refinement analysis is the functionalized-SWCNT curve (top, blue curve) of Sun et al. [46] shown in Figure 11.

Due to the random nature of the nanotube geometry generation, the finite element results of a single RVE would not be a statistically accurate representation of the stress-strain relationship of the general composite. To report a statistically accurate result, a Monte Carlo statistical analysis must be adopted for the data. Monte Carlo statistical analysis is a process in which meaningful information about a random event, such as the stress-strain curve of any single RVE in the current model, is gained by statistically analyzing a large number of those events. In the case of the current model, the only analysis that is needed is to take the average stress values of many different RVEs at the same strain values to create a statistically accurate stress-strain curve. To ensure that an adequate number of random RVE's were considered, the non-linear simulation is performed on 500 different RVE microstructures. The average stress values for each step are then used to generate the stress-strain curve for the composite material. Esteva [42] validated the choice of five hundred different microstructures by performing a Monte Carlo convergence analysis on his linear model. Since the proposed non-linear model is a combination of many linear solutions, this analysis validates five hundred samples as a sufficient sample size for the current model as well.

Before reporting the stress-strain curve for a material, it was first necessary to determine the number of incremental steps and the number of divisions required for the non-linear solution to converge to an accurate value. Using the same volume fraction, nanotube and epoxy densities, and Poisson's ratio as Sun et al. [46], the Monte Carlo analysis described above was performed on the results. To determine the number of incremental steps needed, the results of the incremental solution for a single division of the RVE were examined. This convergence analysis, along with the F-SWCNT curve of Sun et al. [46] for reference, is summarized in Figure 25.

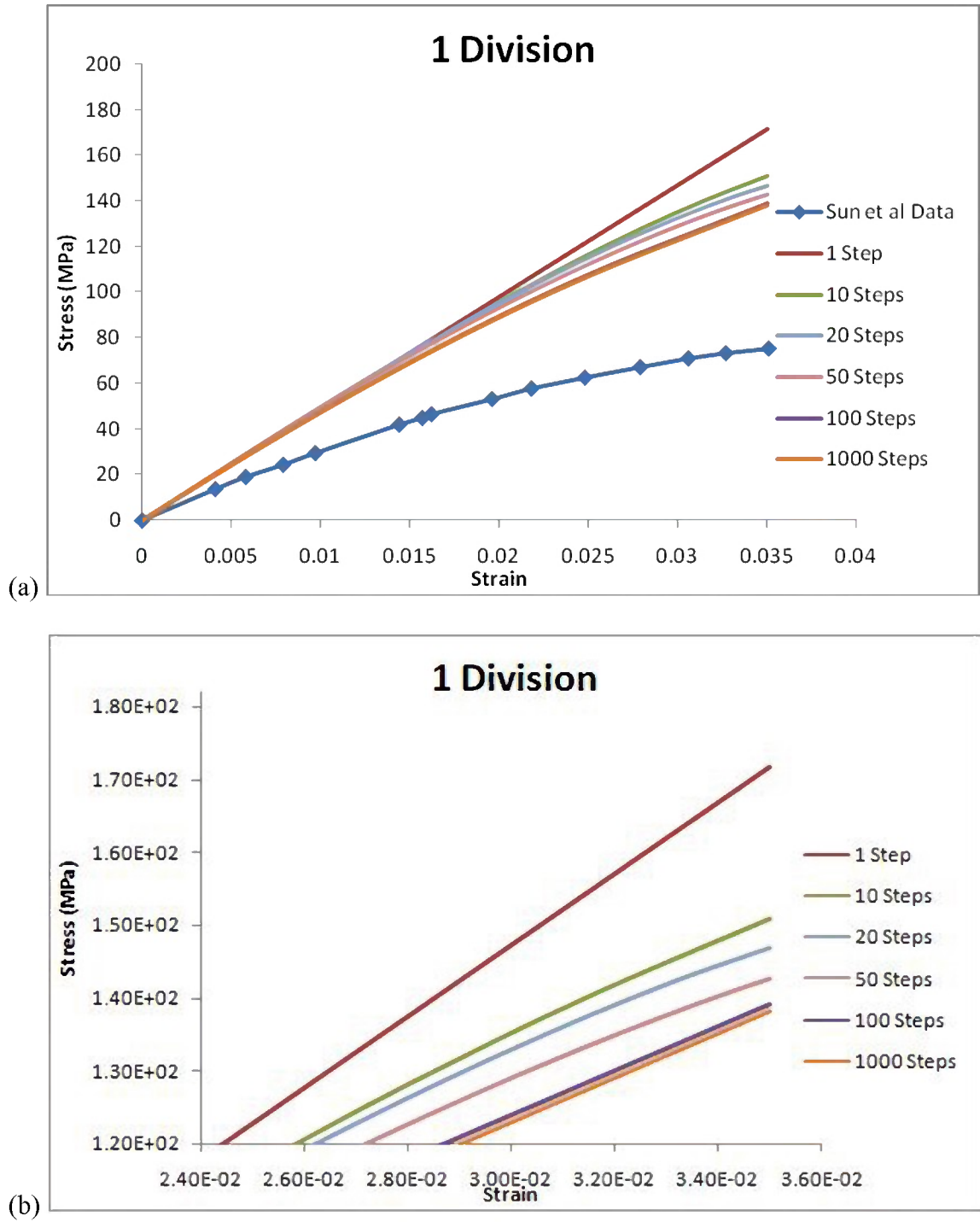


Figure 25. (a) The non-linear incremental convergence analysis for the model is shown for a single division of the RVE. (b) A closer view of the model results at high strains. A step refinement of 100 incremental steps is identified as sufficient for convergence.

By examining these results, 100 incremental steps were identified as necessary to capture the non-linearity of the epoxy. The Monte Carlo analysis was then performed on the results of 500 different RVE's for 1, 10, 20, 40, 60, and 80 divisions in order to determine the mesh refinement needed for an accurate result. This kind of mesh convergence analysis is herein termed Monte Carlo Mesh Convergence Analysis (MCMMA). The MCMMA for 100 incremental steps is presented in Figure 26 along with the F-SWCNT curve reported by Sun et al. [46].

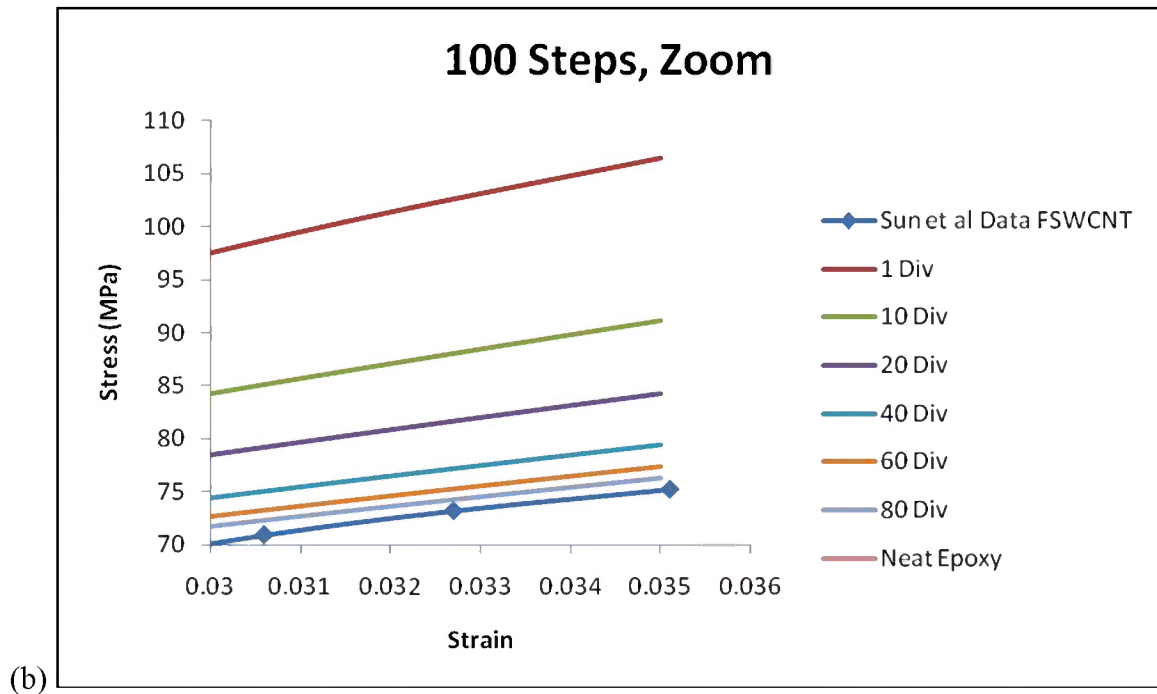
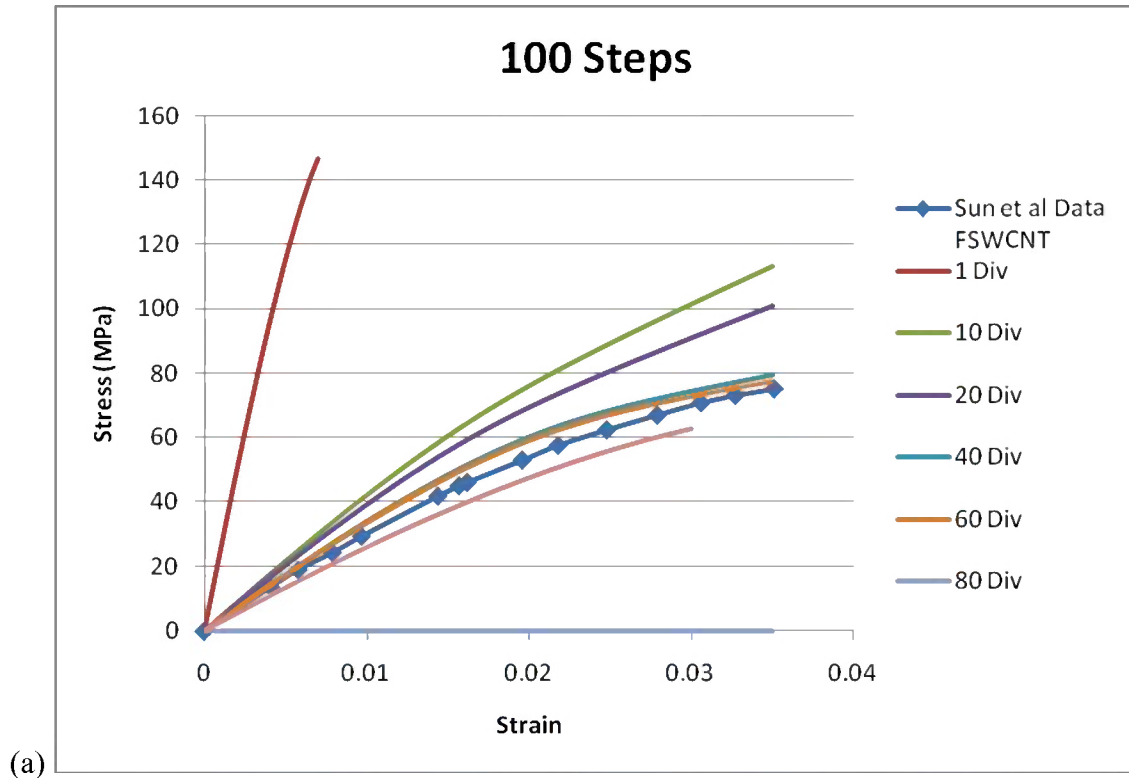


Figure 26. (a) The mesh convergence analysis for the model with one hundred incremental steps is shown for 1, 10, 20, 40, 60, and 80 divisions of the RVE. The “diamond” line identifies the experimental results of Sun et al. [45]. (b) A closer view of the model results at high strains. A mesh refinement of 60 divisions is identified as sufficient for accurate stress-strain results.

The mesh convergence analysis shown above indicates that an accurate result can be obtained with 60 divisions of the finite element mesh. Though a finer mesh will improve the accuracy, as it can be observed by the line for 80 divisions, the computational cost increases as n^2 , where n is the number of divisions. This fact creates the need to identify the minimum number of divisions necessary for accurate results, and is shown to be 60 divisions in Figure 26.

To confirm the choice of 100 incremental steps and make sure that accurate results cannot be obtained by simply increasing the number of divisions, the same MCMMA as shown in Figure 26 was conducted for both one and ten incremental steps. These results are shown in Figure 27. It is readily seen that neither one nor ten steps yield accurate results for any number of divisions.

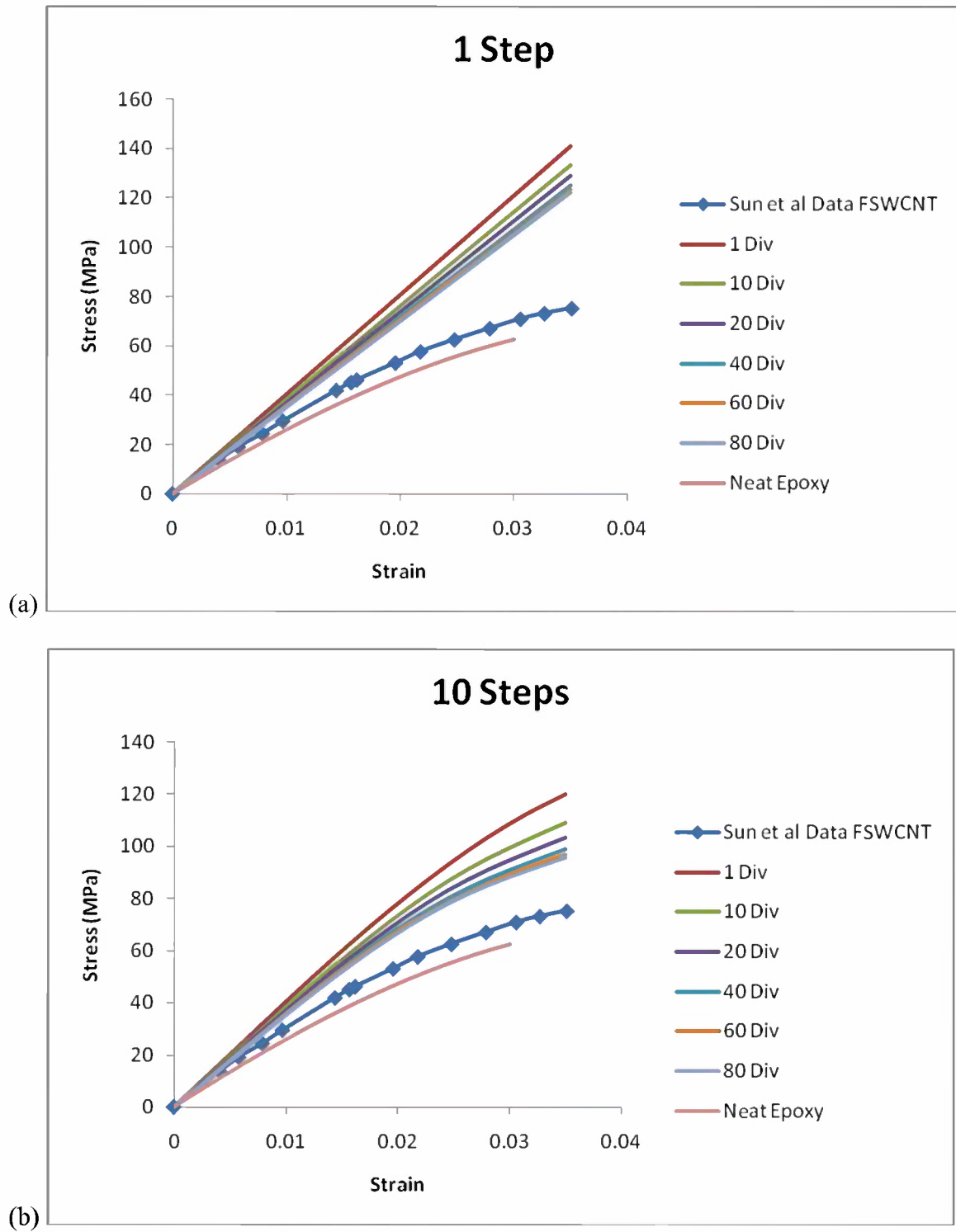


Figure 27. (a) The mesh convergence analysis for the model with one incremental step is shown for 1, 10, 20, 40, 60, and 80 divisions of the RVE. The “diamond” line identifies the experimental results of Sun et al. [45]. (b) The same analysis is shown for the model with 10 incremental steps.

With the values of 60 divisions and 100 incremental steps selected as the model parameters needed for qualitatively accurate results, the final step was to compare the results of the model to different experimental results in order to validate the accuracy and effectiveness of the model. For these data sets, statistical analysis was performed to determine the standard deviation of the Monte Carlo data. The standard deviation of a given data set is determined by the equation [69]

$$\sigma = \sqrt{\frac{1}{N} \sum_{i=1}^N (x_i - \bar{x})^2} . \quad (34)$$

In this equation, N is the number of data points, x_i is an individual data point, and \bar{x} is the mean value of that data set. After calculating the standard deviation of the stresses at the different strain levels, the stress-strain curve for 60 divisions, 100 incremental steps was compared to two different experimental data sets

The stress-strain results of the model were first compared to the experimental results of Sun et al. [46]. The tangent modulus of the epoxy matrix was updated using Equation (30) and the tensile test was simulated up to 3.5% strain. The comparison is shown in Figure 28.

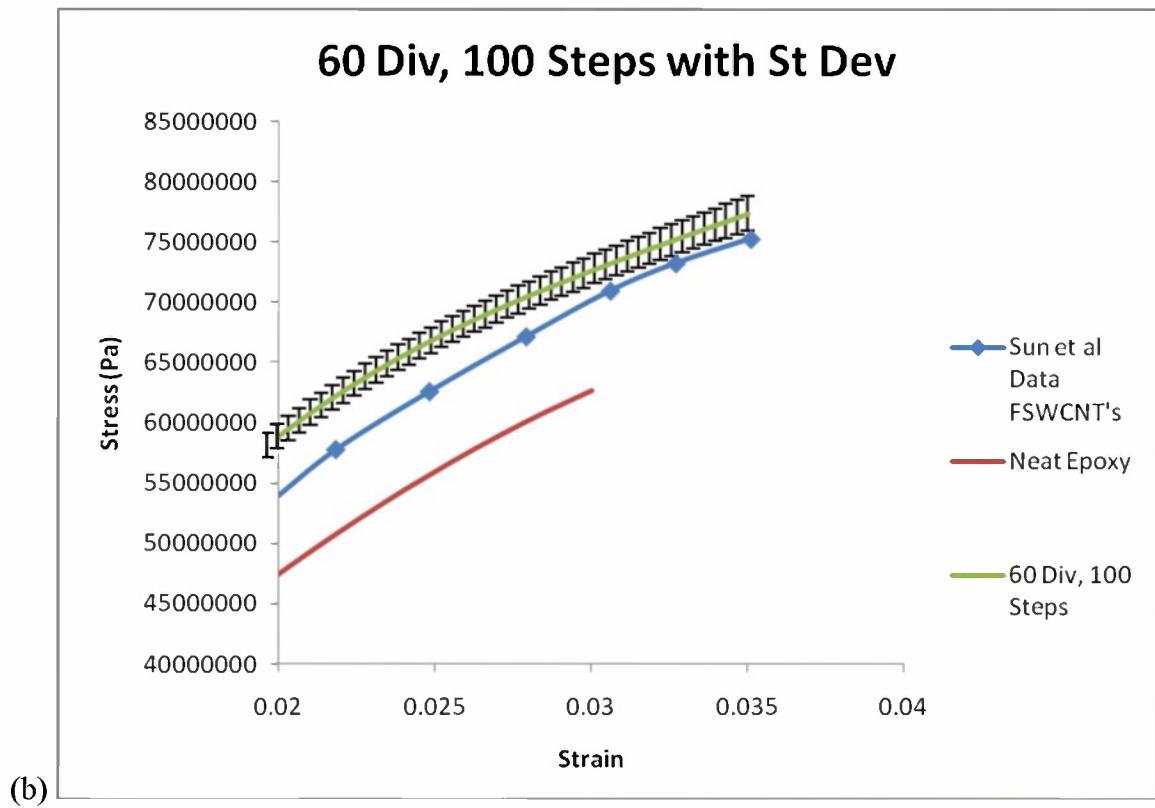
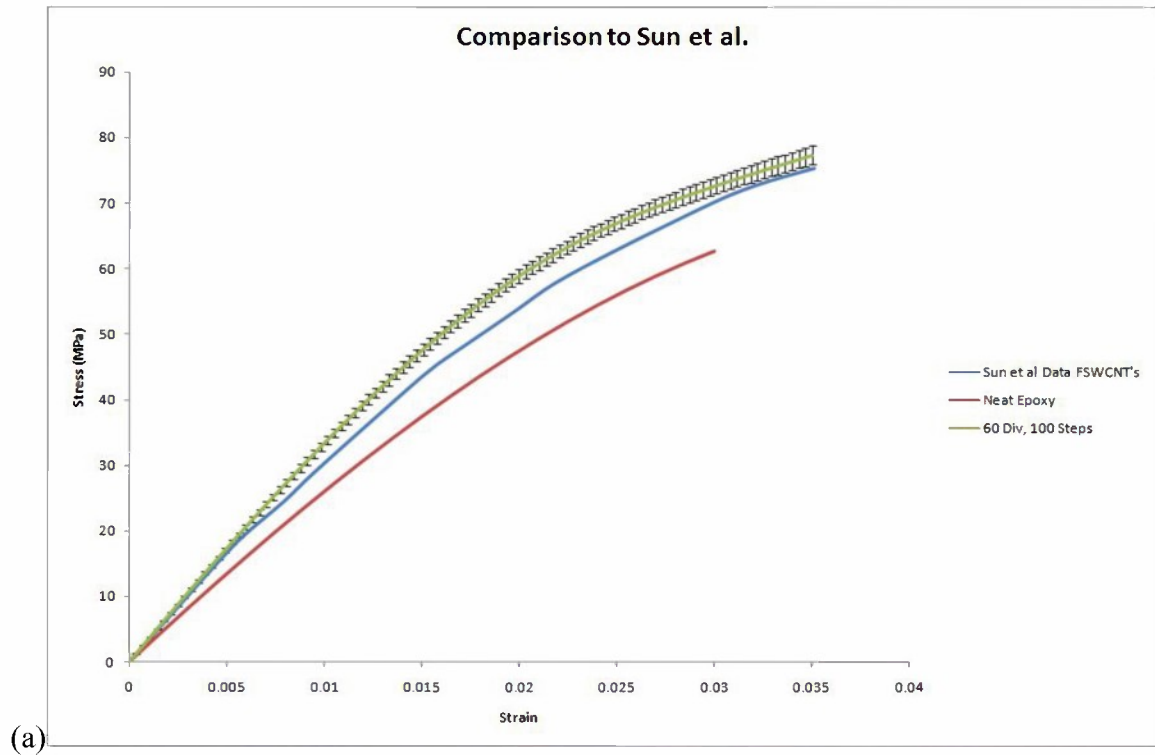


Figure 28. (a) The model results for 60 divisions, 100 steps are compared to the results of Sun et al. [45]. (b) A close view of the stress-strain curve high strain values is shown.

As can be observed Figure 28, the experimental curve is close, but does not fall within the standard deviation error bars of the model at all levels of strain. The maximum disagreement between the model and the experiment is less than 4%. Because the experimental curve is derived from a single realization of an experiment, this lack of agreement is not an indication of a poor model. By looking at the curves of the minimum and maximum RVE's shown in Figure 29, a large span of values for the stress at high strain levels can be observed. The experimental curve of Sun et al. falls within this region. This fact indicates that the model is in fact a good one and the lower curve reported by Sun et al. could be accounted for by any number of factors.

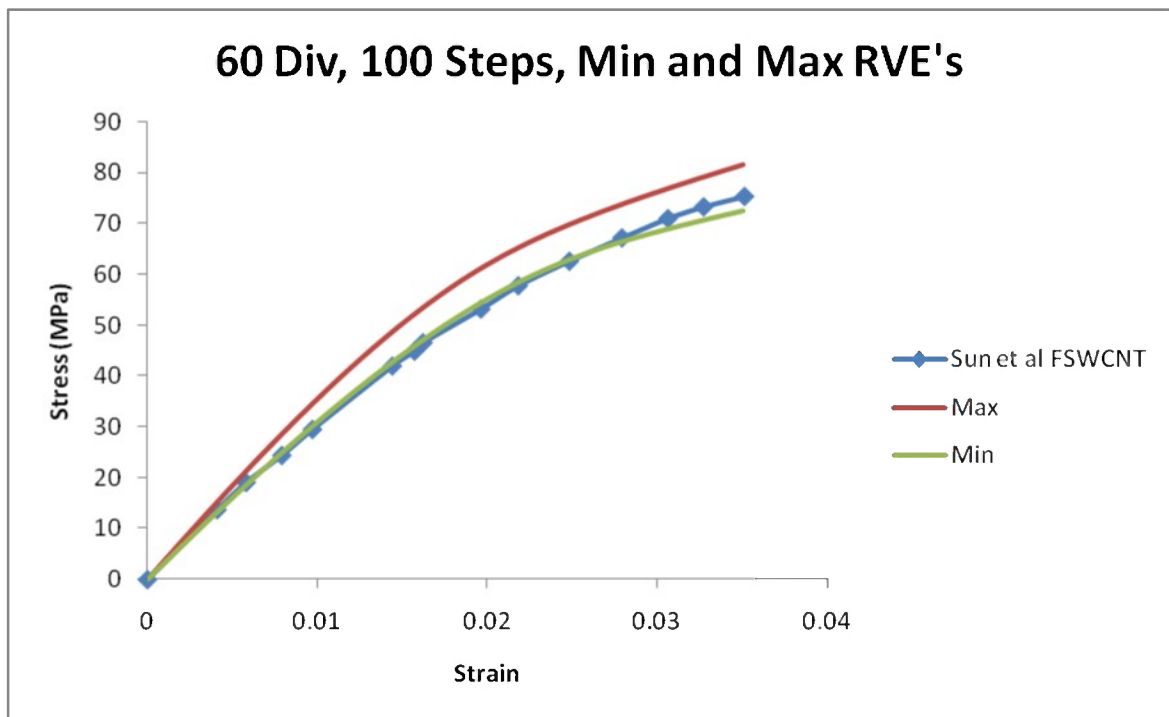


Figure 29. The maximum and minimum RVE's out of the 500 RVE's sampled in the MCMCA are compared to the experimental results of Sun et al. [45] to highlight the span of possible outcomes for random nanotube geometries.

In addition to the results of Sun et al., the model is also compared to the experimental data reported by Zhu et al. [22]. The equation used to update the elastic modulus for this

case is detailed in Equation (33). In this case, the model is used for up to 5% strain and once again, 60 divisions and 100 incremental steps were used. The comparison of the model to Zhu et al.'s data is shown in Figure 30.

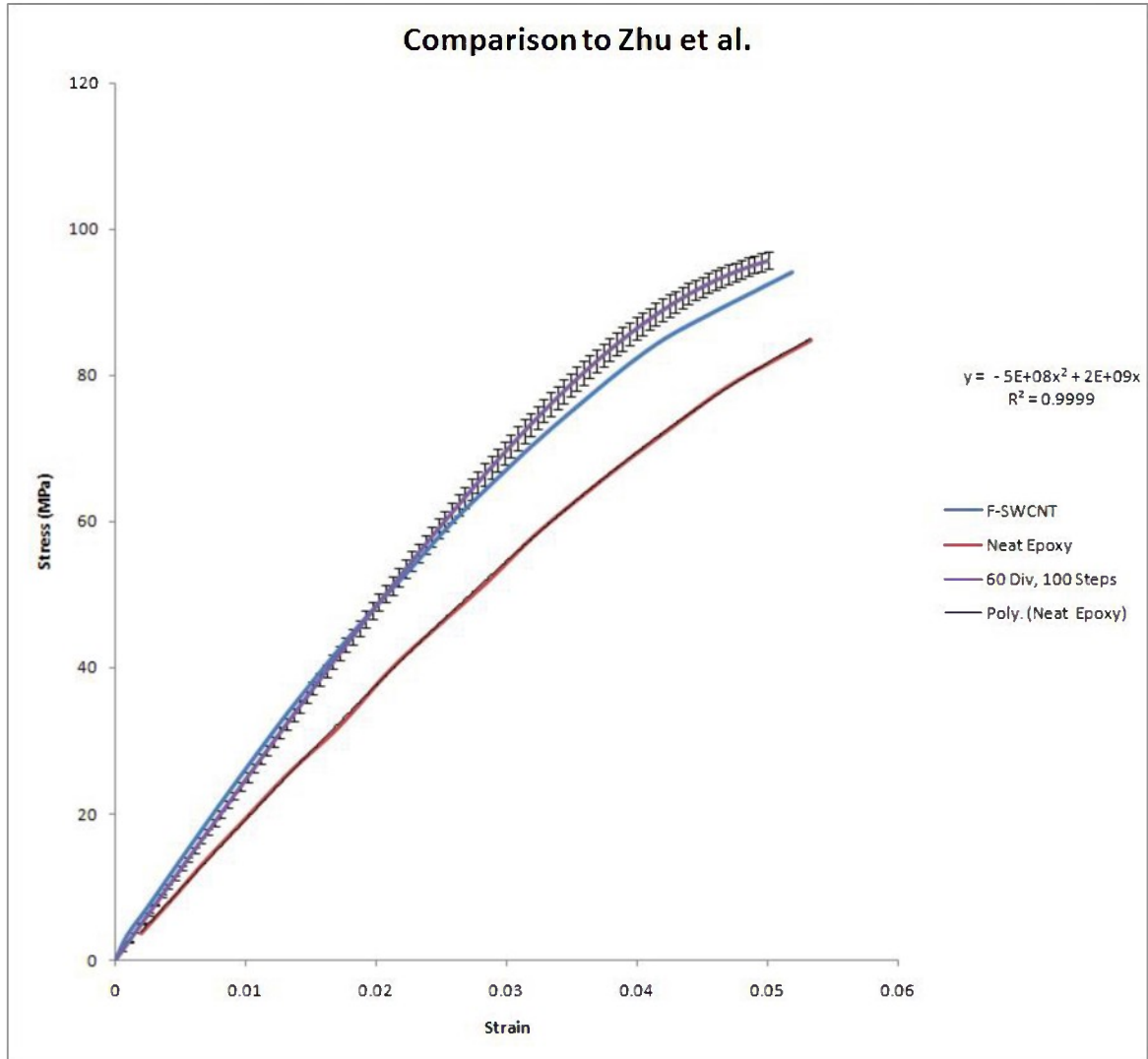


Figure 30. The model results for 60 divisions, 100 steps are compared to the results of Zhu et al. [22]. The center, blue F-SWCNT line represents the experimental data.

Akin to the first experiment, the model's calculated stress-strain curve does not fall within the standard deviation error bars at all strain values. By simply increasing the mesh refinement of the model, a closer curve could easily be generated. However, the

goal of the model proposed herein is to merely yield accurate results, and this is accomplished with 60 divisions as demonstrated above. The largest disagreement between the model and the experimental data is less than 5%. Because of the close agreement with two different experiments, the elastic model is deemed reliable. Utilizing a non-linear finite element procedure with only 60 divisions in a simple square mesh, an accurate stress-strain curve can be generated for an arbitrary nanotube-reinforced polymer composite if the polymer matrix's stress-strain curve is known.

4.3 Thermal Results

The final result of the approach presented in this thesis is calculation of the effective a non-linear thermal conductivity of the composite. Both the incremental and iterative non-linear approaches were considered in the thermal model to determine the superiority of one over the other in terms of computational time and numerical accuracy. For the thermal case, only the non-linear thermal conductivity of SWCNTs was considered because its scale is at least four orders of magnitude greater than the thermal conductivity of the polymer matrix, at any temperature. The thermal conductivity of the polymer used for the present model is assumed to be constant because of the experimental evidence of both Biercuk et al. [50] and Xu et al. [47]. First, the same method used to visualize the displacement contours in the mechanical analysis is applied to the thermal problem to visualize the temperature contour of any RVE. Mesh refinement analysis was then performed on the results of both the incremental and iterative approaches and the effective thermal conductivity for 130 divisions was compared to the values reported in the current literature. For the mesh refinement analysis, a polymer thermal conductivity

of $0.188 \frac{W}{m \cdot K}$ was used. This value is in close agreement with the values reported by Wang et al. [48] for their epoxy resin, and Cai and Song [49] for their polyurethane matrix.

Boundary Conditions and Temperature Contours

To calculate the effective thermal conductivity of the composite, the non-linear thermal properties of SWCNTs were taken from the work of Grujicic et al. [15]. A graph of the non-linear dependence of thermal conductivity on temperature is presented in Figure 9. In this model, the bottom edge of the RVE is held at $0^{\circ}C$, the top edge is held at $100^{\circ}C$, and both side edges are insulated. As usual, these values could be altered depending on the experimentalist's interests. The thermal conductivity of the composite was calculated using the heat flux at the bottom nodes of the RVE. A diagram of these boundary conditions is shown in Figure 31.

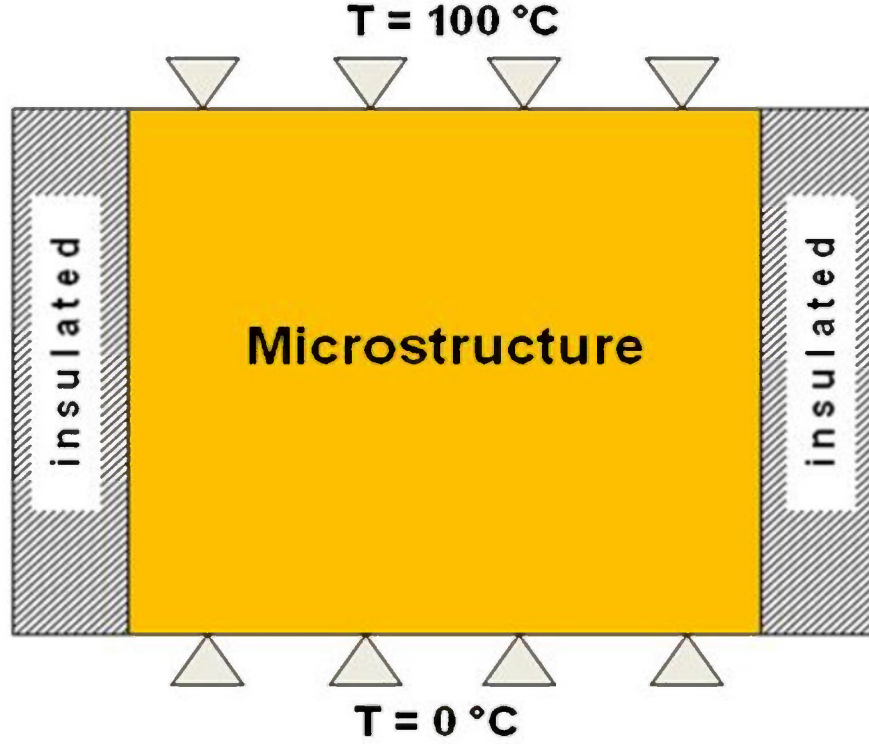


Figure 31. A diagram of the boundary conditions for the thermal analysis is shown. The top edge is held at 100° C and the bottom is held at 0°C while the sides are insulated.

To compare to the elasticity analysis, a given displacement was applied to the top of the RVE and the reaction forces at the bottom fixed nodes were recovered and used to calculate the stress in the RVE. For the thermal analysis, a temperature difference was applied between the top and bottom of the RVE and the heat fluxes at the bottom nodes were recovered. The thermal conductivity of the RVE was then calculated using the equation

$$K_{eff} = \frac{\sum q}{At\Delta T}, \quad (35)$$

where, $\sum q$ is the sum of the heat fluxes across the bottom nodes, A is the area of the RVE, t is the thickness of the RVE, and ΔT is the temperature difference between the bottom and top of the RVE.

Before calculating the thermal conductivity, the first result of the thermal analysis was a qualitative view of the thermal conductivity enhancement provided by the addition of SWCNTs to the polymer. With a similar motivation to the deformation behavior section of the mechanical analysis, visualizing a temperature contour of the RVE allows the user to gain a good understanding of how effectively nanotubes conduct heat through the composite. Using the polymer thermal conductivity of $0.188 \frac{W}{m-K}$ and the nanotube thermal conductivity curve of Grujicic et al. [15], the non-linear thermal model was run using 10 iterative steps and 40 divisions. As will be seen in the following section, the number of steps is more than enough to capture the non-linearity of the nanotubes and the number of divisions is sufficient to simply see the temperature contours accurately. The temperature contour for a random RVE with 1 wt% SWCNTs is shown in Figure 32.

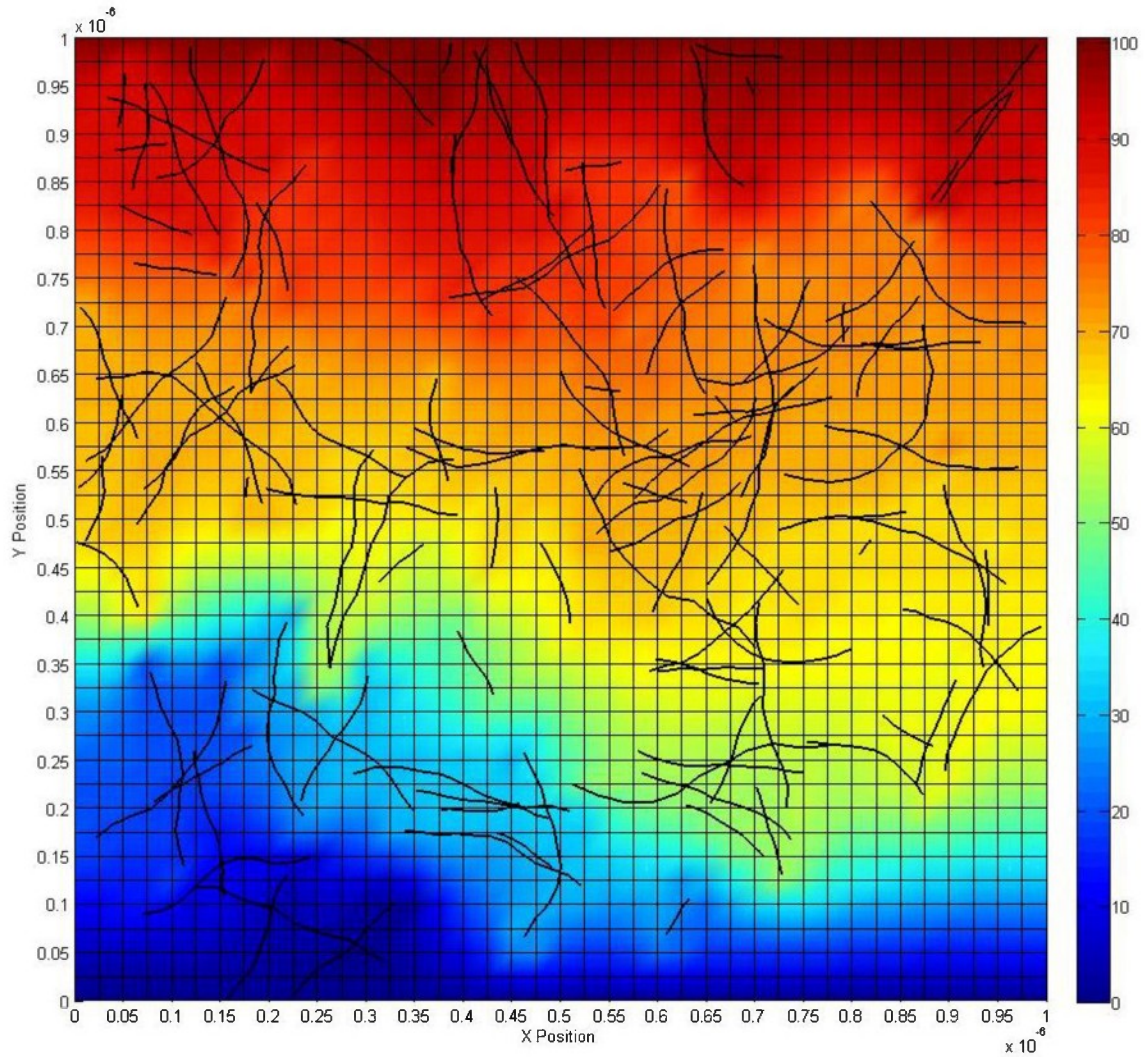


Figure 32. A contour plot of temperatures from the non-linear thermal model is presented.

Similar to the displacement contours for the elastic model, the temperature contour vividly illustrates the reinforcing effect of the nanotubes. The areas of the contour plot where color remains constant indicate regions of high thermal conductivity. These areas clearly follow the nanotubes in the RVE and indicate their role in enhancing the thermal conductivity of the composite.

Mesh Convergence Analysis

After achieving a qualitative confirmation that the model was working correctly through the temperature contours, the next step was to determine the number of steps necessary for convergence in the non-linear solution techniques. For both the iterative and incremental approaches, the thermal conductivities of the nanotubes were updated after each step using the temperatures of the nanotubes in conjunction with Equation (29). The final thermal conductivity of the composite is calculated using the heat flux at the last step in conjunction with Equation (35). Monte Carlo Mesh Convergence Analysis (MCMCA) was used to obtain statistically accurate values of thermal conductivity and to determine the finite element mesh size necessary for the thermal conductivity to converge to an accurate value. 500 RVE's were considered again for the same reasons outlined in the stress-strain results section.

The first approach taken to consider the non-linear thermal conductivity of the nanotubes was the incremental approach described in Chapter 3. Temperature increments between 0° C and 100° C were applied to the top boundary of the RVE. The MCMCA for the incremental approach is shown in Figure 33.

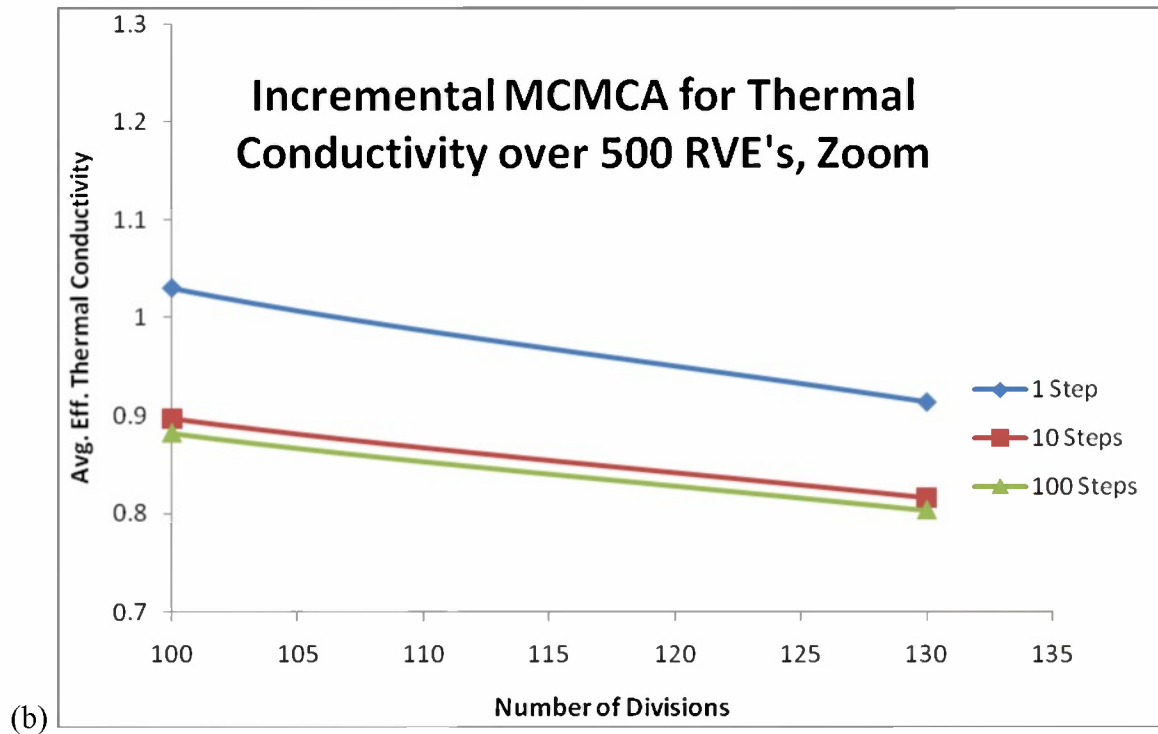
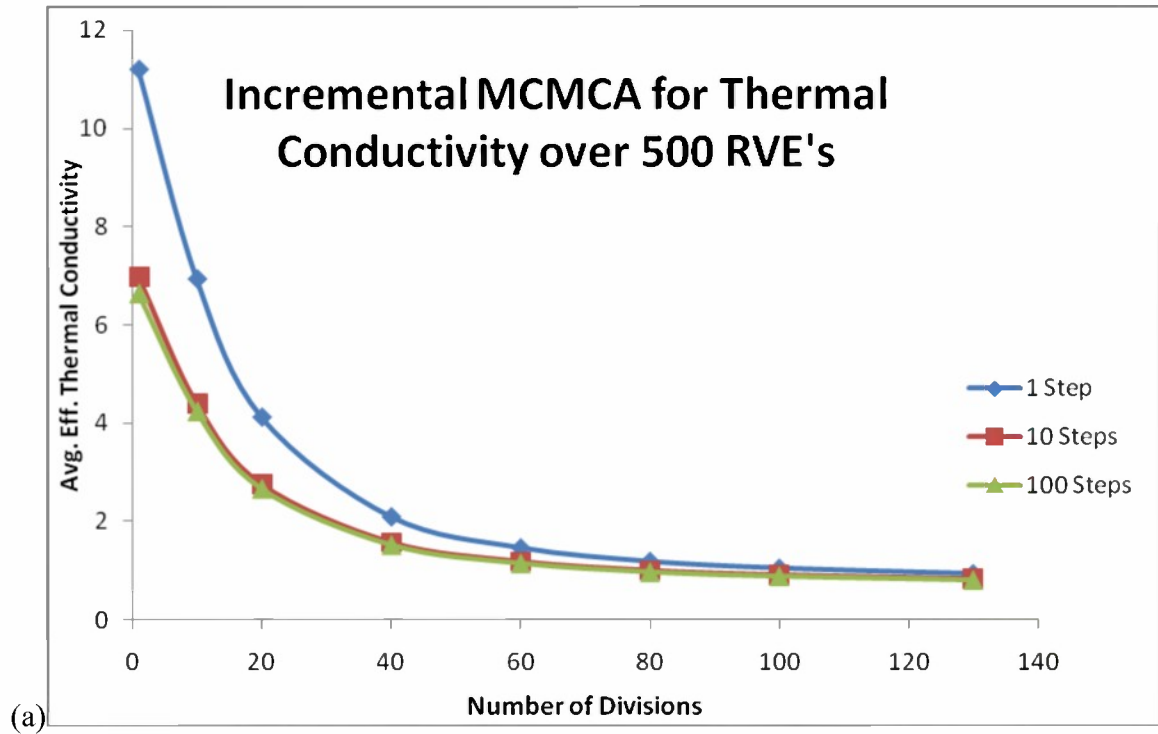


Figure 33. (a) The MCMCA for the thermal conductivity of 500 RVEs is presented for the incremental approach. A mesh refinement of 130 divisions is needed for accurate results. (b) By zooming in, it is also evident that 10 incremental steps are sufficient to capture the non-linearity of the thermal conductivity of the nanotubes.

The MCMCA shown in Figure 33 highlights the three important results of the thermal model. First, an effective thermal conductivity of $\approx 0.80 \frac{W}{m-K}$ was calculated for the composite with 1 wt. % SWCNT loading. This result shows that the model is indeed yielding accurate thermal conductivities. Second, a mesh refinement of 130 divisions was identified as necessary for the FEA to converge to a single value. Finally, it was determined that 10 incremental steps are sufficient to capture the non-linear thermal conductivity of the SWCNTs.

The second approach taken to capture the non-linearity of the SWCNTs was an iterative approach. In this approach, a single temperature gradient of 100° C was applied to the RVE. Using the resultant temperatures throughout the RVE, the thermal conductivities of the nanotubes were updated and the gradient is applied again. MCMCA was used to investigate the number of steps needed to capture the non-linearity of the nanotubes as well as the mesh refinement needed for a convergent effective thermal conductivity of the composite. This analysis is summarized in Figure 34.

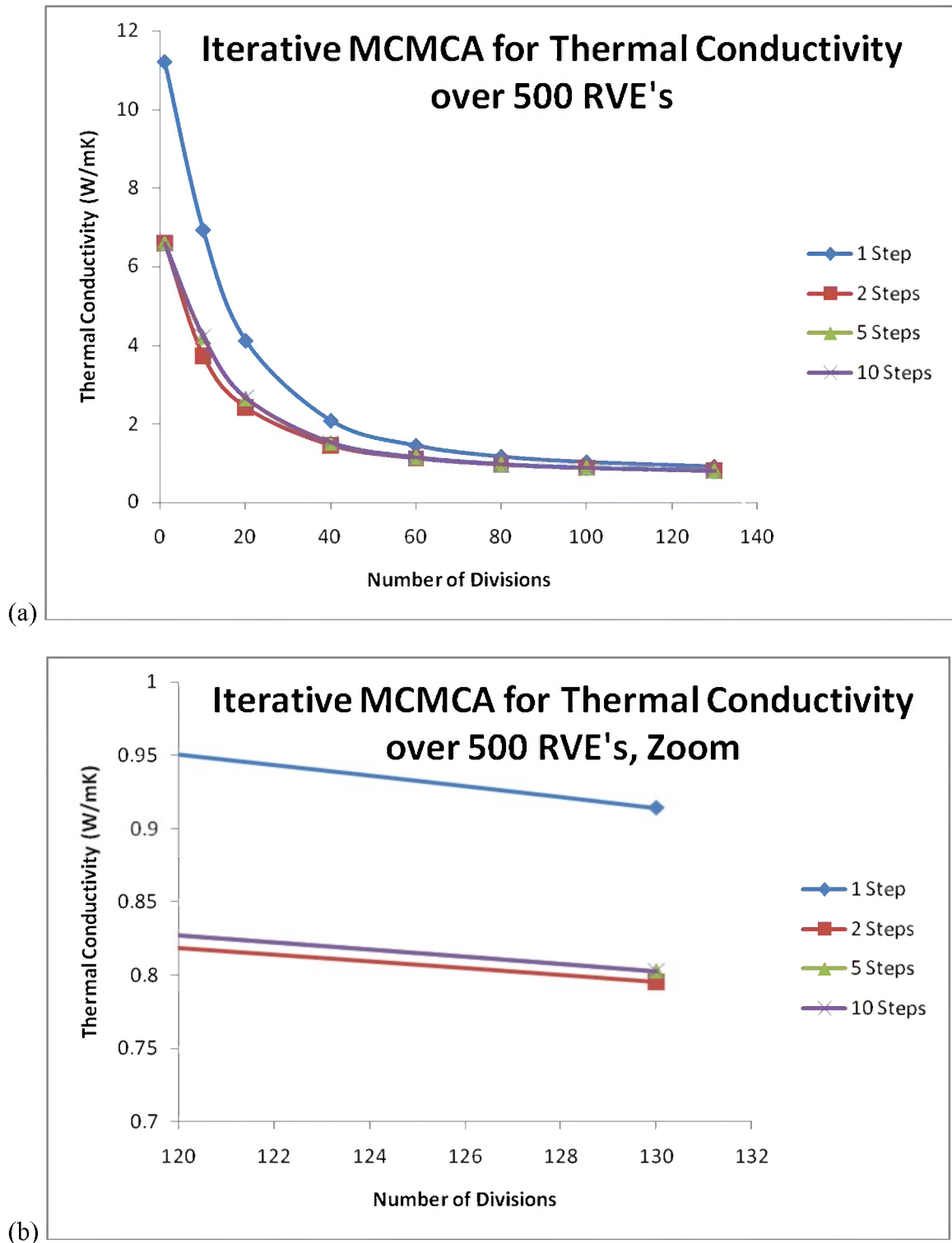


Figure 34. (a) The MCMCA for the thermal conductivity of 500 RVEs is presented for the iterative approach. A mesh refinement of 130 divisions is needed for accurate results. (b) By zooming in, it is also evident that only two iterative steps are needed to capture the non-linearity of the thermal conductivity of the nanotubes.

The MCMCA shown in Figure 34 highlights the three important results of the thermal model as well. First, an effective thermal conductivity of $\approx 0.80 \frac{W}{m-K}$ was calculated for the composite with 1 wt. % SWCNT loading. Second, a mesh refinement of 130 divisions was identified as necessary for the FEA to converge to a single value. Finally, it was determined that 2 iterative steps are sufficient to capture the non-linear thermal conductivity of the SWCNTs.

Comparing these two different approaches, it is apparent that for a mesh refinement of 130 divisions, both the incremental and iterative approaches yield almost identical results. However, it takes the incremental approach 10 steps to accomplish the same non-linear analysis that takes only two steps in the iterative approach. For this reason, the iterative approach is chosen as the preferred non-linear approach to take for the present model.

Comparison to Experiment

The final and most important step in the thermal analysis of composites using the current model is the comparison of the results to experimental data. After a thorough review of the recent literature on the subject, the data of Wang et al. [48], Moisala et al. [16], Biercuk et al. [50], Hong and Tai [51], Cai and Song [49], and Xu et al. [47] was chosen to provide a broad variety of polymers and volume fractions for comparison. Agreement with experimental results both validated the thermal model and confirmed its utility.

Before these comparisons are made, it should be first noted that it was often difficult to compare experiments to the present model exactly for several reasons. First, experimental reports do not always report the complete properties of the composite matrix that they used. The most common property left out is the density of the matrix.

This prevents a truly accurate conversion of weight fraction to volume fraction. An approximate density of $1.2 \frac{\text{g}}{\text{cm}^3}$ was used in these cases to convert weight fractions to volume fractions using Equation (7). Second, different kinds of nanotubes and procedures are often used. For example, Xu et al. [47] reported results for non-purified SWCNTs with no functionalization while Wang et al. [48] used shortened nanotubes of 50 nm or less that are well dispersed throughout the matrix. Moisala et al. [16] and Cai and Song [49] reported results for MWCNT's. Hong and Tai [51] used thin films of SWCNT networks, called Buckypapers, in reporting their results. In short, there are various experimental approaches taken to report thermal conductivity of these composites, and while the model proposed herein can account for a wide variety of physical parameters of the matrix and nanotubes themselves, it cannot account for all of the intricacies mentioned above. However, as the MCMCA results above showed, one can expect the model to still yield reliable values for the thermal conductivities of composites.

First, the model was compared to six different experiments. For each comparison, the model was executed using the same volume fraction and matrix thermal conductivity, K_m , as reported in the papers from which the data was taken. These comparisons are shown in Figure 35.

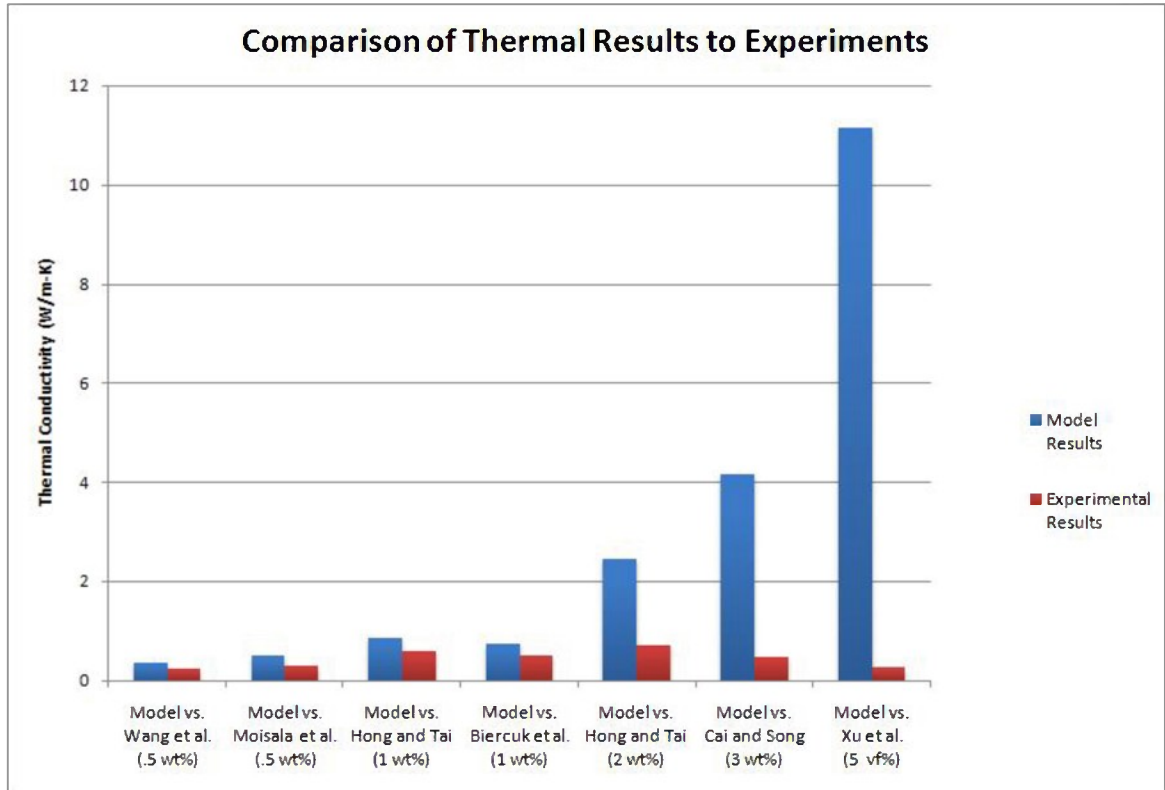


Figure 35. A comparison of the thermal conductivities calculated by the model to various experiments is shown.

As is obvious from Figure 33, the proposed model results are close to relevant experimental results for small weight fractions of 1 wt% or less. However, it is also evident that the model overestimates the thermal conductivity of the composite in every single case. Both of these observations can be explained by the imperfect assumption of perfect transfer of properties between the nanotubes and the polymer matrix inherent in the Embedded Fiber Method.

The primary reason for the inaccuracy of this assumption relates to the high thermal resistance between the nanotube-matrix and nanotube-nanotube interfaces. Huxtable et al. [70] found that the interface conductance, G , for CNT's in a polymer matrix is approximately $12 \frac{\text{MW}}{\text{m}^2\text{K}}$. For comparison, Wilson et al. [71] found an interface

conductance of $130 \frac{\text{MW}}{\text{m}^2 \text{K}}$ for platinum nanoparticles in water. This exceptionally small interface conductance will result in a significant reduction in the thermal conductivity of the composite. Closely related, Xue [72] performed a study examining the effects of interfacial resistance, or Kapitza resistance, between the nanotubes and the surrounding matrix on the effective conductivity of nanotube-reinforced composites. His results indicate that this resistance can effectively reduce the thermal conductivity of the nanotubes by several orders of magnitude. While the small thermal conductance and high thermal resistance accounts for the small overestimation of thermal conductivity at low volume fractions, it does not adequately explain the discrepancy observed at higher volume fractions.

The significant disagreement between the model and experiments for high volume fractions can be explained by the large number of junctions among carbon nanotubes that exist as the nanotube volume fraction increases. While this percolating network is ideal for electrical conductivity, a large resistance to phonon movement from one nanotube to another exists for thermal loads [47]. This resistance actually dominates the small interfacial conductance and is the primary reason why dramatic increases in thermal conductivity are seen for small volume fractions compared to very small gains with the addition of more nanotubes. For example, Wang et al. [48] report a 40% increase in thermal conductivity of their composite with the addition of only 0.5 wt% SWCNTs. In contrast, Xu et al. [47] report only a 60% increase in thermal conductivity with 19% volume fraction of SWCNTs.

With rather limited research reported in these two areas of thermal conductivity hindrance, it is impossible to incorporate these factors empirically into the model.

However, the phenomenological observation of the composite thermal conductivities reported in the literature has allowed the incorporation of these factors into the model by simply reducing the thermal conductivity of the SWCNTs by a factor of twenty. While still using the same non-linear thermal conductivity reported by Grujicic et al. [15], the result of Equation (29) is simply divided by twenty and then the rest of the model continues normally. Using this observation, the effective thermal conductivities shown in Figure 32 were recalculated and again compared to the same experiments. This comparison is shown in Figure 36 which reflects a much better agreement between the model results and the experimental data.

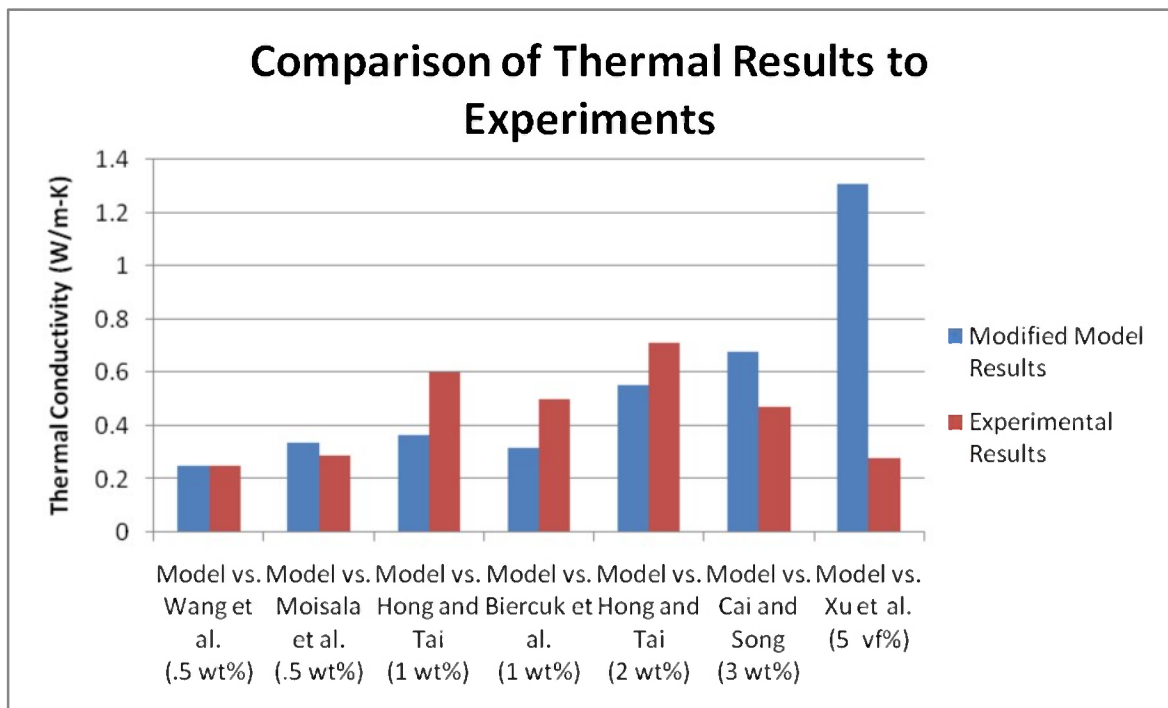


Figure 36. A comparison of the modified model's thermal conductivity results to various experiments is presented. Much better agreement with experimental results is clearly evident.

The comparison shown in Figure 34 clearly illustrates that the simple reduction of the thermal conductivity of the nanotubes by a factor of twenty creates much better agreement between the model and experiment for all volume fractions. For every

comparison, except that to Xu et al., the thermal conductivity predicted by the model is within $\approx 33\%$ of the value reported by the corresponding experiment. While this value may seem large at first, considering the poorly understood and complex mechanisms described above that inhibit efficient heat conduction, this agreement is indeed quite reasonable.

In conclusion, the thermal conductivity calculated using a two-step iterative finite element procedure using the Embedded Fiber Method produced results that provide a good approximation of the thermal properties of a SWCNT-reinforced polymer composite for volume fractions less than about three percent. Comparing model results to six different related experiments, and finding good agreement, demonstrates the versatility of the model for simulating a variety of different polymers over a large range of SWCNT volume fractions. However, the accuracy of the model could be improved with a better understanding of the mechanisms inhibiting efficient heat transfer between the polymer and the nanotubes, and between nanotube junctions.

Chapter 5

Concluding Remarks

In the past decade, a significant amount of experimental and theoretical research has been conducted to develop and characterize a large number of novel nanocomposites. The experimental research has been significantly limited by the cost, complexity, and time required in developing and testing new nanocomposites. To date, no theoretical model has been able to incorporate the non-linear mechanical and thermal properties of these new composites for a sample of significant reinforcing volume fraction.

In this thesis, a non-linear finite element model has been presented to address this need. For mechanical properties, the model was utilized to visualize the deformation behavior and to calculate the stress-strain curve of a SWCNT-reinforced polymer composite under tensile strain. For thermal properties, the model presented was used to calculate the effective thermal conductivity of the composite by incorporating the non-linear thermal conductivity of the SWCNTs.

The three major advantages of the proposed model have been exemplified in the results presented in this paper. First, the capacity to visualize the deformation of a SWCNT-reinforced polymer was demonstrated through plots of the original and deformed finite element meshes along with contour plots of the nodal displacements throughout the RVE.

By comparing these two visualizations, along with the positions of nanotubes in the RVE, significant information about the reinforcing effects of the nanotubes can be gleaned. In addition, the temperature contour plot presented in the thermal results allows the enhancement in thermal conductivity of the composite due to the nanotubes to be clearly observed.

Second, the ability to generate an accurate stress-strain curve of the composite has been demonstrated. Using a mesh refinement of 60 divisions along with a 100 incremental steps, the non-linear elastic properties of the polymer matrix were accurately modeled. After comparing the model results to the work of Sun et al. [46] and Zhu et al. [22], the model has been found to be accurate within 5% for the entire stress-strain curve.

Finally, the capacity to calculate the effective thermal conductivity of a SWCNT-reinforced polymer composite was shown. By incorporating the non-linear thermal properties of SWCNTs, the accuracy of the model is improved. Using a mesh refinement of 130 divisions along with 2 iterative steps, the thermal conductivities of seven different experimental scenarios have been calculated. After comparing the results of the model to the work of Wang et al. [48], Moisala et al. [16], Biercuk et al. [50], Hong and Tai [51], Cai and Song [49], and Xu et al. [47], it has been found that the model is accurate within 33% for any volume fraction less than 3%. While this error may seem large, it is in fact quite reasonable when considering the poorly understood mechanisms inhibiting heat transfer between CNTs and between CNTs and the polymer.

In summary, it has been found that a non-linear finite element model using the Embedded Fiber Method can accurately predict the mechanical and thermal properties of a large variety of different SWCNT-reinforced polymer composites. This model has many

potential uses in composite materials engineering. It provides experimentalists with a tool to validate their results, as well as a means to accurately explore approximate properties of systems for future experimentation. The primary feature of this model is its flexibility for use in a variety of applications. The model proposed in this thesis provides a timely and accurate calculation of deformation, stress-strain relationships, and thermal conductivities for any number of new composite materials.

Further work in the direction of this thesis may include the calculation of electrical properties for these SWCNT-reinforced polymer composites, modifications to allow the modeling of DWCNT and MWCNT-reinforced polymer composites, and the extension of the model to three spatial dimensions.

References

- [1] G.F. Paciotti, L. Myer, D. Weinreich, D. Goia, N. Pavel, R.E. McLaughlin, and L. Tamarkin, "Colloidal Gold: A Novel Nanoparticle Vector for Tumor Directed Drug Delivery.," *Drug Delivery*, vol. 11, May. 2004, pp. 169-183.
- [2] M. Telford, "Tougher nanotube fibers a hot draw: Carbon Nanotubes," *Materials Today*, vol. 8, Dec. 2005, p. 14.
- [3] C. Medina, M.J. Santos-Martinez, A. Radomski, O.I. Corrigan, and M.W. Radomski, "Nanoparticles: pharmacological and toxicological significance," *British Journal of Pharmacology*, vol. 150, Mar. 2007, pp. 552–558.
- [4] T. Natsuki, K. Tantrakarn, and M. Endo, "Effects of carbon nanotube structures on mechanical properties.," *Applied Physics A: Materials Science & Processing*, vol. 79, Jun. 2004, pp. 117-124.
- [5] M. Meo and M. Rossi, "A molecular-mechanics based finite element model for strength prediction of single wall carbon nanotubes," *Materials Science and Engineering: A*, vol. 454-455, Apr. 2007, pp. 170-177.
- [6] K. Tserpes, P. Papanikos, and S. Tsirkas, "A progressive fracture model for carbon nanotubes," *Composites Part B: Engineering*, vol. 37, 2006, pp. 662-669.
- [7] T. Belytschko, S.P. Xiao, G.C. Schatz, and R.S. Ruoff, "Atomistic simulations of nanotube fracture," *Physical Review B*, vol. 65, Jun. 2002, p. 235430.
- [8] M. Yu, O. Lourie, M.J. Dyer, K. Moloni, T.F. Kelly, and R.S. Ruoff, "Strength and Breaking Mechanism of Multiwalled Carbon Nanotubes Under Tensile Load," *Science*, vol. 287, Jan. 2000, pp. 637-640.

- [9] H. E. Troiani, M. Miki-Yoshida, G. A. Camacho-Bragado, S. M. A. L. Marques, S. A. Rubio, A. J. A. Ascencio, and M. Jose-Yacaman, "Direct Observation of the Mechanical Properties of Single-Walled Carbon Nanotubes and Their Junctions at the Atomic Level," Apr. 2003.
- [10] M.M.J. Treacy, T.W. Ebbesen, and J.M. Gibson, "Exceptionally high Young's modulus observed for individual carbon nanotubes," *Nature*, vol. 381, Jun. 1996, p. 678.
- [11] E.W. Wong, P.E. Sheehan, and C.M. Lieber, "Nanobeam Mechanics: Elasticity, Strength, and Toughness of Nanorods and Nanotubes," *Science*, vol. 277, Sep. 1997, pp. 1971-1975.
- [12] A. Desai and M. Haque, "Mechanics of the interface for carbon nanotube-polymer composites," *Thin-Walled Structures*, vol. 43, Nov. 2005, pp. 1787-1803.
- [13] S. Berber, Y. Kwon, and D. Tomanek, "Unusually High Thermal Conductivity of Carbon Nanotubes," *Physical Review Letters*, vol. 84, May. 2000, p. 4613.
- [14] F. Du, C. Guthy, T. Kashiwagi, J.E. Fischer, and K.I. Winey, "An infiltration method for preparing single-wall nanotube/epoxy composites with improved thermal conductivity," *Journal of Polymer Science Part B: Polymer Physics*, vol. 44, 2006, pp. 1513-1519.
- [15] M. Grujicic, G. Cao, and B. Gersten, "Atomic-scale computations of the lattice contribution to thermal conductivity of single-walled carbon nanotubes," *Materials Science and Engineering B*, vol. 107, Mar. 2004, pp. 204-216.

- [16] A. Moisala, Q. Li, I. Kinloch, and A. Windle, "Thermal and electrical conductivity of single- and multi-walled carbon nanotube-epoxy composites," *Composites Science and Technology*, vol. 66, Aug. 2006, pp. 1285-1288.
- [17] J. Zhu, H. Peng, F. Rodriguez-Macias, J. Margrave, V. Khabashesku, A. Imam, K. Lozano, and E. Barrera, "Reinforcing Epoxy Polymer Composites Through Covalent Integration of Functionalized Nanotubes," *Advanced Functional Materials*, vol. 14, 2004, pp. 643-648.
- [18] J.R. Wood, M.D. Frogley, E.R. Meurs, A.D. Prins, T. Peijs, D.J. Dunstan, and H.D. Wagner, "Mechanical Response of Carbon Nanotubes under Molecular and Macroscopic Pressures," *The Journal of Physical Chemistry B*, vol. 103, 1999, pp. 10388-10392.
- [19] C. Li and T. Chou, "Modeling of damage sensing in fiber composites using carbon nanotube networks," *Composites Science and Technology*, vol. In Press, Accepted Manuscript.
- [20] Q. Wang, J. Dai, W. Li, Z. Wei, and J. Jiang, "The effects of CNT alignment on electrical conductivity and mechanical properties of SWNT/epoxy nanocomposites," *Composites Science and Technology*, vol. 68, Jun. 2008, pp. 1644-1648.
- [21] T. Tiano, M. Roylance, and J. Gassner, "32nd SAMPE Conference," 2000, p. 192.
- [22] J. Zhu, J. Kim, H. Peng, J. Margrave, V. Khabashesku, and E. Barrera, "Improving the Dispersion and Integration of Single-Walled Carbon Nanotubes in Epoxy Composites through Functionalization," *Nano Letters*, vol. 3, Aug. 2003, pp. 1107-1113.

- [23] A. Garg and S.B. Sinnott, "Effect of chemical functionalization on the mechanical properties of carbon nanotubes," *Chemical Physics Letters*, vol. 295, Oct. 1998, pp. 273-278.
- [24] Kevin D. Ausman, Richard Piner, A. Oleg Lourie, Rodney S. Ruoff, and Mikhail Korobov, "Organic Solvent Dispersions of Single-Walled Carbon Nanotubes: Toward Solutions of Pristine Nanotubes," Sep. 2000.
- [25] P.C.P. Watts, W.K. Hsu, G.Z. Chen, D.J. Fray, H.W. Kroto, and D.R.M. Walton, "A low resistance boron-doped carbon nanotube-polystyrene composite ," *Journal of Materials Chemistry*, vol. 11, 2001, pp. 2482-2488.
- [26] D.A. Walters, L.M. Ericson, M.J. Casavant, J. Liu, D.T. Colbert, K.A. Smith, and R.E. Smalley, "Elastic strain of freely suspended single-wall carbon nanotube ropes," *Applied Physics Letters*, vol. 74, Jun. 1999, pp. 3803-3805.
- [27] M. Yu, B.S. Files, S. Arepalli, and R.S. Ruoff, "Tensile Loading of Ropes of Single Wall Carbon Nanotubes and their Mechanical Properties," *Physical Review Letters*, vol. 84, Jun. 2000, p. 5552.
- [28] C.D. Reddy, C. Lu, S. Rajendran, and K.M. Liew, "Free vibration analysis of fluid-conveying single-walled carbon nanotubes," *Applied Physics Letters*, vol. 90, Mar. 2007, pp. 133122-3.
- [29] S. Wang, Z. Liang, B. Wang, and C. Zhang, "Statistical characterization of single-wall carbon nanotube length distribution," *Nanotechnology*, vol. 17, 2006, pp. 634-639.

- [30] K.J. Ziegler, U. Rauwald, Z. Gu, F. Liang, W. Billups, R.H. Hauge, and R.E. Smalley, "Statistically Accurate Length Measurements of Single-Walled Carbon Nanotubes," *Journal of Nanoscience and Nanotechnology*, vol. 7, Aug. 2007, pp. 2917-2921.
- [31] D. Shi, X. Feng, Y.Y. Huang, K. Hwang, and H. Gao, "The Effect of Nanotube Waviness and Agglomeration on the Elastic Property of Carbon Nanotube-Reinforced Composites," *Journal of Engineering Materials and Technology*, vol. 126, Jul. 2004, p. 251.
- [32] J. Zhang and M. Tanaka, "Systematic study of thermal properties of CNT composites by the fast multipole hybrid boundary node method," *Engineering Analysis with Boundary Elements*, vol. 31, May. 2007, pp. 388-401.
- [33] V. Skakalova, U. Dettlaff-Weglikowska, and S. Roth, "Electrical and mechanical properties of nanocomposites of single wall carbon nanotubes with PMMA," *Synthetic Metals*, vol. 152, Sep. 2005, pp. 349-352.
- [34] K. Tserpes, P. Papanikos, G. Labeas, and S. Pantelakis, "Multi-scale modeling of tensile behavior of carbon nanotube-reinforced composites," *Theoretical and Applied Fracture Mechanics*, vol. 49, Feb. 2008, pp. 51-60.
- [35] C. Li and T. Chou, "Multiscale modeling of compressive behavior of carbon nanotube/polymer composites," *Composites Science and Technology*, vol. 66, Nov. 2006, pp. 2409-2414.
- [36] J. Xiao and J.W. Gillespie Jr., "Nanomechanics of Single-Walled Carbon Nanotubes as Composite Reinforcement*," *Polymer Engineering and Science*, vol. 46, Aug. 2006, p. 1051.

- [37] Y.S. Song and J.R. Youn, "Evaluation of effective thermal conductivity for carbon nanotube/polymer composites using control volume finite element method," *Carbon*, vol. 44, Apr. 2006, pp. 710-717.
- [38] Q. Xue, "Model for thermal conductivity of carbon nanotube-based composites," *Physica B: Condensed Matter*, vol. 368, Nov. 2005, pp. 302-307.
- [39] A. Bagchi and S. Nomura, "On the effective thermal conductivity of carbon nanotube reinforced polymer composites," *Composites Science and Technology*, vol. 66, Sep. 2006, pp. 1703-1712.
- [40] G.M. Odegard, T.S. Gates, K.E. Wise, C. Park, and E.J. Siochi, "Constitutive modeling of nanotube-reinforced polymer composites," *Composites Science and Technology*, vol. 63, Aug. 2003, pp. 1671-1687.
- [41] G.D. Seidel and D.C. Lagoudas, "Micromechanical analysis of the effective elastic properties of carbon nanotube reinforced composites," *Mechanics of Materials*, vol. 38, 2006, pp. 884-907.
- [42] M. Esteva, "Hybrid Finite Elements Nanocomposite Characterization by Stochastic Microstructuring," Doctor of Philosophy, Rice University, 2008.
- [43] A. Konrad and M. Graovac, "An application for line elements embedded in a 2D or 3D finite element mesh," *Magnetics, IEEE Transactions on*, vol. 32, 1996, pp. 647-650.
- [44] A. Ranjbaran, "Mathematical Formulation of Embedded Reinforcements in 3D Brick Elements," *Communications in Numerical Methods in Engineering*, vol. 12, Dec. 1996, pp. 897-903.

- [45] A. Ranjbaran, "Embedding of reinforcements in reinforced concrete elements implemented in DENA," *Computers & Structures*, vol. 40, 1991, pp. 925-930.
- [46] L. Sun, G. Warren, J. O'Reilly, W. Everett, S. Lee, D. Davis, D. Lagoudas, and H. Sue, "Mechanical properties of surface-functionalized SWCNT/epoxy composites," *Carbon*, vol. 46, Feb. 2008, pp. 320-328.
- [47] Y. Xu, G. Ray, and B. Abdel-Magid, "Thermal behavior of single-walled carbon nanotube polymer-matrix composites," *Composites Part A: Applied Science and Manufacturing*, vol. 37, Jan. 2006, pp. 114-121.
- [48] S. Wang, R. Liang, B. Wang, and C. Zhang, "Dispersion and thermal conductivity of carbon nanotube composites," *Carbon*, vol. 47, Jan. 2009, pp. 53-57.
- [49] D. Cai and M. Song, "Latex technology as a simple route to improve the thermal conductivity of a carbon nanotube/polymer composite," *Carbon*, vol. 46, Dec. 2008, pp. 2107-2112.
- [50] M.J. Biercuk, M.C. Llaguno, M. Radosavljevic, J.K. Hyun, A.T. Johnson, and J.E. Fischer, "Carbon nanotube composites for thermal management," *Applied Physics Letters*, vol. 80, Apr. 2002, pp. 2767-2769.
- [51] W. Hong and N. Tai, "Investigations on the thermal conductivity of composites reinforced with carbon nanotubes," *Diamond and Related Materials*, vol. 17, 2008, pp. 1577-1581.
- [52] M. Falvo, R. Taylor II, A. Helser, V. Chi, F. Brooks Jr, S. Washburn, and R. Superfine, "Nanometre-scale rolling and sliding of carbon nanotubes," *Nature*, vol. 397, Jan. 1999, p. 236.

- [53] J. Salvétat, G.A.D. Briggs, J. Bonard, R.R. Bacsa, A.J. Kulik, T. Stockli, N.A. Burnham, and L. Forro, "Elastic and Shear Moduli of Single-Walled Carbon Nanotube Ropes," *Physical Review Letters*, vol. 82, Feb. 1999, p. 944.
- [54] F.H. Gojny, M.H. Wichmann, B. Fiedler, and K. Schulte, "Influence of different carbon nanotubes on the mechanical properties of epoxy matrix composites - A comparative study," *Composites Science and Technology*, vol. 65, Dec. 2005, pp. 2300-2313.
- [55] R.B. Pipes, S.J.V. Frankland, P. Hubert, and E. Saether, "Self-consistent properties of carbon nanotubes and hexagonal arrays as composite reinforcements," *Composites Science and Technology*, vol. 63, Aug. 2003, pp. 1349-1358.
- [56] M. Hiramatsu, T. Deguchi, H. Nagao, and M. Hori, "Area-selective growth of aligned single-walled carbon nanotube films using microwave plasma-enhanced CVD," *Diamond and Related Materials*, vol. 16, 2007, pp. 1126-1130.
- [57] H. Takikawa, M. Ikeda, K. Hirahara, Y. Hibi, Y. Tao, P.A. Ruiz, T. Sakakibara, S. Itoh, and S. Iijima, "Fabrication of single-walled carbon nanotubes and nanohorns by means of a torch arc in open air," *Physica B: Condensed Matter*, vol. 323, Oct. 2002, pp. 277-279.
- [58] J. Akin, *Finite Element Analysis With Error Estimators: An Introduction to the FEM and Adaptive Error Analysis for Engineering Students*, Elsevier Butterworth-Heinemann, 2005.
- [59] C.S. Desai and J.F. Abel, *Introduction to the Finite Element Method*, Litton Educational Publishing, 1972.

- [60] O. Zienkiewicz, R. Taylor, and J. Zhu, *The Finite Element Method: Its Basis and Fundamentals*, Elsevier Butterworth-Heinemann, 2005.
- [61] T. Kawamura, Y. Kangawa, and K. Kakimoto, "Investigation of the thermal conductivity of a fullerene peapod by molecular dynamics simulation," *Journal of Crystal Growth*, vol. 310, Apr. 2008, pp. 2301-2305.
- [62] S. Shaikh, L. Li, K. Lafdi, and J. Huie, "Thermal conductivity of an aligned carbon nanotube array," *Carbon*, vol. 45, Nov. 2007, pp. 2608-2613.
- [63] X. Li, H. Gao, W.A. Scrivens, D. Fei, X. Xu, M.A. Sutton, A.P. Reynolds, and M.L. Myrick, "Nanomechanical characterization of single-walled carbon nanotube reinforced epoxy composites," *Nanotechnology*, vol. 15, 2004, pp. 1416-1423.
- [64] M. Meyers and K. Chawla, *Mechanical Behavior of Materials*, Upper Saddle River, NJ: Prentice-Hall, Inc., 1999.
- [65] H. Li, N. Zhao, C. He, C. Shi, X. Du, J. Li, and Q. Cui, "Fabrication of short and straight carbon nanotubes by chemical vapor deposition," *Materials Science and Engineering: A*, vol. 476, Mar. 2008, pp. 230-233.
- [66] Z. Jia, Z. Wang, J. Liang, B. Wei, and D. Wu, "Production of short multi-walled carbon nanotubes," *Carbon*, vol. 37, 1999, pp. 903-906.
- [67] C.M. Landis and R.M. McMeeking, "Stress concentrations in composites with interface sliding, matrix stiffness and uneven fiber spacing using shear lag theory," *International Journal of Solids and Structures*, vol. 36, Oct. 1999, pp. 4333-4361.
- [68] S. Iijima, "Helical microtubules of graphitic carbon," *Nature*, vol. 354, Nov. 1991, pp. 56-58.

- [69] J.R. Taylor, *An Introduction to Error Analysis: The Study of Uncertainties in Physical Measurements*, 55D Gate Five Road, Sausalito, CA 94965: University Science Books, 1997.
- [70] S.T. Huxtable, D.G. Cahill, S. Shenogin, L. Xue, R. Ozisik, P. Barone, M. Usrey, M.S. Strano, G. Siddons, M. Shim, and P. Keblinski, "Interfacial heat flow in carbon nanotube suspensions," *Nature Materials*, vol. 2, Nov. 2003, p. 731.
- [71] O.M. Wilson, X. Hu, D.G. Cahill, and P.V. Braun, "Colloidal metal particles as probes of nanoscale thermal transport in fluids," *Physical Review B*, vol. 66, Dec. 2002, p. 224301.
- [72] Q.Z. Xue, "Model for the effective thermal conductivity of carbon nanotube composites," *Nanotechnology*, vol. 17, 2006, pp. 1655-1660.

Appendix A

Newton Rhapson Scheme to Find the Natural Coordinates of a Nanotube

```

subroutine NatCoordFinder(exc,x,y,nc)
! find natural coordinates from
! element global coordinates (reverse mapping)
implicit none
real(8), intent(in) :: exc(8,1),x,y
real(8),intent(out) :: nc(2,1)
real(8) x1,x2,x3,x4,y1,y2,y3,y4
real(8) a1,a2,a3,a4,b1,b2,b3,b4
real(8) J(2,2),Ji(2,2),f(2,1),nci(2,1),d,jj

! extracting node coordinates
x1=exc(1,1)
y1=exc(2,1)
x2=exc(3,1)
y2=exc(4,1)
x3=exc(5,1)
y3=exc(6,1)
x4=exc(7,1)
y4=exc(8,1)

a1=0.25*(x1+x2+x3+x4)
a2=0.25*(-x1-x2+x3+x4)
a3=0.25*(-x1+x2+x3-x4)
a4=0.25*(x1-x2+x3-x4)

b1=0.25*(y1+y2+y3+y4)
b2=0.25*(-y1-y2+y3+y4)
b3=0.25*(-y1+y2+y3-y4)
b4=0.25*(y1-y2+y3-y4)

nc=0.d0 ! initial guess
d=1.d0

do while (d>0.0001d0)
! Calculating Jacobian matrix
J(1,1)=a3+a4*nc(2,1)
J(1,2)=a2+a4*nc(1,1)
J(2,1)=b3+b4*nc(2,1)
J(2,2)=b2+b4*nc(1,1)
! Calculating vector of equations

```

```

f(1,1)=a1+a2*nc(2,1)+a3*nc(1,1)+a4*nc(1,1)*nc(2,1)-x
f(2,1)=b1+b2*nc(2,1)+b3*nc(1,1)+b4*nc(1,1)*nc(2,1)-y
! Calculating inverse of Jacobian matrix
jj=J(1,1)*J(2,2)-J(1,2)*J(2,1)
Ji(1,1)=J(2,2)/jj
Ji(1,2)=-J(1,2)/jj
Ji(2,1)=-J(2,1)/jj
Ji(2,2)=J(1,1)/jj
! Newton-Rhapson Approximation
nci=nc-matmul(Ji,f)
! Calculating the norm of difference
d=sqrt((nci(1,1)-nc(1,1))**2+(nci(2,1)-nc(2,1))**2)
nc=nci
enddo
end subroutine NatCoordFinder

```